Quantum Dynamics of Strongly Correlated Ultracold Bose Gases in Optical Lattices

Vom Fachbereich Physik
der Technischen Universität Darmstadt

zur Erlangung des Grades
eines Doktors der Naturwissenschaften
(Dr. rer. nat.)

genehmigte Dissertation
von Dipl.-Phys. Markus Hild
aus Bad Soden - Salmünster

Darmstadt 2010
D17

Referent:	Prof. Dr. R. Roth
Korreferent:	Prof. Dr. J. Wambach
Tag der Einreichung:	24.11.2009
Tag der Prüfung:	16.12.2009

Abstract

Ultracold bosonic gases in optical lattices are strongly correlated quantum systems similar to solids. The strong correlation between the electrons in a solid on the one hand, and the bosonic atoms in optical lattice on the other, exhibit various quantum phenomena like insulation, conductivity, localization of electrons and atoms, respectively.

Controlled by the intensity of the lattice laser, the ultracold bosonic gas can be transferred from a regime with superfluid character for shallow lattices into a regime of strong correlations, the Mott insulator. As an additional external parameter besides the lattice depth, one can generate spatial inhomogeneities by superimposing an additional standing wave (so-called two-color superlattices), which gives rise to localization effects or the formation of a Bose-glass phase.

In the present work, numerical simulations are employed in order to investigate characteristic signatures of the quantum phases in the low-energy excitation spectrum of one-dimensional systems. We simulate temporal small amplitude modulations of the optical lattice in analogy to experiments, and evaluate the response of the system from the time-evolved initial state.

The lattice systems are described in the framework of the Bose-Hubbard model. For the evaluation of the time-evolved state, we employ several numerical methods. We analyze systems of small size (6 particles on 6 sites) using an exact time-evolution by integration of the time-dependent Schrödinger equation. The formulation of an importance truncation scheme enables us to retain only the relevant components of the model space in the strongly correlated regime and, thus, allows for the investigation of systems with 10 particles on 10 sites using exact time-evolution. Based on this method, we present results of the Mott-insulating regime as well as for the Bose-glass phase.

Furthermore, we employ particle-hole methods, which allow for the treatment of systems with experimental lattice sizes and particle numbers. Starting from the equation of motion method we adapt the Tamm-Dancoff approximation as well as the random-phase approximation for the occupation number representation of the Bose-Hubbard model. We present results of simulations of up to 50 particles on 50 sites and discuss the impact of the lattice depth on the low-energy excitations (U-resonance). Moreover, the impact of a two-color superlattice and the variation of its amplitude is investigated.

Zusammenfassung

Ultrakalte bosonische Gase in optischen Gittern bilden stark korrelierte Quantensysteme, die vergleichbar mit Festkörpersystemen sind. Die starke Korrelation zwischen Elektronen im Festkörper auf der einen Seite, und den bosonischen Atomen im Gittersystem auf der anderen führen zu zahlreichen Quantenphänomenen wie Isolatoreffekten, Leitfähigkeit und Lokalisierung von Elektronen bzw. Atomen.

In Abhängigkeit von der Intensität der Gitterlaser läßt sich ein ultrakaltes Gas von Bosonen von einem Regime mit ausgeprägtem superfluiden Charakter für flache Gitter in ein stark korreliertes Regime, den Mott-Isolator, überführen. Als weiteren Freiheitsgrad neben der Gittertiefe lassen sich mittels Überlagerung mit einer weiteren optischen Stehwelle räumlich Inhomogenitäten erzeugen (sogenannte Zwei-Farb Supergitter), welche, bei entsprechender Stärke, Lokalisierung oder die Ausbildung einer Bose-Glas Phase hervorrufen.

Im Rahmen dieser Arbeit werden mittels numerischer Simulationen charakteristische Signaturen der Quantenphasen im niederenergetischen Anregungsspektrum von eindimensionalen Gittersystemen untersucht. Wir simulieren hierzu eine schwache zeitliche Amplitudenmodulation des optischen Gitters, welche ebenfalls in Experimenten Anwendung findet, und erfassen die Antwort des Systems durch Auswertung des zeitentwickelten Anfangszustandes.

Die Beschreibung der Gittersysteme findet im Rahmen des Bose-Hubbard Modells statt. Zur Ermittlung des zeitlich entwickelten Zustandes werden verschiedene Methoden angewandt. Wir analysieren Systeme mittlerer Größe (6 Teilchen auf 6 Gitterplätzen) im Rahmen einer exakten Zeitentwicklung durch Integration der zeitabhängigen Schrödingergleichung. Die Einführung einer Importance Truncation erlaubt uns den Modellraum im stark korrelierten Regime derart einzuschränken, daß Systeme mit bis zu 10 Teilchen und Gitterplätzen mittels exakter Zeitentwicklung untersucht werden können. Auf Basis dieser Methode werden Resultate für die Mott-Isolator- sowie die Bose-Glas Phase vorgestellt.

Darüber hinaus wenden wir Teilchen-Loch Methoden an, welche uns ermöglichen, Systeme mit experimentellen Gittergrößen und Teilchenzahlen zu simulieren. Ausgehend von der Bewegungsgleichungsmethode adaptieren wir sowohl die Tamm-Dancoff-Approximation als auch die Random-Phase-Approximation für die Besetzungsdarstellung des Bose- Hubbard Modells. Wir präsentieren die Ergebnisse von Simulationen mit bis zu 50 Teilchen auf 50 Gitterplätzen. Diskutiert werden in diesem Rahmen der Einfluss der Wechselwirkungsstärke auf niedrig liegende Anregungen (U-Resonanz) der Systeme. Des Weiteren wird der Einfluss des Zwei-Farb-Supergitters und die Variation dessen Modulations-

amplitude untersucht.

Contents

Introduction

A short history of Bose-Einstein condensation

The creation of ensembles of atoms at temperatures below a few microkelvin opened the door to exciting experimental and theoretical studies of fundamental quantum phenomena. A prominent example is the condensation of bosonic particles into the energetically lowest quantum state. This phenomenon, the Bose-Einstein condensation, was already predicted in 1924. The derivation of the statistical behavior of photons by Bose [1] and the subsequent generalization to an ideal gas of massive particles by Einstein [2] predicted the condensation of the particles into the same single-particle state. Particles of integer spin — the bosons — obey the Bose-Einstein statistics and are subject to Bose-Einstein condensation at low temperatures. In contrast, fermionic particles obey the Fermi-Dirac statistics and are not allowed to occupy the same quantum state due the Pauli exclusion principle.

A milestone regarding the realization of this new state of matter was achieved by Heike Kammerlingh-Onnes in 1911, thirteen years before the theory of BECs was established. One of his achievements was to advance the refrigeration techniques which led to the discovery of superconductivity: In 1911, he observed an abruptly vanishing electrical resistance of mercury at $T = 4.2\,\mathrm{K}$ [3]. It took about forty years, until the phenomenological Ginzburg-Landau theory [4] explained superconductivity as a macroscopic quantum effect. A few years later, the BCS theory was found by Bardeen, Cooper, and Schrieffer in 1957 [5], which provides a microscopic description of superconductivity. This theory states, that two electrons of opposite spin alignment form a *Cooper pair* based on a weak attractive interaction mediated by vibrational modes of the crystal lattice (phonons). Due to their bosonic character, Cooper pairs are subject to Bose-Einstein condensation and show collective behavior which results in the charge transport without resistance.

Another closely related low-temperature phenomenon is superfluidity, i.e., the ability of a liquid to flow without friction. Superfluidity of liquid ^{4}He below 2.17 K has been discovered by Kapitsa, Allen, and Misener in 1938 [6,7] and was assumed to be a manifestation of Bose-Einstein condensation. However, superfluid helium is a strongly interacting liquid rather than a dilute gas as in Einsteins theory. Hence, the connection to Bose-Einstein condensation could not be proven easily. It took until 1960, when Henshaw and Woods found experimental evidence for a condensate in superfluid helium by neutron scattering [8]. However, due to the strong interatomic interaction, only a small fraction of the superfluid helium is also a Bose-Einstein condensate.

In order to create a *pure* Bose-Einstein condensate, it was necessary to focus on dilute gases. A lot of experimental efforts have been spend to condense hydrogen [9] around 1980, but the condensation was inhibited by the recombination of the atoms to molecules. However, these endeavors led to the development of magnetic traps [10] which allow to confine neutral atoms by their magnetic moment.

A crucial element in order to reach the ultracold temperature regime required for condensation of dilute gases is laser cooling. Laser cooling includes a wide range of methods to cool atoms based on the interaction with photons, and was significantly advanced by Chu, Cohen-Tannoudji, and Phillips, who received the Nobel prize in 1997. A prominent example is Doppler cooling, where the cooling effect is achieved by the absorption of photons from a distinct direction and the successive isotropic spontaneous emission, which results in a decrease of the velocity in direction of the laser beam.

However, using laser cooling alone one cannot reach the nanokelvin regime required for condensation. The cooling effect is limited by the so-called recoil limit to typically $\sim 1\,\mu$K, where the recoil received by spontaneous emission of a photon balances the cooling effect. In order to overcome this limit, evaporative cooling is applied to approach the condensation regime. Evaporation means to allow high velocity particles to escape from the ensemble, which results in a decrease of the temperature after re-thermalization.

Eventually, these techniques enabled the group of Wieman and Cornell to reach the critical temperature and density to Bose-Einstein condense a vapor of ^{87}Rb atoms [11] in 1995. Figure 1 illustrates the velocity distributions obtained by the time-of-flight method[1] for different temperatures in the condensation regime. The atoms are confined in a 3D trapping potential of oblate geometry, i.e., the cloud is more tightly confined in the axial than in the radial direction. This asymmetry allows to identify the condensate and non-condensate fraction of the cloud by the geometry of the velocity distribution after the time of flight: the thermal cloud (non-condensate fraction) shows an isotropic expansion regardless of the geometry of the trap, whereas the condensate reflects the geometry of the trap. A few months later, the condensation of ^{23}Na atoms has been achieved in the group of Wolfgang Ketterle [13]. Their condensate consisted of 5×10^5 atoms, in contrast to the 2000 atoms in the Rubidium condensate of Wieman and Cornell. The experimental realization of BECs offers unique possibilities to study quantum phenomena in a macroscopic system, such as the interference between two expanding condensates [14], which reflects the wave-like behavior of matter. Another example is the atom laser [15]. Here, instead of coupling out coherent light from a cavity, coherent matter-waves are coupled out from the trap.

---

[1] The velocity distribution of the atom cloud is proportional to the particle density after a ballistic expansion (time-of-flight). The image of the density distribution is obtained by exposure of the cloud to resonant light, resulting in a shadow image due to absorption.

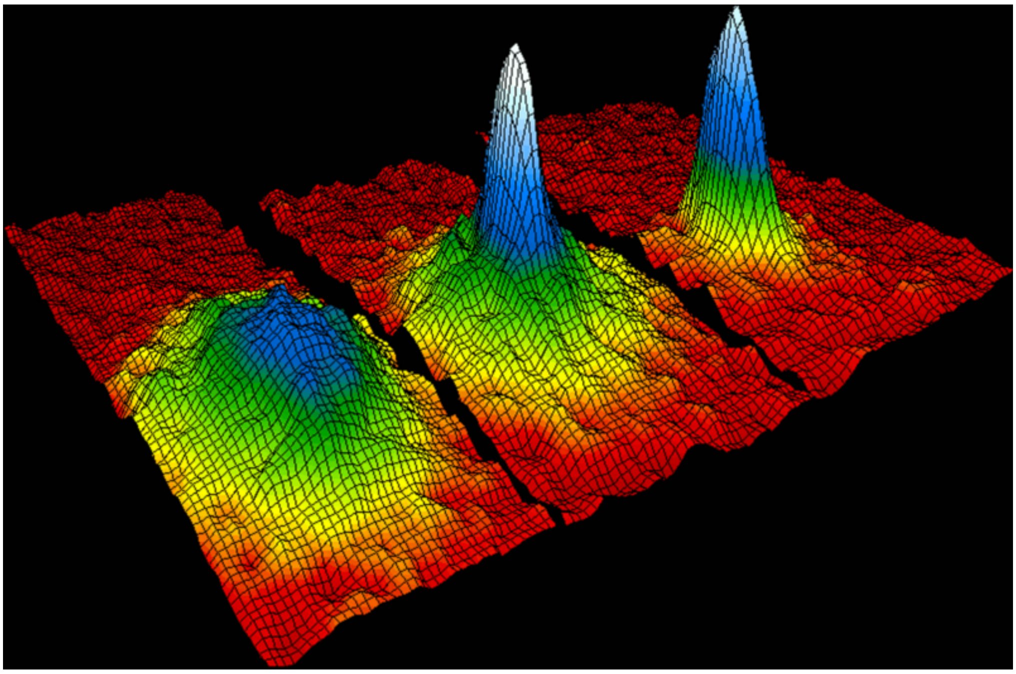

Fig. 1.: Velocity distribution of a vapor of ^{87}Rb at temperatures ~400 nK, ~200 nK, and ~50 nK (from left to right) obtained after ballistic expansion by Cornell and Wieman [11]. Shown is the isotropically expanded thermal cloud (lhs.), the partially condensed sample (center), and the pure condensate (rhs.). The image is taken from [12].

BECs in optical lattices — a versatile tool to study quantum phenomena

An exciting research field resulting from the experimental availability of pure BECs are systems of ultracold bosonic atoms in optical lattices, generated by two counter-propagating lasers. Based on the ac-Stark shift, the optical standing wave is a periodic potential for the atoms. Such a setup was proposed by Jaksch *et al.* [16] to be a perfect realization of the Bose-Hubbard model (BHM) [17–19]. The Hubbard model was formulated by John Hubbard in order to study electrons in narrow energy bands as they appear in solids [20], especially to describe the transition between conducting and insulating systems. In 1989, Fisher *et al.* investigated the BHM in order to describe experiments in which ^{4}He is absorbed by porous materials like Vycor [17]. They investigated the phase diagram of the model at zero temperature, especially the prominent transition from a superfluid phase to a Mott insulating phase, i.e., an insulator induced by the inter-particle interaction. Analogously, Jaksch *et al.* demonstrated in 1998 that the increase of the laser intensity, which leads to in deeper lattice sites, results in a Mott insulating state [16].

The experimental realization of such a strongly correlated system has been achieved by Greiner *et al.* [21] in 2002. They were able to transfer a ultracold cloud of ^{87}Rb atoms

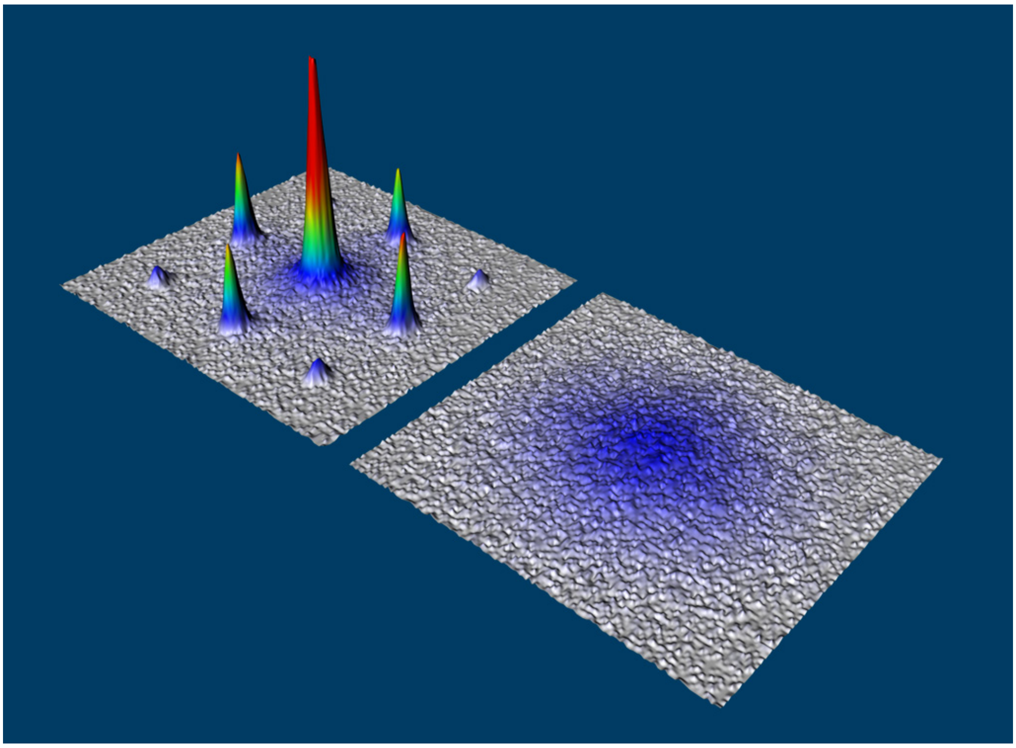

Fig. 2.: Interference pattern after time of flight of an ultracold Bose gas in an optical lattice with the superfluid phase on the left hand side and the Mott insulating phase on the right hand side. The image is taken from [22].

from the superfluid (SF) phase to the Mott insulator (MI) phase by increasing the lattice depth. The superfluid and Mott insulating phase are distinguished by their interference pattern after a time of flight as shown in Fig. 2. The superfluid phase is characterized by a high degree of coherence and shows an interference pattern after release from the lattice, which is similar to the diffraction patterns of coherent light from a grating. In the Mott insulating phase, the atoms are pinned to individual sites and, therefore, lose their phase coherence which is indicated by the absence of interference peaks.

The direct connection between the theoretical model and its experimental realization made ultracold gases in optical lattices an active field of research in the past decade in both, theory [23–34] and experiment [35–39]. The experiment of Greiner *et al.* has been reproduced in various laboratories and has proven as an excellent playground for strongly correlated systems: in analogy to the crystal structure of solids, the atoms in optical lattices represent an artificial crystal of light with similar physics, but with a much better control over all relevant parameters. The phase diagram of the lattice systems exhibits phases of superfluidity and insulation as well as localization and a Bose-glass (BG). Due to the direct access to all control parameters, one can easily "navigate" through the whole phase diagram [33]:

- The laser intensity controls the lattice depth and is, therefore, responsible for the SF-MI phase transition.
- The superposition with a second weaker laser of different wave length introduces spatial inhomogeneities in form of a two-color superlattice [25, 26, 29, 30, 35, 38]. The variation of the strength of the superlattice amplitude gives access to a quasi Bose-glass phase and localization effects [29, 30].
- Feshbach resonances allow to control the inter-particle interaction [40].

The primary observable in experiments is the interference pattern, which serves as the "keyhole" to gain information on the state of the system. For instance, the interference pattern measures the degree of coherence of the particles directly and allows to derive the condensate fraction from the shape of the interference peaks [39]. A much deeper insight into the physics of a quantum system is obtained by going beyond ground-state properties. Such information is provided by spectroscopy, which includes also information on excited states and allows, for instance, to characterize the quantum phase through gaps in the excitation spectrum. Already in the pioneering experiment by Greiner *et al.* the excitation spectrum has been probed by applying a potential gradient [21], i.e., tilting the lattice. Another well-established technique employs a weak temporal modulations of the lattice amplitude [39] in order to perform Bragg spectroscopy [41]. Here, the modulation frequency defines the energy quantum offered to the system, which allows for the precise probing of a specific energy. Experimentally, the response is measured by the broadening of the central interference peak (cf. Fig. 2), which is identified with an energy transfer induced by the modulation [39]. Consequently, the evaluation of the energy transfer for a range of modulation frequencies provides the excitation spectrum. From the excitation spectrum, one can extract the characteristics of the individual quantum phases, such as position and width of the resonance peaks. Based on this technique, the superfluid to Mott-insulator phase transition [25, 27, 28, 39] as well as the transition from the Mott regime into the Bose-glass phase [25, 26, 36] of three- and one-dimensional lattices have been studied experimentally and theoretically. The investigation of these quantum phases as well as the characterization of the transition between them are subject of the present work. We focus on the simulation of the temporal amplitude modulation of a one-dimensional lattice in order to excite the system and evaluate the response by employing various numerical methods.

The outline of the thesis is as follows: In the first chapter, the formal framework is introduced by briefly reviewing the Bose-Hubbard model and its phase diagram. In the second chapter, we employ exact time-evolutions in order to investigate the excitation structure in the strongly interacting regime. Additionally, we introduce a truncation scheme which reduces the model space to the relevant components and enables us to simulate systems of moderate size. Moreover, the dynamical signatures of the transition from the Mott insulating (MI) to the quasi Bose-glass (BG) phase are studied. In the third chapter, we employ particle-hole methods in order to advance to experimentally relevant system sizes. Within the framework of the Tamm-Dancoff approximation, we investigate the transition from the Mott insulating to the superfluid phase as well as the Mott insulator to Bose-glass transition. Furthermore, the application of the random-phase approximation is discussed.

Chapter 1

Ultracold atoms in optical lattices

1.1. Optical lattices

Lasers are essential and valuable tools for the creation and manipulation of Bose-Einstein condensates. Besides their important role for cooling atoms to the μK regime, lasers allow to create optical lattices, which are subject of very active research in the past decade.

Optical lattices are based on the ac-Stark shift in an oscillating electric field, such as the standing wave of two counter-propagating lasers. The field induces an oscillating electric dipole moment in the atom which, at the same time, interacts with the field. This interaction creates a trapping potential which is proportional to the polarizability α of the atom and the intensity $\mathcal{I}$ of the field [43].

The oscillation frequency is far-detuned from resonances of the atom in order to avoid losses by internal excitations. Depending on the detuning relative to the resonance, the atoms experience a force towards the maxima (red detuned) or minima (blue detuned) of the optical lattice.

With a setup of two counter-propagating lasers in each spatial direction one can form a three dimensional lattice for atoms as depicted in Fig. 1.1 (b), where the dots represent the individual lattice sites. In such a three-dimensional lattice, the motion of the atoms is limited to tunneling processes between the sites. By adjusting the intensities of the lasers one can realize various scenarios, like an array of one-dimensional tubes as depicted in Fig. 1.1 (a). Here, the atoms move freely inside the tubes, whereas their motion in

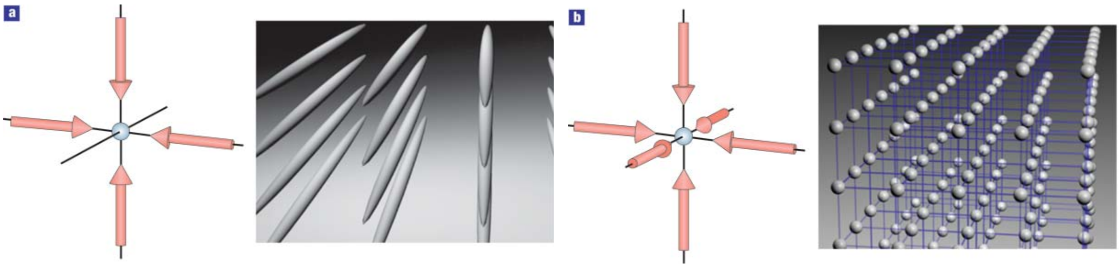

Fig. 1.1.: Array of one-dimensional tubes created by two perpendicular standing laser fields (a) and a 3D lattice by three standing waves in all three dimensions (b). Picture taken from [42].

the other directions is limited to tunneling between the tubes. In 1995 the groups of Cornell and Wieman [11] and Ketterle [13] achieved the experimental realization of a Bose-Einstein condensate with ^{87}Rb and ^{23}Na, respectively. The combination of such a cloud of ultracold atoms and an optical lattice opened a whole new range of opportunities to study quantum effects. In 1998 Jaksch *et al.* proposed that ultracold bosons in optical lattices are perfect realizations of the Bose-Hubbard model [16], which exhibits a quantum phase-transition from a superfluid to Mott-insulating phase [17]. This phase-transition was observed experimentally in 2002 by Greiner *et al.* [21] (cf. Sect. 1.3).

By increasing the laser intensity in two perpendicular directions it is possible to investigate one-dimensional quantum systems. Thereby, the tunneling of the atoms in these directions is strongly suppressed which results in an array of one-dimensional lattices. These one-dimensional lattice systems are subject of the present work.

1.2. Bose-Hubbard model (BHM) in one dimension

1.2.1. Bose-Hubbard Hamiltonian

A fundamental property of the single-particle energies of atoms in a periodic potential is the formation of energy bands which are separated by band gaps [see textbooks like [44]]. The Hubbard model was developed for the description of electrons in a single band of a lattice, assuming that excitations to other bands can be neglected due to sufficiently large band gaps [20].

These requirements are also fulfilled by a gas of ultracold bosonic atoms in an optical lattice. For sufficiently deep lattices, the gap between the bands is large enough that admixtures by states of higher bands can be neglected. We therefore restrict to single-particle states of the first band only, which are represented by localized Wannier functions. As starting point for the derivation of the Bose-Hubbard Hamiltonian we write down the one-dimensional Hamiltonian of a system of bosonic atoms with a contact interaction in an external potential,

$$\mathbf{H} = \int \mathrm{d}x \; \boldsymbol{\psi}^\dagger(x) \left(-\frac{1}{2m} \frac{\partial^2}{\partial x} + V_{\mathrm{lattice}}(x) + V_{\mathrm{trap}}(x) \right) \boldsymbol{\psi}(x) + \frac{g}{2} \int \mathrm{d}x \; \boldsymbol{\psi}^\dagger(x) \boldsymbol{\psi}^\dagger(x) \boldsymbol{\psi}(x) \boldsymbol{\psi}(x). \tag{1.1}$$

The $\boldsymbol{\psi}^\dagger(x)$ and $\boldsymbol{\psi}(x)$ are the bosonic field operators for a given atomic state, $V_{\mathrm{lattice}}(x)$ is the optical lattice potential and $V_{\mathrm{trap}}(x)$ is a slowly varying external potential, such as of a magnetic trap. The coupling constant is given by

$$g = \frac{4\pi a_{\mathrm{s}} \hbar^2}{m} \tag{1.2}$$

with the s-wave scattering length a_{s} and the atomic mass m. The potential generated by the optical lattice reads

$$V_{\mathrm{lattice}}(x) = V_0 \sin^2\left(\frac{2\pi}{\lambda} x \right), \tag{1.3}$$

with the laser wavelength λ and the lattice depth V_0.

The field operators in (1.1) can be expanded in terms of the localized Wannier functions,

$$\boldsymbol{\psi}^\dagger(x) = \sum_{i=1}^{I} \omega_0^*(x - \xi_i)\, \mathbf{a}_i^\dagger \tag{1.4}$$

and

$$\boldsymbol{\psi}(x) = \sum_{i=1}^{I} \omega_0(x - \xi_i)\, \mathbf{a}_i, \tag{1.5}$$

with the number of lattice sites I and the position-space coordinate ξ_i of the ith site. The operators $\mathbf{a}_i^\dagger$ and $\mathbf{a}_i$ create and annihilate, respectively, a boson on the ith site of the lattice and obey the bosonic commutator relations

$$[\mathbf{a}_i^\dagger, \mathbf{a}_j^\dagger] = [\mathbf{a}_i, \mathbf{a}_j] = 0 \quad \text{and} \quad [\mathbf{a}_i, \mathbf{a}_j^\dagger] = \delta_{ij}.$$

We can rewrite the full Hamiltonian by plugging (1.4) and (1.5) into (1.1),

$$\mathbf{H} = \sum_{i,j=1}^{I} J_{ij} \left(\mathbf{a}_i^\dagger \mathbf{a}_j + \mathbf{a}_j^\dagger \mathbf{a}_i \right) + \sum_{i,j=1}^{I} \epsilon_{ij} \mathbf{a}_i^\dagger \mathbf{a}_j + \sum_{i,j,k,l=1}^{I} U_{ijkl} \mathbf{a}_i^\dagger \mathbf{a}_j^\dagger \mathbf{a}_k \mathbf{a}_l, \tag{1.6}$$

with the parameters

$$J_{ij} = \int \mathrm{d}x \, \omega_0^*(x - \xi_i) \left(-\frac{1}{2m} \frac{\partial^2}{\partial x^2} + V_{\text{lattice}}(x) \right) \omega_0(x - \xi_j), \tag{1.7}$$

$$U_{ijkl} = \frac{g}{2} \int \mathrm{d}x \; \omega_0^*(x - \xi_i) \omega_0^*(x - \xi_j) \omega_0(x - \xi_k) \omega_0(x - \xi_l), \tag{1.8}$$

and

$$\epsilon_{ij} = \int \mathrm{d}x \; \omega_0^*(x - \xi_i) V_{\text{trap}}(x) \omega_0(x - \xi_j). \tag{1.9}$$

We assume tunneling between adjacent sites only, and since the lattice potential is invariant under translations by the lattice spacing a, $V_{\text{lattice}}(x) = V_{\text{lattice}}(x + a)$, equation (1.7) simplifies to

$$J = \int \mathrm{d}x \; \omega_0^*(x) \left(-\frac{1}{2m} \frac{\partial^2}{\partial x^2} + V_{\text{lattice}}(x) \right) \omega_0(x - \delta). \tag{1.10}$$

Furthermore, since we assume contact interaction only, we can neglect the interaction of atoms at different sites. Additionally, the interaction is assumed not to be site dependent, so we define $U \equiv U_{1111}$ and simplify (1.8) to

$$U = \frac{g}{2} \int \mathrm{d}x \; |\omega_0(x)|^4. \tag{1.11}$$

Finally, since Wannier functions located at different sites do not overlap too strongly, the off-diagonal contribution of the external potential $V_{\text{trap}}(x)$ can be neglected, hence, (1.9) is approximated by

$$\epsilon_i = \int \mathrm{d}x \; V_{\text{trap}}(x) |\omega_0(x - \xi_i)|^2. \tag{1.12}$$

Based on these considerations we can formulate the final expression of the Bose-Hubbard Hamiltonian,

$$\mathbf{H} = -J \sum_{i=1}^{I} \left(\mathbf{a}_i^\dagger \mathbf{a}_{i+1} + \mathbf{a}_{i+1}^\dagger \mathbf{a}_i \right) + \frac{U}{2} \sum_{i=1}^{I} \mathbf{n}_i (\mathbf{n}_i - 1) + \sum_{i=1}^{I} \epsilon_i \, \mathbf{n}_i, \tag{1.13}$$

with the occupation number operator $\mathbf{n}_i = \mathbf{a}_i^\dagger \mathbf{a}_i$. Tunneling strength J (1.10), interaction strength U (1.11), and external potential ϵ_i (1.12) are the so-called Hubbard parameters. The physics of the Bose-Hubbard model (BHM) is governed by the competition between these parameters.

Band structure

In most cases, we study the properties of the bosonic lattice systems with respect to the Hubbard parameters, i.e., J, U, and ϵ_i. However, these parameters are functions of the experimental control parameters like the lattice depth V_0 and the wave length of the lasers λ. In order to compare the results to experiments, we have to translate the experimental parameters to the Hubbard parameters.

The first step to relate a set of experimental control parameters to the Hubbard parameters is to calculate the localized Wannier functions for the given lattice. This is achieved by evaluation of the Bloch functions based on the Bloch theorem [45], which describes delocalized single-particle states $\psi_q(x)$ with the quasimomentum q. Within a single band, the Bloch functions are related to the localized Wannier functions $w_0(x-\xi_i)$ via Fourier transformation. The Wannier functions are then plugged into the integrals (1.10) to (1.12) in order to evaluate the Hubbard parameters [33].

1.2.2. Number basis representation

A many-body state in the model space of the Bose-Hubbard model can be described in the occupation number representation. The basis states are characterized by I-tuples of integer numbers $\{n_1,\cdots,n_I\}$, which refer to the number of atoms in localized single-particle state at the individual sites. Since we assume a fixed number of sites I and particles N, the number basis is spanned by all compositions of N particles on I sites,

$$\big|m\big\rangle = \big|\{n_1,\cdots,n_I\}_m\big\rangle. \tag{1.14}$$

For an arbitrary state of the number basis we will also use the symbol $\big|n_1,\cdots,n_I\big\rangle$ for simplicity. The number basis is *orthogonal*

$$\big\langle n_1,\cdots,n_I\big|n'_1,\cdots,n'_I\big\rangle = \delta_{n_1 n'_1}\cdots\delta_{n_1 I n'_I} \tag{1.15}$$

and *complete* in the model space

$$\sum_{\{n_1,\cdots,n_I\}} \big|n_1,\cdots,n_I\big\rangle\big\langle n_1,\cdots,n_I\big| = \mathbf{1} \tag{1.16}$$

and the dimension is given by

$$D = \frac{(N+I-1)!}{N!(I-1)!}. \tag{1.17}$$

The latter expression reveals the strong factorial growth of the model space with the number of particles and sites, which is illustrated in Fig. 1.2. In the experiment of Stöferle *et al.* [39] $1.5{\cdot}10^5$ particles were in the cloud, which makes about $\sqrt[3]{1.5\cdot10^5} \approx 50$ particles

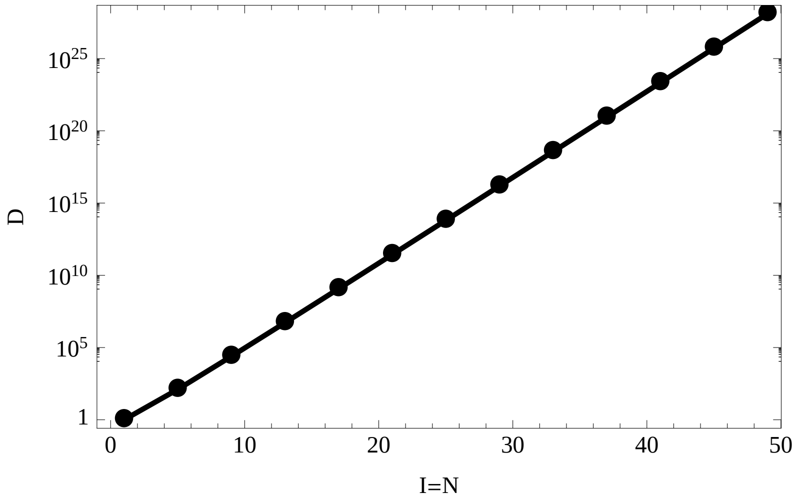

Fig. 1.2.: Model-space dimension as function of the number of particles N and number of sites $I = N$.

in a single one-dimensional tube. The model space for such a system is of the dimension $D \approx 50 \cdot 10^{27}$, which is not feasible numerically in view of exact diagonalization to solve the Schrödinger equation. In order to handle such system sizes we introduce two approximative methods in chapters 2 and 3.

Finally, we have to define how the the bosonic creation and annihilation operators $\mathbf{a}_i^\dagger$ and $\mathbf{a}_i$ of the Bose-Hubbard Hamiltonian (1.13) act on the states of the number basis. These operators obey the bosonic commutator relations,

$$[\mathbf{a}_i^\dagger, \mathbf{a}_j^\dagger] = [\mathbf{a}_i, \mathbf{a}_j] = 0 \quad \text{and} \quad [\mathbf{a}_i, \mathbf{a}_j^\dagger] = \delta_{ij}.$$

The creation operator $\mathbf{a}_i^\dagger$ creates a boson on the ith site,

$$\mathbf{a}_i^\dagger \left|n_1, \cdots, n_i, \cdots, n_I\right\rangle = \sqrt{n_i + 1} \left|n_1, \cdots, n_i + 1, \cdots, n_I\right\rangle \tag{1.18}$$

and the annihilation operator $\mathbf{a}_i$ annihilates a particle at site i

$$\mathbf{a}_i \left|n_1, \cdots, n_i, \cdots, n_I\right\rangle = \sqrt{n_i} \left|n_1, \cdots, n_i - 1, \cdots, n_I\right\rangle. \tag{1.19}$$

An arbitrary state in the number basis is given by

$$\left|\psi\right\rangle = \sum_{m=1}^{D} c_m^{(\psi)} \left|\{n_1, \cdots, n_I\}_m\right\rangle, \tag{1.20}$$

and thus defined by the complex expansion coefficients $c_m^{(\psi)}$ with $\sum_{m=1}^{D} |c_m^{(\psi)}|^2 = 1$.

The coefficients $c_m^{(\nu)}$ of the energy eigenstates $\left|E_\nu\right\rangle$ are obtained by solving the stationary Schrödinger equation,

$$\mathbf{H}\left|E_\nu\right\rangle = E_\nu \left|E_\nu\right\rangle. \tag{1.21}$$

This is achieved numerically by the diagonalzation of the Bose-Hubbard Hamilton matrix in number basis representation. It should be emphasized at this point, that the solution of the Schrödinger equation for the full model space of a system of experimental relevant sizes is not feasible. We present therefore a truncation scheme in chapter 2, which allows to reduce the model space dimension to the relevant subspace.

1.3. Quantum phases, phase transitions and simple observables

1.3.1. Superfluid to Mott insulator phase transition

About ten years before Jaksch *et al.* [16] found the perfect realization of the Bose-Hubbard model (BHM) in systems of ultracold bosons in optical lattices, Fisher *et al.* showed, that the BHM exhibits a quantum phase transition from the superfluid (SF) to the Mott-insulating (MI) phase [17].

In order to review the ground states in the two quantum phases, we consider a system of N bosons on $I = N$ sites of a homogeneous lattice. The Hamiltonian describing this system reads

$$\mathbf{H} = -J \sum_{i=1}^{I} \left(\mathbf{a}_i^\dagger \mathbf{a}_{i+1} + \mathbf{a}_{i+1}^\dagger \mathbf{a}_i \right) + \frac{U}{2} \sum_{i=1}^{I} \mathbf{n}_i (\mathbf{n}_i - 1). \tag{1.22}$$

For strong interactions, U dominates over the tunneling strength J. Thus, the tunneling of the atoms between sites is strongly suppressed and due to the strong on-site interaction the atoms are pinned to individual sites in the ground state. The system is in the Mott insulating state, i.e., the atoms are localized purely by interaction [46]. The system can be described approximately by a single number state with one particle per site,

$$\left|0, \mathrm{MI}\right\rangle \approx \left|1, \cdots, 1\right\rangle. \tag{1.23}$$

Due to the dominating interaction strength the tunneling processes can be neglected and the Hamilton operator reduces to the interaction term. Since the interaction term consists of the occupation-number operator $\mathbf{n}_i$ only, the Hamiltonian is diagonal in this limit. Hence, the eigenbasis is spanned by the number states. This situation is illustrated in the plots (a) and (b) of Fig. 1.3 for a system of 6 bosons on 6 sites. Plot (a) shows the Hamilton matrix in the number basis representation and (b) the energy spectrum with the fully degenerate Hubbard bands. The gapped band structure is a signature of the MI phase.

The states in the individual bands belong to certain classes of number states. As mentioned above, the ground state consists of the number state with one particle per site, and has, therefore, zero energy. The energetically next number state has exactly one doubly occupied site, which corresponds to the energy U. All number states with one double occupation form the first Hubbard band. The next band is composed by states with two double occupations, and so on. For an increase of the tunneling strength off-diagonal elements arise in the Hamilton matrix in Fig. 1.3 (c) for $U/J = 40$. These off-diagonal elements lift the degeneracy of the energy eigenstates as visible in Fig. 1.3 (d). The structure of the eigenstates is still comparable to that of the system with a vanishing J, but they have small admixtures from all other number states. A further decrease of the ratio U/J to 20 implies stronger off-diagonal matrix elements of the Hamiltonian in 1.3 (e), which causes a further broadening of the bands in (f). Finally, when the tunnel-

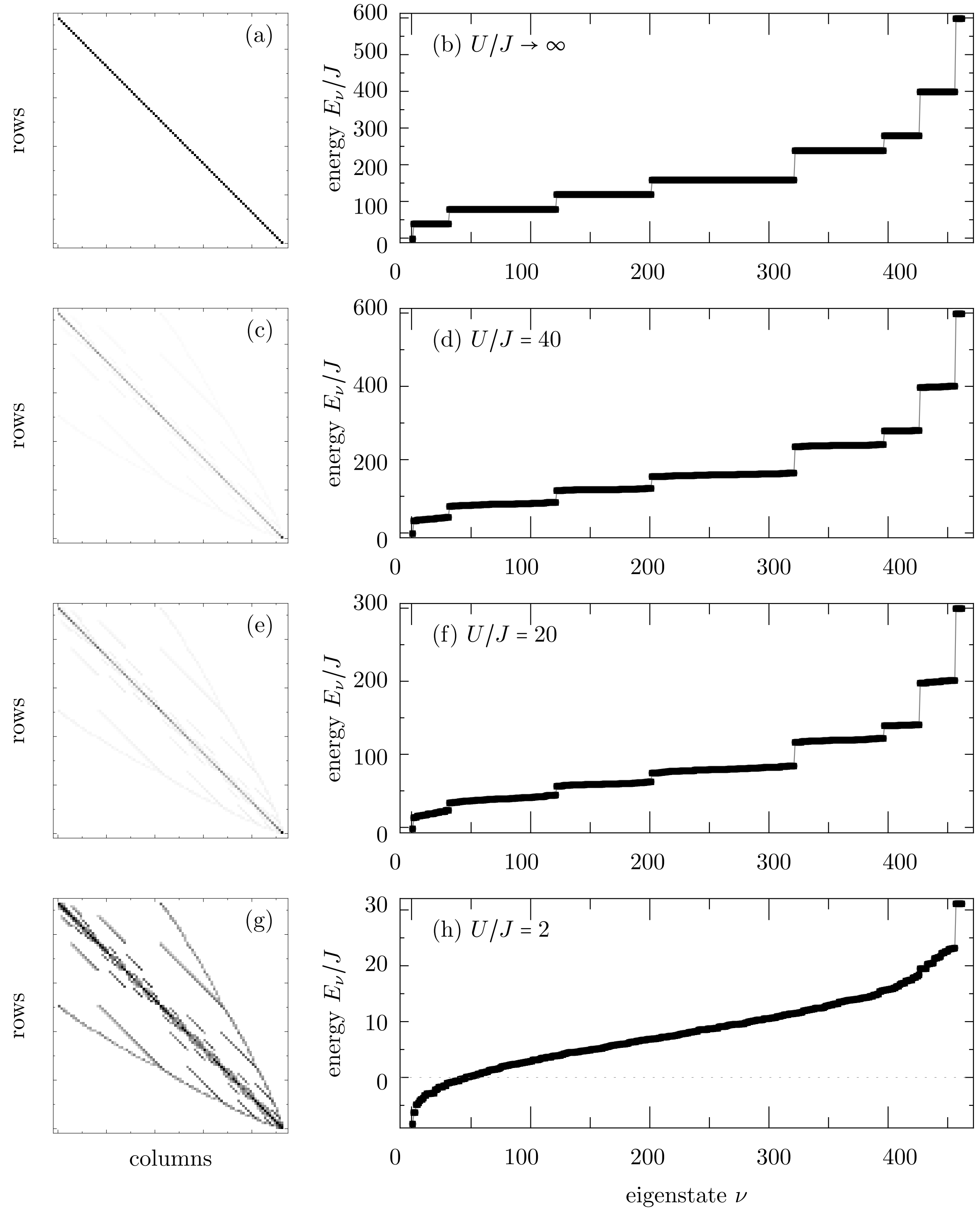

Fig. 1.3.: From strong interaction to superfluidity: Shown is the structure of the Hamilton matrix (left column) and the corresponding energy spectrum (right column) of a system with $N = I = 6$ and the ratios $U/J \to \infty$, U/J=40, 20, and 2 (top to bottom).

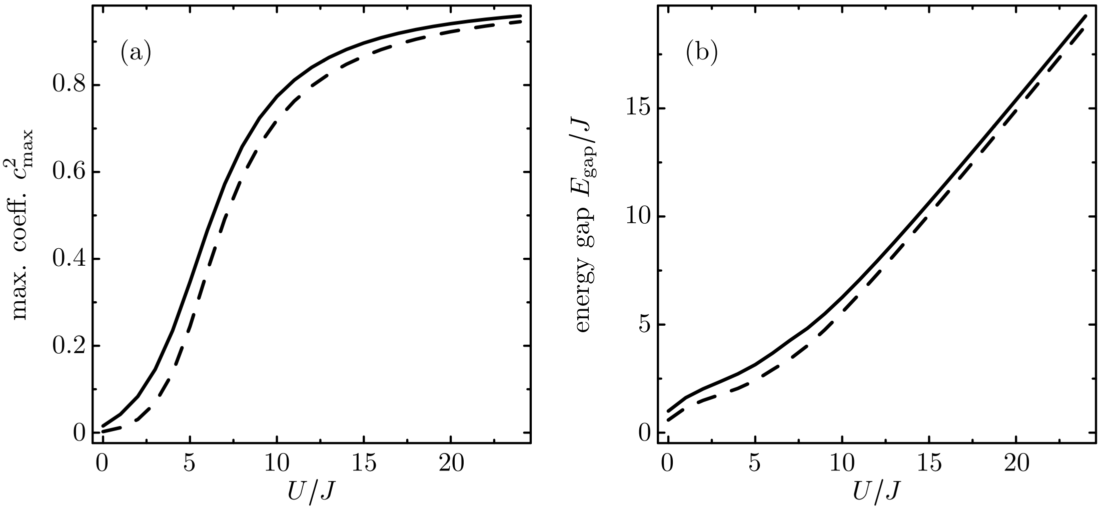

Fig. 1.4.: Maximum coefficient $c^2_{\max}$ (a) and energy gap $E_{\text{gap}} = E_1 - E_0$ (b) as function of U/J. Shown are the results for a system with 6 bosons on 6 sites (——) and 8 bosons on 8 sites (– – –).

ing and the interaction are of comparable strength (g), the gapped band structure has completely vanished (h), which is a signature of the superfluid phase. The critical ratio of tunneling and interaction strength for the quantum phase transition is determined to $(U/J)_c \approx 4.65$ via Monte-Carlo calculations [47,48] and $(U/J)_c = 3.3 \pm 0.1$ in recent calculations [32] employing the DMRG method (density-matrix renormalization group method) [28,33,49,50].

1.3.2. Observables

The phase transition manifests itself in various observables in the calculations, but many of them are not available in the experiment. In the following we will present two simple observables, which we have already used in the previous discussion of the characteristics of the quantum phases, i.e., the maximum expansion coefficient of the number basis expansion of the ground state $c^2_{\max}$ and the energy gap E_{gap}. Both observables are not directly accessible in experiments. Finally, we introduce the most important experimental observable, which is the matter-wave interference-pattern.

Maximum expansion coefficient

The maximum coefficient of the number basis expansion of the ground state shows a distinct signature in each of the phases. In the strongly interacting regime, i.e., $U \gg J$, where the atoms are pinned to individual lattice sites, the ground state can be described by a single number state $|0, \text{MI}\rangle \approx |1, 1, \cdots, 1\rangle$. All other number states include multiple occupations of sites and have, therefore, extremely weak contributions to the ground state. Hence, the absolute square of the coefficient of this number state is close to 1, i.e., the MI phase is characterized by a large maximum coefficient $c^2_{\text{max}} = \max(\{|c^{(0)}_m|^2\})$.

On the other hand, in the superfluid regime the atoms are spread over the whole lattice and the ground state is a superposition of all number states. Since all number states are of comparable importance to the ground state, the maximum coefficient c^2_{max} is rather small in the SF phase.

Figure 1.4 (a) illustrates the maximum coefficient as function of the interaction strength for a system of 6 bosons on 6 sites and 8 bosons on 8 sites. For weak interactions, the system shows a small maximum coefficient which rapidly increases in the region of the phase transition $U/J = 3 - 7$. Towards infinite ratios $U/J \to \infty$ the maximum coefficient converges to one, $c^2_{\text{max}} \to 1$.

Energy gap

Another observable is the energy gap E_{gap}. Figures 1.3 (e) to (g) show the energy spectrum of a systems in the MI regime, which is characterized by a gapped structure. On the other hand, one observes a gapless energy spectrum in the superfluid phase in Fig. 1.3 (h).

We define, therefore, the energy gap E_{gap} as the difference between the ground state energy E_0 and the energy of the first excited state E_1,

$$E_{\text{gap}} = E_1 - E_0, \tag{1.24}$$

which we obtain by solving the Schrödinger equation. Figure 1.4 (b) shows the energy gap as function of the interaction strength for the 6 and 8 boson system. The curves show a small energy gap for weak interactions and a slight kink in the transition region, after which they increase linearly with U/J.

Matter-wave interference-pattern

The primary experimental observable is the matter-wave interference pattern of the atoms after release from all confining potentials and a ballistic expansion. After a certain time of expansion a picture is taken of the cloud after a *time-of-flight* (TOF). The shadow resulting from the absorption of resonant light shows the density distribution of the particles in the cloud. Since particles with higher momentum cover a larger distance during the expansion time, this interference pattern shows the momentum distribution before the release of the cloud.

In the pioneering experiments on the observation of the superfluid to Mott insulator phase transition [21], the two regimes were identified by this method. Figure 1.5 depicts the interference patterns observed at different stages of the transition between both regimes in a three dimensional lattice.

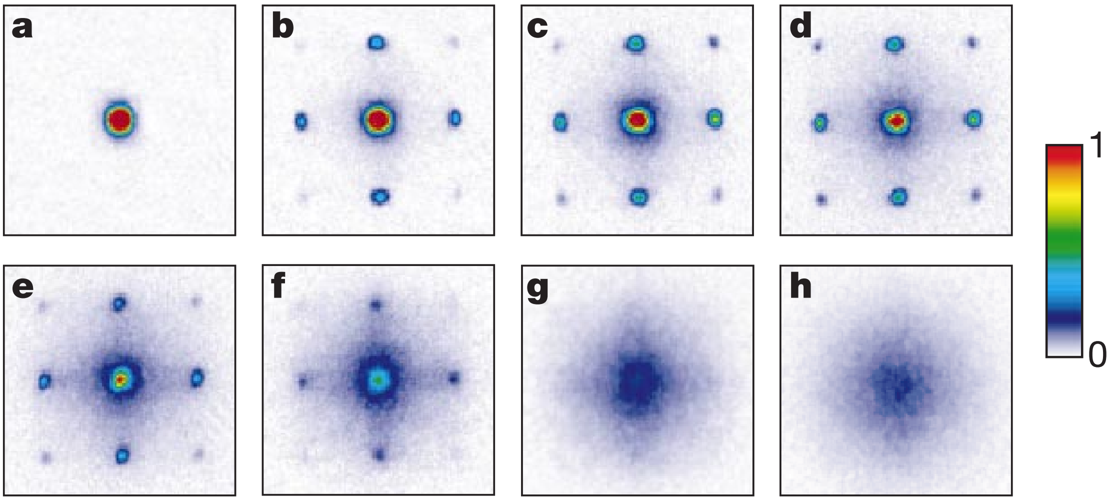

Fig. 1.5.: Evolution of the matter-wave interference-pattern in the experiment by Greiner *et al.* [21]. Shown is the evolution from the superfluid (a) to the Mott insulator phase (h) in a 3D optical lattice. The lattice depths V_0 are (a) 0 E_R, (b) 3 E_R, (c) 7 E_R, (d) 10 E_R, (e) 13 E_R, (f) 14 E_R, and (h) 16 E_R. The image is taken from [21].

Figure 1.5 (a) shows the interference pattern of the atomic cloud in the absence of the lattice potential. All atoms are condensed in the lowest energy state and the interference pattern shows a strong central peak. For a weak lattice, higher order interference peaks arise (b)-(d), which reflect the high degree of coherence of the atoms. The emergence of the higher-order peaks. For a lattice depth of $V_0 = 13\ \mathrm{E_R}$[1] in (e), the interference structure gets weaker and an incoherent background emerges. For further increase of the lattice depth the interference structure vanishes completely (f)-(g). The atoms are isolated from each other and have lost their phase coherence and one observes the incoherent background only.

To derive the matter-wave interference-pattern for a one-dimensional lattice system we start with the Bloch functions. The Bloch theorem [45] states, that the eigenfunctions of a Hamiltonian with a periodic potential are of the form

$$\psi_{q,b}(x) = \exp(-\mathbf{i}qx)u_{q,b}(x), \tag{1.25}$$

with the function $u_{q,b}(x)$, which has the same periodicity as the potential. In general, the functions $\psi_{q,b}(x)$ and $u_{q,b}(x)$ carry the index of the band b, but since we are focusing on the first band only, we omit it in the following. The $\psi_q(x)$ are the single-particle quasi-momentum eigenfunctions in the lowest band $b = 0$.

---

[1] The recoil energy E_R is defined by $E_\mathrm{R} = \hbar^2k^2/(2m)$, with the wave number k of the lattice and the mass m of the atoms. The recoil energy defines an energy scale of theses systems.

Within a single band, the Bloch functions can be Fourier transformed into the conjugated representation of localized Wannier functions $w(x-\xi_i)$ [51],

$$\psi_q(x) = \frac{1}{\sqrt{I}} \sum_{i=1}^{I} \exp(-\mathbf{i}q\xi_i)\omega(x-\xi_i). \tag{1.26}$$

The operators $\mathbf{a}_i^\dagger$ ($\mathbf{a}_i$) of the BHM create (annihilate) a boson in the Wannier state corresponding to $w(x-\xi_i)$, hence, equation (1.26) can be used to define the creation and annihilation operators of a boson in the Bloch state with quasi momentum q,

$$\mathbf{c}_q^\dagger = \frac{1}{\sqrt{I}} \sum_{i=1}^{I} \exp(-\mathbf{i}q\xi_i)\mathbf{a}_i^\dagger, \tag{1.27}$$

and

$$\mathbf{c}_q = \frac{1}{\sqrt{I}} \sum_{i=1}^{I} \exp(\mathbf{i}q\xi_i)\mathbf{a}_i, \tag{1.28}$$

respectively. Analogously to the definition of the mean occupation number operator $\mathbf{n}_i = \mathbf{a}_i^\dagger \mathbf{a}_i$ of a site i, one can define the occupation number operator of a quasi momentum state via $\mathbf{n}_q = \mathbf{c}_q^\dagger \mathbf{c}_q$. The mean occupation number of the quasi momentum q in the state $|\psi\rangle$ is then given by

$$n_q = \langle\psi|\,\mathbf{c}_q^\dagger \mathbf{c}_q|\psi\rangle = \frac{1}{I} \sum_{i,j=1}^{I} \exp[\mathbf{i}(\xi_i - \xi_j)q]\langle\psi|\,\mathbf{a}_j^\dagger \mathbf{a}_i\,|\psi\rangle, \tag{1.29}$$

with the matrix elements of the one-body density matrix $\rho_{ij}^{(1)} = \langle\psi|\,\mathbf{a}_j^\dagger \mathbf{a}_i\,|\psi\rangle$. The coordinate in position space in (1.29) has been substituted by $\xi_i = ai$, with the lattice spacing a. Equation (1.29) can now be written in the compact form

$$n_q = \frac{1}{I} \sum_{i,j=1}^{I} \exp[\mathbf{i}(i-j)aq]\,\rho_{ij}^{(1)}. \tag{1.30}$$

The latter expression can be generalized to the intensity of the matter-wave interference pattern $\mathcal{I}(\delta)$ by allowing continuous values δ rather than discrete ones aq in the exponential of (1.30),

$$\mathcal{I}(\delta) = \frac{1}{I} \sum_{i,j=1}^{I} \exp[\mathbf{i}\delta(i-j)]\,\rho_{ij}^{(1)}. \tag{1.31}$$

Figure 1.6 illustrates typical intensities of the matter-wave interference pattern for a system in the superfluid regime (a) and (b) and the Mott insulating regime (c) and (d). In the superfluid regime, most bosons are condensed to the lowest quasi momentum state with $q = 0$ which results in a sharp peak of the interference pattern at $\delta = qa = 0$. On the other hand, in the Mott regime the bosons are pinned to individual sites and are

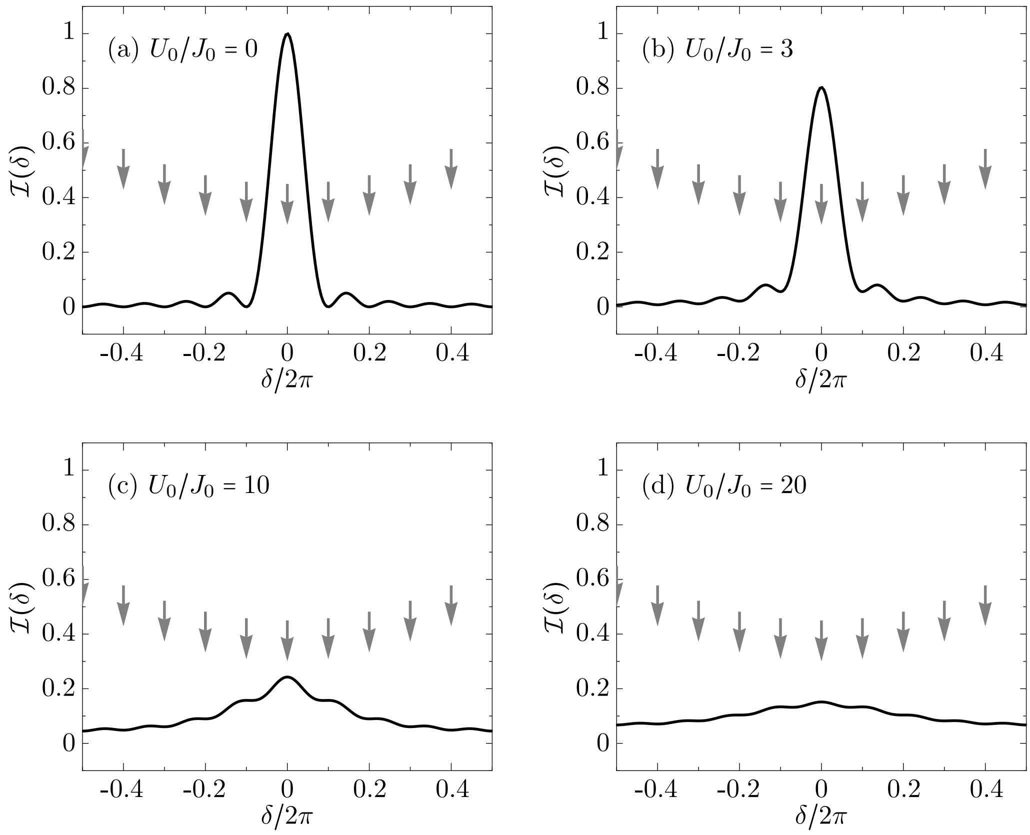

Fig. 1.6.: Intensity $\mathcal{I}(\delta)$ matter-wave interference pattern as function of the phase δ of a system with $I = N = 10$. Shown are the results for the superfluid phase (a) and (b) and the Mott-insulating phase (c) and (d). The gray arrows mark phases δ which correspond to the quasi momenta via $\delta = qa$.

therefore strongly localized, which results in a broad quasi momentum distribution.

1.3.3. Superlattice potentials

The inclusion of disorder into a lattice system gives rise to additional effects and quantum phases. Such inhomogeneous lattices allow for the study of phenomena well known from solid state physics, like localization effects [52] and the formation of a Bose-glass phase.

A simple approach to introduce inhomogeneities is the superposition of the lattice laser with the wavelength λ_1 with a laser of a weaker intensity and a different wavelength λ_2 [25,26,30,36]. This superposition results in a spatial modulation as depicted in Fig. 1.7 (a) for a one-dimensional setup. Due to the two wavelengths (*colors*) involved these setups are the so-called *two-color superlattices.* The gray dots in the minima represent the

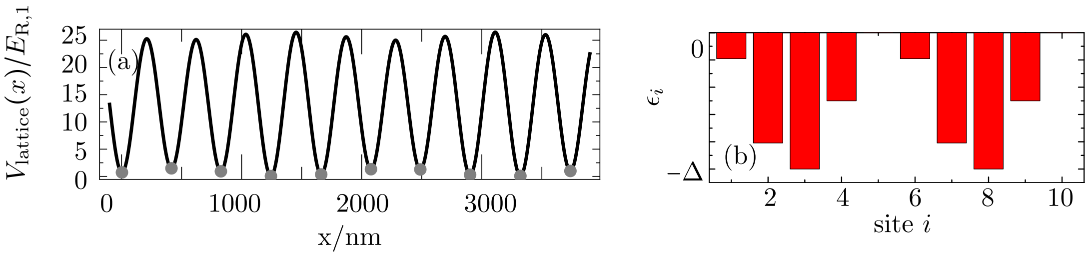

Fig. 1.7.: A two-color superlattice realized with the superposition of the standing waves of two lasers (a). The parameters correspond to the experiment by Fallani *et al.* *et al.* [36] with the wave lengths $\lambda_1 = 830$ nm and $\lambda_2 = 1076$ nm and the lattice depths $V_1 = 16$ $\mathrm{E}_{\mathrm{R},1}$ and $V_2 = 2.5$ $\mathrm{E}_{\mathrm{R},2}$ and a gas of ^{87}Rb . The gray dots in the minima of the wave field in (a) represent the lattice sites and their energetic defines the structure of the on-site potential parameters ϵ_i in (b).

sites of the superlattice. The offset energies between the lattice sites define the on-site potential parameter ϵ_i of the Bose-Hubbard Hamiltonian. Figure 1.7 (b) shows the distribution of the on-site potential parameters ϵ_i for a period-five two-color superlattice. The parameter Δ defines the amplitude of the superlattice modulation.

The amplitude of the superlattice Δ adds another dimension to the phase diagram shown in Fig. 1.8 and gives rise to additional quantum phases. The density plot in Fig. 1.8 shows the maximum coefficient c^2_{max} of the number basis expansion of the ground state as function of the interaction strength U and superlattice amplitude Δ. Lighter shadings refer to small coefficients and darker shadings to larger coefficients.

The line defined by $\Delta = 0$ in Fig. 1.8 corresponds to the superfluid to Mott insulator phase transition in a homogeneous lattice, the SF phase corresponds to a small coefficient c^2_{max} and the MI phase to a larger one.

Superfluid phase. For values of U and Δ comparable to the tunneling strength J, the system is in the superfluid phase, and the wave function of the bosons is spread over the whole lattice [cf. schematic in Fig. 1.8 (a)]. As discussed earlier, this delocalization of the particles is reflected in the structure of the ground state by contributions of all number states, which results in a small maximum coefficient c^2_{max}.

Homogeneous Mott-insulator phase (MI). For $U/J > (U/J)_c$ and $\Delta < U$ the system is in the homogeneous Mott regime, which is characterized by a large maximum coefficient c^2_{max}. In this regime, the system is dominated by the interaction strength and the ground states strongest contribution comes from the number state with one particle per site [cf. schematic in Fig. 1.8 (b)].

(Quasi) Bose-glass phase (BG). By increasing the superlattice amplitude to $\Delta \approx U$ one

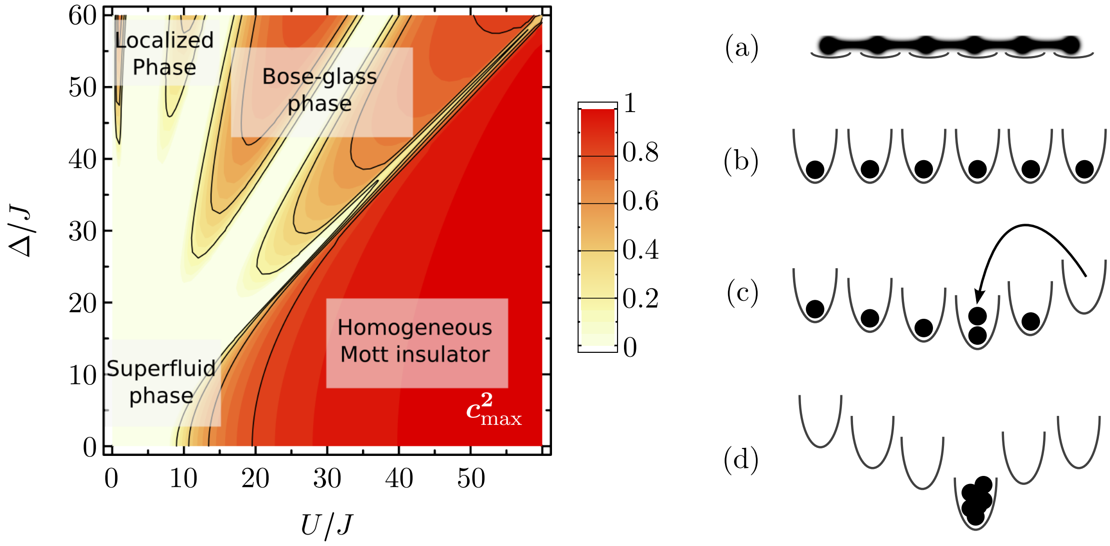

Fig. 1.8.: Phase diagram of a system of 10 bosons on 10 sites of an optical superlattice spanned by the interaction strength U/J and the superlattice amplitude Δ/J. Plotted is the maximum coefficient c^2_{max} of the number basis expansion of the ground state.

arrives at the boundary to the *Bose-glass phase*. At this boundary, the number states with one particle per site and that with two particles in the deepest well are energetically equal. This degeneration results in a decrease of the maximum expansion coefficient, which manifests in the light shaded valley along the $U = \Delta$-line in Fig. 1.8.

At this point, a severe change in the structure of the ground state occurs. The system comes from the domain, where the ground state was dominated by the number state with one particle per site into the domain, where the lowest well is doubly occupied [cf. schematic in Fig. 1.8 (c)]. In this domain, the number state with the deepest well doubly occupied has the strongest contribution to the ground state, which causes the first lobe of large c^2_{max} above the $U = \Delta$-line.

For a further increase of the superlattice amplitude Δ the difference in the potential energy of another pair of sites becomes comparable to the interaction, and another domain change is triggered. In the transition regime between the domains the maximum coefficient drops again due to the energetic degeneration of the two competing number states.

This change in the dominating number state continues for increasing Δ until all particles are located in the deepest wells. The islands of insulating phases above the $U = \Delta$-line are the so-called Mott lobes of the quasi Bose-glass phase.

The structure of the quasi Bose-glass phase depends directly on the structure of the on-site potential parameters ϵ_i. The phase is called *quasi* Bose-glass since a Bose-glass requires true disorder. In a random lattice, the change between the domains occurs continuously since the energy offsets are continuous rather than discrete.

Localized phase. The fourth prominent region of the phase diagram is the localized phase, which occurs for $U \ll \Delta$. In this regime, all particles are located in the deepest well, since due to the weak U the total interaction energy on this site does not exceed the total potential energy [cf. schematic in Fig. 1.8 (d)].

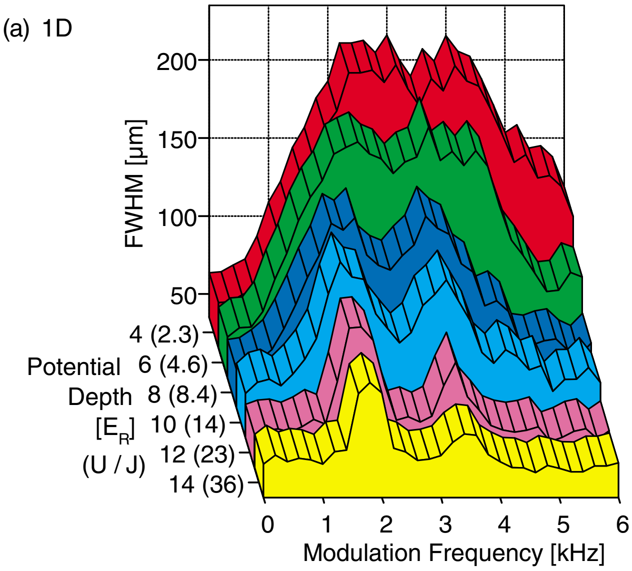

Fig. 1.9.: Full width half maximum of the central interference peak as function of the modulation frequency of the lattice amplitude of a ultracold bosonic gas in one dimension. Shown is the response for interaction strengths in the range from $U/J = 2.3$ to 36 from the experiment by Stöferle *et al.* [39].

1.4. Probing the energy spectrum by lattice modulation

In Sect. 1.3.2, we have presented a few simple observables which show characteristic signatures of the superfluid and the Mott insulating phase. Another approach is to probe the energy spectrum by exciting the system and measuring the response.

Experimentally, this is done by two-photon Bragg spectroscopy [41], which can be realized in optical lattices by an amplitude modulation of the lattice laser [36, 39]. The modulation frequency ω defines the energy quanta $\hbar\omega$ of the excitation.

In experiments, the broadening of the central interference peak visible after a time of flight is related to the amount of energy transferred into the gas. Hence, one can measure the response of a gas by evaluating the width of the central interference peak as function of the modulation frequency of the lattice amplitude.

Stöferle *et al.* performed this experiment with a gas of ^{87}Rb atoms in one- and three-dimensional lattices [39]. Figure 1.9 shows the width (full width – half maximum) as function of the modulation frequency of the one-dimensional system at zero temperature in the range from $U/J = 2.3$ to 36.

In the superfluid regime, they observed a broad resonance and a structure of narrow peaks in the Mott insulator phase. The response structures exhibit direct information on the energy spectrum: the discrete peaks one observes for certain modulation frequencies in the Mott regime signal a gapped energy spectrum, whereas the broad excitation in the superfluid phase is in accordance to the continuous distribution of the eigenenergies (cf. Fig. 1.3).

In the following two chapters, we simulate the lattice modulation and analyze the response of the systems numerically. We focus on the strongly interacting regime of one-dimensional systems and introduce approximations, which enable us to treat system of experimentally relevant size. Our aim is to find signatures of the individual quantum phases in the low-lying excitations induced by weak lattice-amplitude modulations.

Chapter 2

Exact methods

In the following chapter, the dynamics of ultracold Bose gases in optical lattices is studied based on exact methods. In the first section, the explicit time-evolution is briefly reviewed with regard to the Bose-Hubbard model and the amplitude modulation of the optical lattice. Moreover, the linear response analysis is introduced as a complementary tool for studies of the lattice systems in the strongly interacting regime.

In order to treat moderate system sizes, we introduce the *importance truncation* of the number basis, which allows us to reduce the Hilbert space to a subspace spanned by the most important basis states for a given Hamiltonian. In the final part of this chapter we simulate homogeneous lattice systems as well as two-color superlattices in order to extract their response to amplitude modulations. Furthermore, we investigate the quasi-momentum distribution at the resonance to get a deeper understanding on the underlying excitation processes.

2.1. Time evolution

2.1.1. General notes

A straight-froward way to study time-dependent phenomena in quantum systems is to perform an explicit time evolution. More precisely, one has to prepare an initial state and track its time evolution driven by the Hamilton operator using the time-dependent Schrödinger equation

$$\mathbf{i}\frac{d}{dt}\left|\psi,t\right\rangle = \mathbf{H}\left|\psi,t\right\rangle. \tag{2.1}$$

In the case of a time-independent Hamilton operator, the time-evolution operator

$$\mathbf{U}(t,t_0) = \exp[-\mathbf{iH}(t-t_0)] \tag{2.2}$$

solves the Schrödinger equation using $|\psi,t\rangle = \mathbf{U}(t,0)\,|\psi,t=0\rangle$ with the initial state $|\psi,0\rangle$. For time-dependent Hamilton operators one has to keep in mind, that the Hamiltonians at different times t do not commute in general. In this case, one has to introduce a time-ordering operator $\mathbf{T}$.

Nevertheless, if the time intervals Δt (which do not have to be equidistant) are chosen sufficiently small, the Hamiltonian can be approximated as piecewise constant. The time evolution of an initial state $|\psi,0\rangle$ is then given by applying a string of operators $\mathbf{U}_n \equiv \mathbf{U}(t_{n+1},t_n)$,

$$\begin{aligned}|\psi,t=n\Delta t\rangle &= \mathbf{U}_n \cdots \mathbf{U}_1\,|\psi,t=0\rangle\\ &= \exp(-\mathbf{iH}_n\Delta t)\cdots\exp(-\mathbf{iH}_1\Delta t)\,|\psi,t=0\rangle,\end{aligned}$$

with the index n counting the time steps. The operators $\mathbf{U}_n$ ($\mathbf{H}_n$) represent the constant time-evolution operator (Hamilton operator) in the time interval $\Delta t = t_{n+1} - t_n$. By applying the time-evolution operators sequentially, one has access to the systems state at each time step t_n and can thus evaluate all observables at these times.

2.1.2. Lattice modulation in the Bose-Hubbard model

The aim of the studies presented in this work is to obtain the response function of a system of ultracold bosons in an optical lattice induced by a temporal modulation of the lattice amplitude. The time-dependence of the lattice amplitude enters the Bose-Hubbard model via the parameters J and U [equations (1.10) and (1.11)]. In order to obtain the time-dependent expressions for these parameters, the localized Wannier states are approximated by Gaussians of the width σ [53]. The optimal value for the time-dependent width $\sigma(t)$ is obtained by minimizing the energy in the potential

$$V(x,t) = V_0[1+F\sin(\omega t)]\sin^2(kx). \tag{2.3}$$

Computation of the matrix elements of the tunneling energy (1.10) and the interaction part (1.11) of the first-quantized Hamiltonian within this Gaussian approximation leads to the time-dependent Hubbard parameters. For the interaction strength one gets

$$U(t) = U_0[1+F\sin(\omega t)]^{1/4} \tag{2.4}$$

and

$$J(t) = J_0\exp[-F\sin(\omega t)] \tag{2.5}$$

for the tunneling parameter according to [53]. In the lowest order, the temporal change of the on-site energies is directly given by the change of the potential $V_{\text{lat}}(x,t)$, i.e.,

$$\epsilon_i(t) = \epsilon_{i,0}[1+F\sin(\omega t)]. \tag{2.6}$$

By substituting the static parameters with the dynamic ones shown here we obtain the time-dependent Bose-Hubbard Hamiltonian.

For our simulations we take the ground state corresponding to J_0 and U_0 as initial state. The ground state is obtained by diagonalisation of the Hamilton matrix represented in the number state basis. In later sections, we will introduce truncated number bases. The ground state is then obtained by solving the Schrödinger equation in this effective space.

Starting from the initial state, the system is evolved in time steps Δt while modulating the lattice with a fixed frequency ω and relative amplitude F. The frequency ω defines the probe energy and the response of the system is measured by evaluating observables using the time-evolved state $|\psi, t\rangle$. For sufficiently small time-steps Δt the Hamiltonian can be assumed to be constant in this interval, which allows to perform the stepwise evolution as presented in the previous subsection.

2.1.3. Evaluation of the response

In order to obtain the response function of a system of N bosons in a lattice of I sites we assume a fixed interaction strength U_0/J_0, and evaluate the ground state $|E_0\rangle$ of the system by solving the stationary Schrödinger equation. The ground state is used as the initial state $|\psi, t=0\rangle = |E_0\rangle$ of the time-evolution. With the time-dependent Hubbard parameters presented in the previous section we can write down the time-dependent Hamiltonian

$$\mathbf{H}(t) = -J(t)\sum_{i=1}^{I}\left(\mathbf{a}_i^\dagger \mathbf{a}_{i+1} + \mathbf{a}_{i+1}^\dagger \mathbf{a}_i\right) + \frac{U(t)}{2}\sum_{i=1}^{I}\mathbf{n}_i(\mathbf{n}_i - 1) + \sum_{i=1}^{I}\epsilon_i(t)\mathbf{n}_i. \tag{2.7}$$

The time interval of the simulation is sliced in small pieces of Δt, which have to be chosen small enough to sample the oscillations in (2.7) appropriately. According to the Nyquist-Shannon sampling theorem, the sampling frequency has to be at least twice as large as the frequency of the signal. This means for the simulations, that Δt has to be smaller or equal of half of the smallest modulation period, which is ensured for all our simulations.

To evolve the system we evaluate the time-evolution operator $\mathbf{U}_n$ for the interval $[t_n, t_{n+1}]$ and evolve the system by the time step $\Delta t = t_{n+1} - t_n$,

$$|\psi, t_{n+1}\rangle = \mathbf{U}_n(t_{n+1}, t_n)\,|\psi, t_n\rangle. \tag{2.8}$$

Since we have access to the system state $|\psi, t_n\rangle$ at each time t_n we are able to evaluate various observables. Our canonical observable for the representation of the response curve is the time-averaged energy transfer. Therefore, the energy transfer

$$\Delta E(t_n) = \langle\psi, t_n|\mathbf{H}_0|\psi, t_n\rangle - E_0 \tag{2.9}$$

is evaluated at each time t_n of the modulation interval and eventually averaged over the saturated time range. For a strongly interacting system at $U_0/J_0 = 20$ the saturation sets in after $tJ_0 \approx 7$, which is discussed in Sect. 2.4.1.

This procedure is repeated for modulation frequencies in the range of interest which then provides a response function represented by the time-averaged energy transfer $\bar{\Delta E}$ as function of the modulation frequency ω.

2.1.4. Numerical methods

Crank-Nicholson (CN) scheme

For large-scale computations the construction of the time-evolution operators $\mathbf{U}_i$ would require to evaluate the exponential of the Hamiltonian (2.2) at each time step. This means numerically, that we have to evaluate the matrix exponential of the Hamilton matrix in the number-basis representation and, therefore, requires to transform it to its eigenbasis. Since the solution of the full eigenproblem is not feasible even for moderate system sizes, one has to approximate the time-evolution operator. We employ the well established Crank-Nicholson (CN) scheme (see appendix C for details)

$$U_n(t_{n+1}, t_n) \approx \frac{1 - \mathbf{i}H(t_{n+1/2})\Delta t/2}{1 + \mathbf{i}H(t_{n+1/2})\Delta t/2}. \tag{2.10}$$

The CN-scheme is of second order in time and since it is an implicit method, it is also unconditionally stable [54]. The price for this stability is that one has to solve a set of linear equations at each time step (see appendix C).

Predictor-Corrector (PC) method

Complementary to the CN scheme we also employ the predictor-corrector method, which is an explicit method for of ordinary differential equations. To explain the principle of the method we assume an initial state $\left|\psi, 0\right\rangle$ which has to be evolved by some Hamiltonian $\mathbf{H}(t)$ using the time-dependent Schrödinger equation. Initially, the method *predicts* the next time step $\left|\psi, n+1\right\rangle$ in an explicit Euler step. This rough guess is then used to interpolate the derivative in the *corrector*-step and eventually refine the solution [55]. Due to the predictor-step, the method does not require the solution of a set of linear equations and is, therefore, numerically less demanding than the CN scheme. On the other hand, the method lacks of the stability of the CN scheme, especially in cases where small numerical values are involved. The lack of accuracy of these values cumulates to larger numerical errors and eventually leads to a breakdown of the method. Since the initial states of a bosonic lattice in the strongly interacting regime include of a large number of extremely small coefficients in the number basis expansion, the method is problematic. However, in the weakly interacting regime, where almost all coefficients are small, but still accurate enough, the method performs well.

2.2. Linear Response Analysis

A valuable tool for studying the dynamical properties of a strongly interacting system of atoms in an optical lattice is the linear response analysis. The system is probed by a small amplitude modulation of the optical lattice (2.3). In order to investigate the effect of the temporal modulation, we focus on the time-dependent part of the lattice potential (2.3), which is responsible for the oscillation around the initial lattice depth V_0,

$$\begin{aligned} \tilde{V}_0(t) &= V_0[1 + F\sin(\omega t)] && (2.11) \\ &= V_0 + \Delta V_0(t), && (2.12) \end{aligned}$$

with $\Delta V_0(t) = V_0 F\sin(\omega t)$. The Hubbard parameters J and U are functions of the lattice depth V_0 and thus sensitive to its temporal variation. In a short notation the Hubbard Hamiltonian describing a homogeneous lattice system reads

$$\mathbf{H}(t) = -J[\tilde{V}_0(t)]\mathbf{H}_J + U[\tilde{V}_0(t)]\mathbf{H}_U \tag{2.13}$$

with the operator structure hidden in the symbols $\mathbf{H}_J$ and $\mathbf{H}_U$. Since we assume small modulations of the time-dependent lattice depth $V_0(t)$ around V_0 we can expand the Hamiltonian (2.13) and obtain a linearization by retaining the lowest-order terms only,

$$\mathbf{H}_{\text{lin}}(t) = \mathbf{H}_0 + \Delta V_0(t)\frac{\partial\mathbf{H}}{\partial\tilde{V}_0}\bigg|_{V_0}, \tag{2.14}$$

with the unperturbed Hamiltonian $\mathbf{H}_0$. Evaluation of the derivative in (2.14) with respect to the lattice depth $\tilde{V}_0$ (see Appendix A for detailed derivation) leads to the following expression:

$$\mathbf{H}_{\text{lin}}(t) = \mathbf{H}_0 + FV_0\sin(\omega t)\left[\frac{d\ln U}{d\tilde{V}_0}\bigg|_{V_0}\mathbf{H}_0 - J\left(\frac{d\ln J}{d\tilde{V}_0}\bigg|_{V_0} - \frac{d\ln U}{d\tilde{V}_0}\bigg|_{V_0}\right)\mathbf{H}_J\right]. \tag{2.15}$$

In order to understand the excitation of the ground state $|E_0\rangle$ we take a look at the operator structure of the linearized Hamiltonian (2.15) and how it is acting on $|E_0\rangle$. Whether the linearized, time-dependent Hamiltonian is capable to excite the ground state into a excited state $|E_\nu\rangle$ is determined by a non-vanishing matrix element $\langle E_\nu|\mathbf{H}_{\text{lin}}|E_0\rangle$. The first term of the time-dependent part of (2.15) is proportional to $\mathbf{H}_0$ and due to the orthogonality of the eigenstates, its contribution to the matrix element is trivially zero. But since $\mathbf{H}_J$ does not share its eigenbasis with $\mathbf{H}_0$, the third term can connect between the ground state and other eigenstates and can, therefore, produce excitations.

The matrix elements select those states from all eigenstates, which can be excited from the ground state via lattice modulation and are therefore the link to the excitation mechanism. This allows to define a simple strength function, which gives an estimate to the excitation spectrum of the system. The Gaussian based strength function (GSF) is given

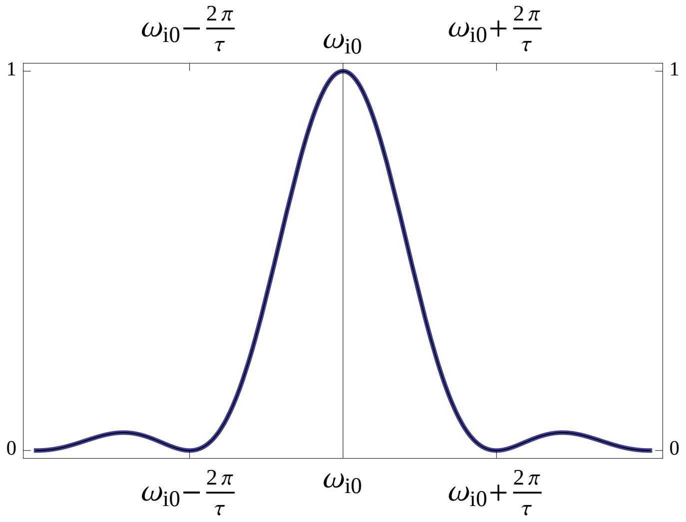

Fig. 2.1.: The sinc-function as the elementary response to periodic perturbations.

by

$$R_{\mathrm{GSF}}(\omega) = \sum_{\{\nu\}} E_\nu G_\sigma(\omega - E_\nu) \left|\left\langle E_\nu\right| \mathbf{H}_J \left|E_0\right\rangle\right|^2 , \tag{2.16}$$

with the modulation frequency ω and the energy eigenvalue E_ν of the eigenstate $\left|E_\nu\right\rangle$. The Gaussian function $G_\sigma(x)$ represents an elementary response of width σ. The width of the Gaussian is chosen for representation purposes and, in that sense, unrelated to the physics. Based on the linearized Hubbard Hamiltonian (2.15) one can also derive the proper expression for the transition probabilities based on time-dependent perturbation theory in the linear regime. The perturbative strength function (PSF) reads

$$R_{\mathrm{GSF}}(\omega) = \sum_{\nu} E_\nu P^{(\tau)}_{0\to\nu}(\omega), \tag{2.17}$$

with the transition probabilities

$$P^{(\tau)}_{0\to\nu}(\omega) = \left| J V_0 F \left(\left.\frac{d\ln J}{d\tilde{V}_0}\right|_{V_0} - \left.\frac{d\ln U}{d\tilde{V}_0}\right|_{V_0} \right) \left\langle E_\nu\right| \mathbf{H}_J \left|E_0\right\rangle \right|^2 \frac{\sin^2[(\omega_{i0} - \omega)\tau/2]}{(\omega_{i0} - \omega)^2}, \tag{2.18}$$

which are explicitly derived in Appendix B. For infinite modulation times $\tau \to \infty$ (2.17) leads to Fermi' s golden rule.

The transition probability consists of the matrix elements of the hopping operator between the ground and excited states and a pre-factor depending on the system parameters. The last part of the expression is a squared *sinc*-function, which represents a basic excitation depending on the modulation time τ.

In the simple form of the strength function (2.16) the Gaussian function took the role of the sinc-function, which is shown in Fig. 2.1, which demonstrates the reciprocal relation between modulation time and width of the resonance.

In the following we examine a system of $I = N = 6$ at several interaction strengths ranging from the Mott insulator to the superfluid regime. Figures 2.2 and 2.3 show in each column from top to bottom the energy spectrum, the Gaussian strength function (2.16), and the perturbative strength function (2.17). In the energy spectra in the top row non-vanishing matrix elements $\langle E_\nu | \mathbf{H}_J | E_0 \rangle$ are indicated by gray vertical lines. The Gaussian strength function in the second row and the perturbative strength function in the third row are based on the solution of the full eigenproblem of the underlying system.

In the case of the strongly interacting systems shown in Figs. 2.2 (a) and (b), there exist three strong excitation channels into the first band and a few into the third band. The matrix elements connecting the ground state and states in the second band are vanishing, since excitation of states in the second band are suppressed in homogeneous systems [28]. The strong matrix elements between ground state and first Hubbard band in Fig. 2.2 (a) generate the U-resonance and its fine structure in Fig. 2.2 (c) and (d). The matrix elements connecting ground state and the third band in Fig. 2.2 (a) are too weak to show up clearly in the response in Figs. 2.2 (c) and (e). The $3U$-resonance is visible in the response functions for $U/J = 15$ in Figs. 2.3 (d) and (f).

In the superfluid regime the energy gaps have vanished [Figs. 2.3 (a) and (b)] and a rather continuous distribution of states with non-vanishing transition amplitude appears. This results in broader strength distributions in Figs. 2.3 (c) and (d) (GSF) as well as (e) and (f) (PSF) [25,39].

In recent publications, the transition of the 3U-peak in Fig. 2.3 (j) to the frequency corresponding to 4U has been proposed as a signature of increasing superfluid character for a system with boxed boundary-conditions [24].

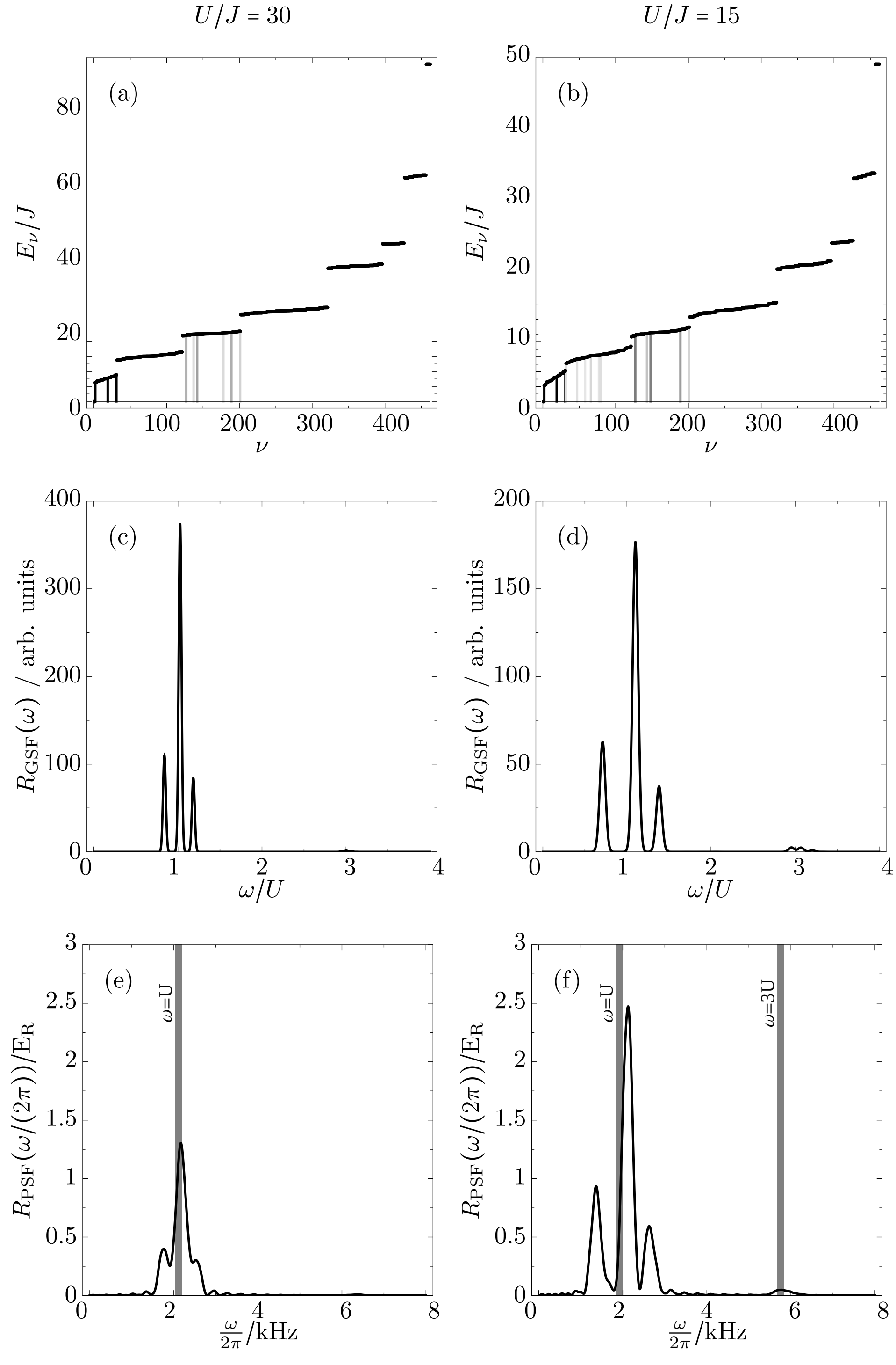

Fig. 2.2.: Eigenspectra (top row) and the strength functions (middle and bottom row) of 6 bosons on 6 sites of a homogeneous lattice for $U/J = 30, 15$ (from left to right). The vertical gray lines in the spectra point out eigenstates with sizable matrix element $\langle E_\nu | \mathbf{H}_J | E_0 \rangle$. Darker shadings refer to stronger matrix elements. Panels (c) and (d) show the gaussian strength function with the width $\sigma/J = 0.5$. Panels (e) and (f) show the response based on the perturbative strength function with $\tau = 20$ ms. The vertical gray lines in (e) and (f) point-out the modulation frequencies corresponding to $\omega = U$, $3U$.

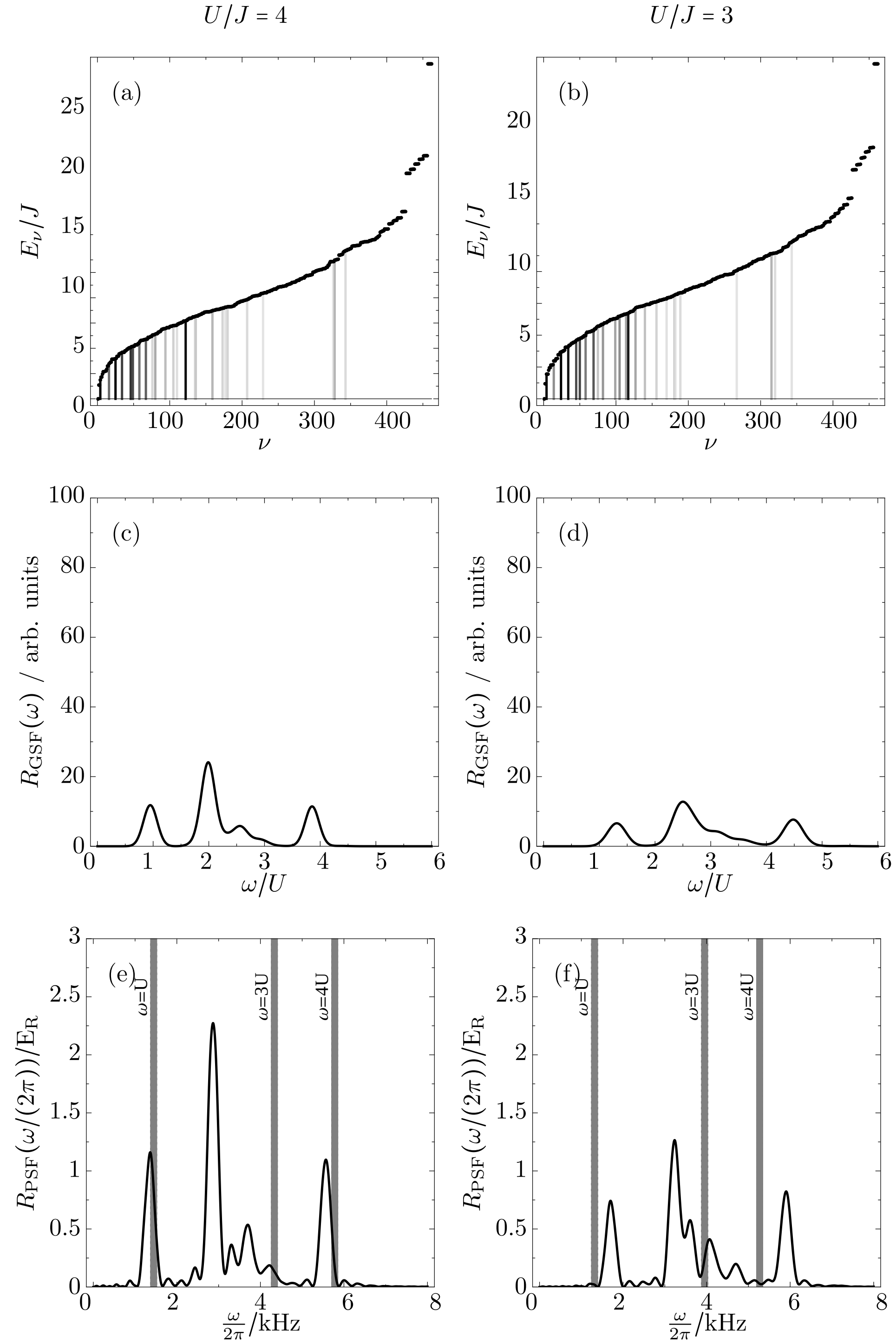

Fig. 2.3.: Eigenspectra (top row) and the strength functions (middle and bottom row) of 6 bosons on 6 sites of a homogeneous lattice for $U/J = 4, 3$ (from left to right). The vertical gray lines in the spectra point out eigenstates with sizable matrix element $\langle E_\nu | \mathbf{H}_J | E_0 \rangle$. Darker shadings refer to stronger matrix elements. Panels (c) and (d) show the gaussian strength function with the width $\sigma/J = 0.5$. Panels (e) and (f) show the response based on the perturbative strength function with $\tau = 20$ ms. The vertical gray lines in (e) and (f) point-out the modulation frequencies corresponding to $\omega = U$, $3U$, $4U$.

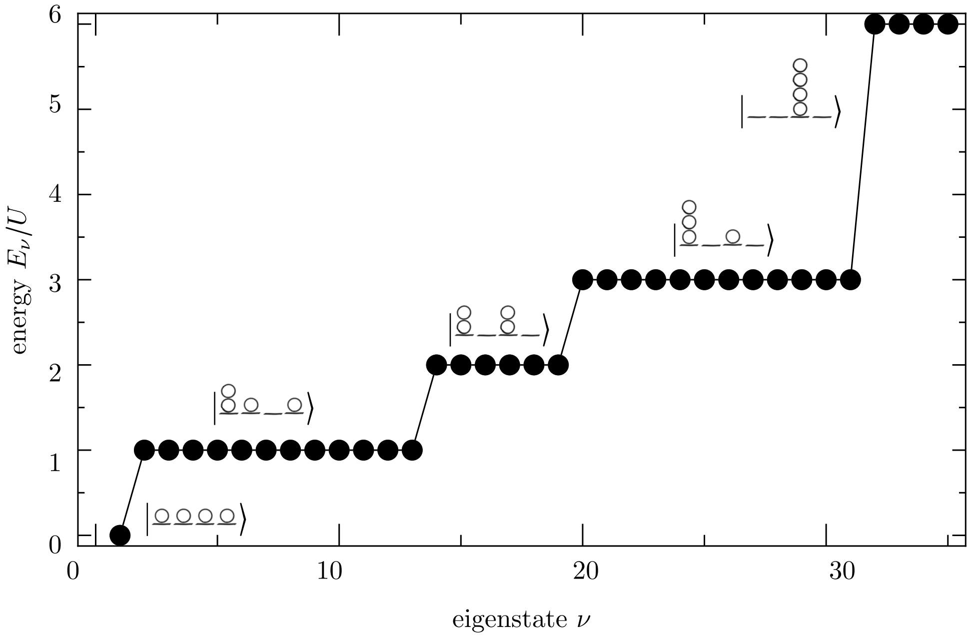

Fig. 2.4.: Energy spectrum of system of 4 bosons on 4 sites at $U/J \to \infty$. The drawings on top of the bands represent the structure of the eigenstates in the band, and each eigenstate is a permutation of this drawing. The ground state, which is located in the lower left corner at $E_0 = 0$ is $\left|1,1,1,1\right\rangle$.

2.3. Importance truncation

2.3.1. Energy based truncation

Up to now, we have studied systems in the full single-band Hilbert space. The dimension of the Hilbert space for N bosons on I sites is given by

$$D = \frac{(N+I-1)!}{N!(I-1)!}.$$

Due to this factorial growth of the basis with the number of bosons and sites (see Fig. 1.2), it is not feasible to treat systems in the full Hilbert space for experimentally relevant system sizes. The straight-forward way to reduce the numerical effort is to restrict the calculations on the relevant subspace, i.e., to keep the most important number states only.

A measure for the importance of a number state $\left|m\right\rangle$ for the description of a particular energy eigenstate $\left|E_\nu\right\rangle$ is its amplitude $c_m^{(\nu)} = \left\langle m\middle|E_\nu\right\rangle$. The larger the magnitude of the coefficient $|c_m^{(\nu)}|$, the more important the corresponding number state $\left|m\right\rangle$. The difficulty of this measure is, that the coefficients are not known *a priori*, since they require the solution the Schrödinger equation at first. Hence, in order to truncate the system in an effective manner, we have to find another measure which is available without solving the eigenproblem.

To find such a measure, we analyze the system we want to investigate. Our aim is to describe the low-energy properties and eventually the low-lying excitations of a bosonic lattice system in the strongly interacting regime. This means in the language of the Bose-Hubbard model, that the tunneling strength J is small compared to the interaction U. Since the only off-diagonal elements are proportional to the small parameter J and the interaction term is purely diagonal in number basis representation, the Hamilton matrix is close to diagonal.

We go one step further and assume the tunneling strength to be $J = 0$, and consequently $U/J \to \infty$. Figure 2.4 illustrates the energy spectrum for 4 bosons on 4 sites for such an infinite interaction.

Since the Hamilton matrix is diagonal in the number basis representation, the number states are the energy eigenstates of the system. Each of the fully degenerate Hubbard bands in Fig. 2.4 consists of a certain class of number states of the same energy. The ground state is the number state with all four bosons on individual sites and the energy $\big\langle \underline{\circ}\,\underline{\circ}\,\underline{\circ}\,\underline{\circ} \big| \mathbf{H} \big| \underline{\circ}\,\underline{\circ}\,\underline{\circ}\,\underline{\circ} \big\rangle = 0$.

The next higher energy in the spectrum comes from eigenstates with one doubly occupied and one unoccupied site, i.e.

$$\big\langle \underline{\circ}\,\underline{\ \ }\,\underline{\circ}\,\underline{\overset{\circ}{\circ}} \big| \mathbf{H} \big| \underline{\circ}\,\underline{\ \ }\,\underline{\circ}\,\underline{\overset{\circ}{\circ}} \big\rangle = U, \tag{2.19}$$

and forms the first Hubbard band. With a simple combinatorial argument we can evaluate the number of states in the first band: For a system of I sites there are I options to place the double occupation times $I - 1$ remaining options to put the unoccupied site, which makes 12 states for $I = 4$.

The next band is composed by number states with two double occupations and lies at the energy $2U$. This scheme can be continued for all energies of the eigenstates; exemplarily, the typical number states are shown on top of each band in Fig. 2.4 (b).

If we now allow weak tunneling $J \ll U$ between the lattice sites, weak off-diagonal elements appear in the Hamilton matrix. This means for the eigenstates that correlations to other number states arise and, therefore, their degeneracy is broken (cf. the sequence of Figs. 1.3). Nevertheless, the major contribution to the eigenstates in the individual bands still comes from the number states we identified in the system with $U/J \to \infty$.

The knowledge of the number states which contribute the strongest to the low-lying

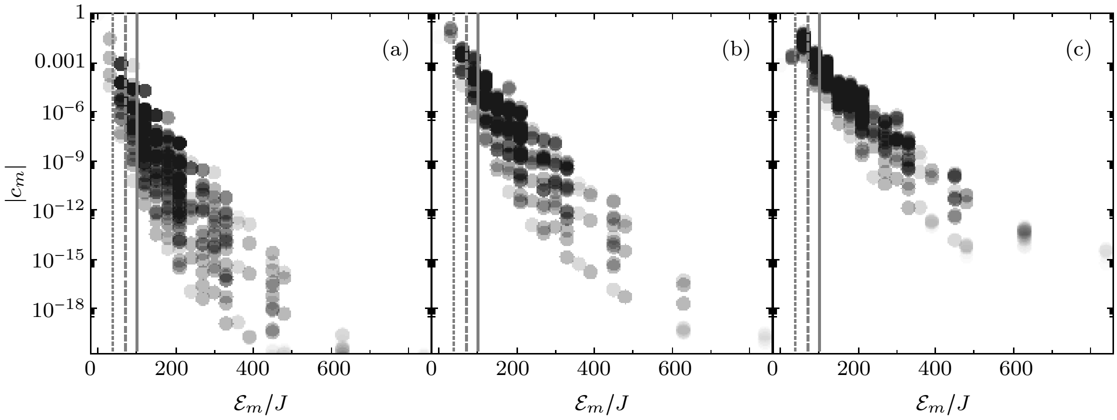

Fig. 2.5.: Correlation between the *a posteriori* coefficients c_i of the eigenstates and the *a priori* energy of the respective numberstate $|m\rangle$ for 8 bosons on 8 sites at the $U/J = 30$. The panels show the ground state (a), the first states of the first (b) and second (c) Hubbard band. The vertical gray lines point out typical cut-off energies $\mathcal{E}_{\text{trunc}}/J = 40$ (┈┈┈), 70 (— — —), 100 (———), which define truncated bases of the dimensions $D = 57, 477, 1205$.

eigenstates together with the fact that these number states are those with lowest energy $\mathcal{E}_m = \langle m|\mathbf{H}|m\rangle$ offers a handle to introduce an energy-based truncation criterion. One can simply restrict the model space to the number states $|m\rangle$ which fulfill the inequality

$$\mathcal{E}_m = \langle m|\mathbf{H}|m\rangle \leq \mathcal{E}_{\text{trunc}}, \tag{2.20}$$

i.e., to allow for states with an energy below the truncation energy $\mathcal{E}_{\text{trunc}}$, only. Moreover, since the energy $\mathcal{E}_m$ can be easily evaluated it is available a priori.

Correlation between energy and coefficient of a number state

As a benchmark for this criterion, we plot the energy $\mathcal{E}_m$ versus their coefficient of some eigenstates of an exactly solvable system with 8 bosons on 8 sites at $U/J = 30$. Figure 2.5 illustrates that for the ground state (a), and the first states of the first (b) and second (c) Hubbard band. The plots confirm that the energy $\mathcal{E}_m$ gives a reliable *a priori* estimate of the *a posteriori* coefficients.

The plots demonstrate also the tendency, that for higher-lying eigenstates more number states get important, since the centroid of the coefficients increases in (b) and (c). The three vertical lines mark typical truncation energies $\mathcal{E}_{\text{trunc}}/J_0 = 40, 70, 100$ which correspond to the basis dimensions $D = 57, 477, 1205$. This is important, since we want to investigate excitations from the ground state to states in the first few bands. Hence, we have to choose the truncation energy appropriate to include also the number states that are important for these bands. We will address this in the following benchmark section.

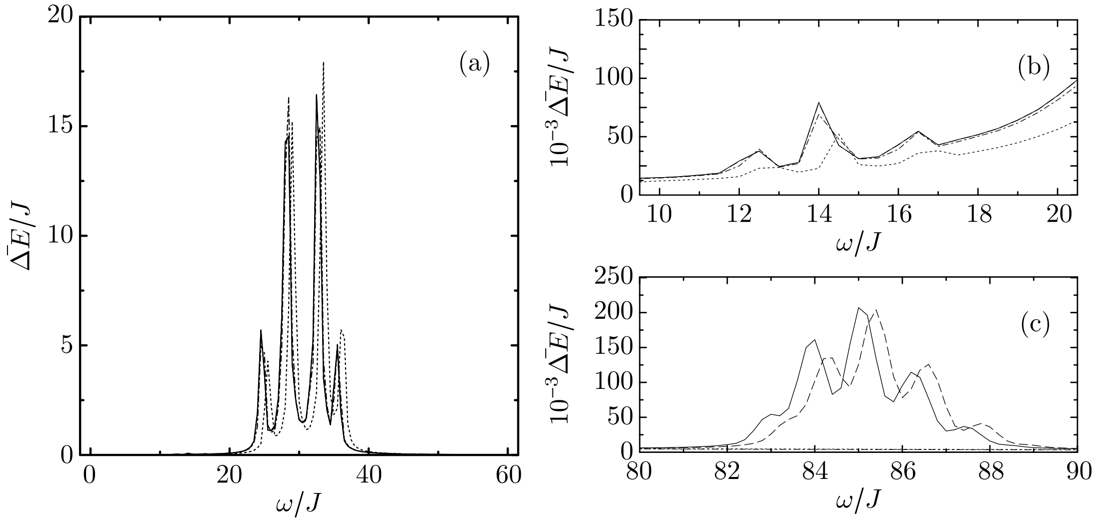

Fig. 2.6.: Comparison of the time-averaged energy transfer $\bar{\Delta E}$ for a Bose gas with $I = N = 8$ at the interaction strength $U/J = 30$. The solid line (———) represents the results for the full basis, (— — —) shows the time evolution for the truncation $\mathcal{E}_{\text{trunc}}/J = 100$, (-—-—-) for $\mathcal{E}_{\text{trunc}}/J = 70$, and (-------) for $\mathcal{E}_{\text{trunc}}/J = 40$. Depicted are the main resonance at $\omega = U$ (a), the non-linear resonance at $\omega = U/2$ (b), and the $3U$-resonance (c).

In conclusion, we have seen, that the energy based truncation provides an efficient means to discard irrelevant number states from the outset, based on the clear correlation between the expansion coefficients $c_m^{(\nu)}$ and the energy $\mathcal{E}_m$. Moreover, the importance truncation preserves properties like the variational principle as well as the Hylleraas-Undheim theorem. This ensures the eigenenergies obtained in the importance truncated space are always upper bounds to the exact energies in the full space.

2.3.2. Exact time evolution: benchmark calculations

In order to demonstrate the robustness of the importance truncation for the description of the time evolution under small amplitude modulations of the optical lattice, we perform benchmark calculations with several truncation energies and compare the results with the full basis for a system of 8 bosons in 8 sites at $U/J = 30$.

We perform explicit time-evolutions of the system for the full basis as well as three truncated bases with $\mathcal{E}_{\text{trunc}}/J = 100, 70, 40$. As observable we evaluate the energy transfer into the system via

$$\Delta E(t) = \langle \psi, t | \mathbf{H}_0 | \psi, t \rangle - E_0 \tag{2.21}$$

with the initial Hamiltonian $\mathbf{H}_0 = \mathbf{H}(t = 0)$ and the energy of the initial state E_0. The energy transfer is averaged over the modulation time, where we leave out the initial phase of the system to cover only the saturated time-range $\tau J_0 = 6 - 20$. This procedure is repeated for modulation frequencies in the range of $\omega/J_0 = 0 - 70$ in order to obtain the response function $\bar{\Delta E}$ as function of ω.

Figure 2.6 (a) shows the typical U-resonance located at $\omega = U$ with the fragmentation resulting from the finite size of the system. This resonance is based on excitations from the ground state to states in the first Hubbard band. Fig. 2.6 (b) shows a small resonance at $\omega = U/2$ which results from a non-linear effect based on the excitation into a first-band state of the energy $U/2$ [28] . Fig. 2.6 (c) shows the 3U resonance at $\omega = 3U$ which corresponds to excitations from the ground state into the third Hubbard band.

The U-resonance and the resonance at $\omega = U/2$ are very well described with all of the bases, solely the strongest truncation with $\mathcal{E}_{\text{trunc}}/J = 40$ shows a small shift to higher energies. This shift is an effect of the strong truncation and manifests its variational character [56, 57]. However, the $3U$-resonance is not visible for the bases truncated at $\mathcal{E}_{\text{trunc}}/J = 70$ and 40, since the relevant number states describing the states of the third band are not included.

Overall, the resonances which lie close to the truncation energy tend to be shifted to higher modulation frequencies. In the sense of the variational principle, this means that these states miss some correlations to higher number states, which are not included. Besides the U-resonance for the basis with $\mathcal{E}_{\text{trunc}}/J = 40$ one observes this also for the $3U$-resonance with the basis with $\mathcal{E}_{\text{trunc}}/J = 100$. Nevertheless, these resonances allow still for qualitative discussions.

To sum up, the importance truncation allows to reduce the numerical effort in a controlled way. By choosing the truncation energy appropriate one can include certain features like higher resonances in calculations with a larger model space as well as focus on the U-resonance only with a stronger truncation.

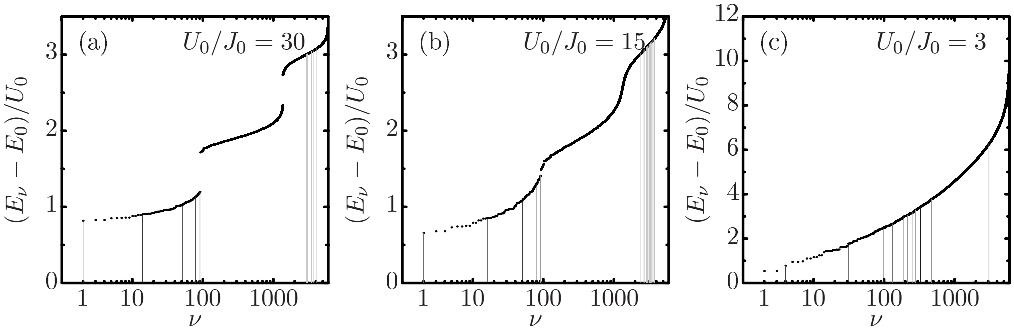

Fig. 2.7.: Lowest energy eigenvalues of 10 bosons on 10 sites at the interaction strengths $U/J = 30, 15, 3$, computed by diagonalization of the Hamilton matrix in a truncated number basis. The basis used in all three cases is generated for the interaction strength $U/J = 30$ and includes number states up to the energy $\mathcal{E}_{\text{trunc}}/J_0 = 100$. The energies are shifted by the ground state energy. The vertical lines illustrate the strongest matrix elements $\langle E_\nu | \mathbf{H}_J | E_0 \rangle$, which connect the ground state to excited states. The strength of the matrix elements is represented by the gray level of the lines, where darker lines correspond to stronger values.

2.4. Homogeneous systems

In this section, the signatures of the response function in the Mott insulating regime and towards the superfluid phase are studied. Therefore, we simulate 10 bosons on 10 sites of a homogeneous lattice at several interaction strengths in the strongly interacting and superfluid regime using the linear response analysis and explicit time-evolutions.

2.4.1. Linear response analysis & time evolution in truncated bases

We have seen in Sect. 2.2 that the linear response analysis is a valuable tool to identify possible excitations in the strongly interacting regime. Therefore, we solve the stationary Schrödinger equation of a system of 10 bosons on 10 sites in a basis truncated with $\mathcal{E}_{\text{trunc}}/J_0 = 100$ at $U_0/J_0 = 30$, i.e., the number states dominating the third Hubbard band are included. This basis is used for the solution of two systems in the Mott regime with the interaction strengths $U_0/J_0 = 30$ and 15 as well as one system in the superfluid phase $U_0/J_0 = 3$.

Figure 2.7 (a) shows the energy spectrum for the system with $U_0/J_0 = 30$. The vertical gray lines mark strong matrix elements $\langle E_\nu | \mathbf{H}_J | E_0 \rangle$ of the tunneling operator between ground and excited states. These matrix elements identify five prominent states in the first Hubbard band, which indicate possible excitations created by the lattice modulation. Moreover, one observes a few weaker matrix elements which indicate excitations into the third band.

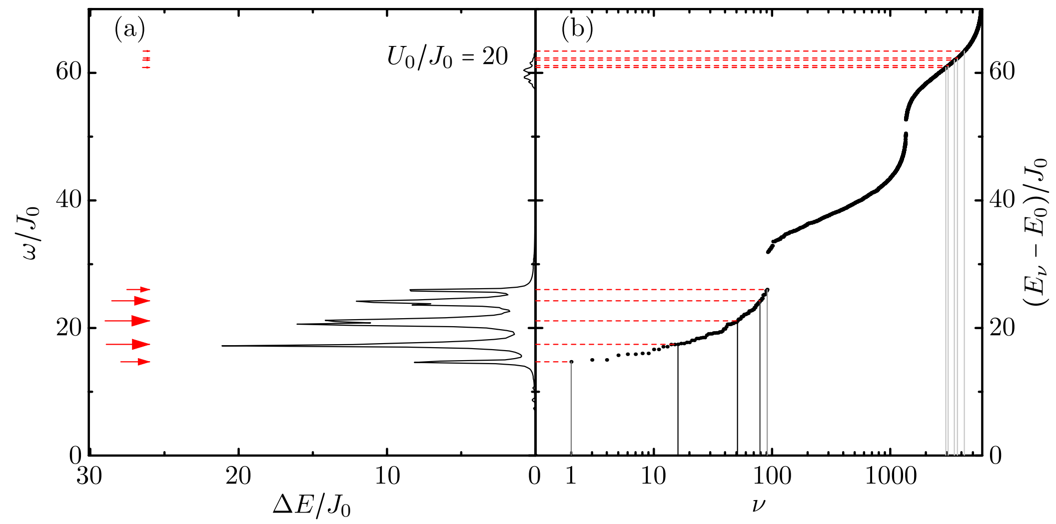

Fig. 2.8.: Relation between the excitation energies of the static Hubbard Hamiltonian and the resonance structure of a bosonic system ($I = N = 10$) at $U_0/J_0 = 20$. The left panel shows the time-averaged energy transfer as a function of the frequency ω; the right panel depicts the lower part of the energy spectrum of the corresponding Hamiltonian. The vertical gray lines mark the eigenstates which are connected to the ground state by strong matrix elements $\langle E_\nu | \mathbf{H}_J | E_0 \rangle$. the horizontal lines and the arrows respectively point out the correspondence between the excitation energies and the resonance structure.

For $U_0/J_0 = 15$ in Fig. 2.7 (b) the gaps between the Hubbard bands are strongly reduced. On the other hand, the width of the bands has increased in comparison to the higher interacting case. The excitations to the first and third band marked by the vertical gray lines, thus are spread over a wider energy range and therefore yield a broadened excitation profile.

For the superfluid case with $U_0/J_0 = 3$ in Fig. 2.7 (c) the band gaps have eventually vanished and the strong matrix elements connecting ground and excited states are spread over a wider range. This leads to a more continuous excitation function in contrast to the strongly interacting systems discussed before.

Linear response analysis & explicit time-evolution

The linear response analysis provides already a rough picture of the response function one has to expect for systems in different regions of the phase diagram. For the strongly interacting regime the importance truncated solutions predict a strong resonance for modulation frequencies in the energy region of the first band $\omega \approx U_0$ and a weaker one at $\omega \approx 3U_0$.

In Fig. 2.8 we compare the response function for a system of 10 bosons on 10 sites at

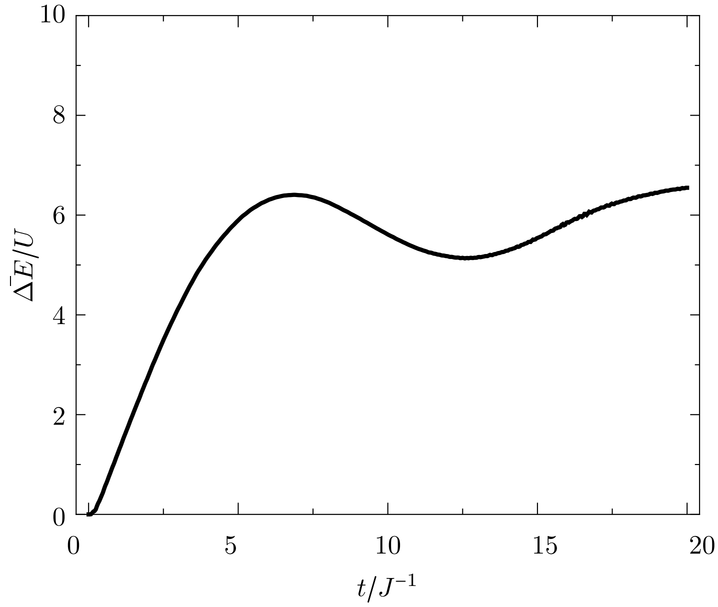

Fig. 2.9.: Frequency-averaged energy transfer $\Delta\bar{E}$ as function of the time of a system with $I = N = 10$ at $U_0/J_0 = 20$ and a truncation energy $\mathcal{E}_{\text{trunc}}/J_0 = 120$. The plot shows the average energy transfer in the interval $\omega/J = 14.4$ to 25.6 (U-resonance) at each time.

$U_0/J_0 = 20$ with the lower end of the energy spectrum of the static Hamiltonian. The response curve is obtained via an explicit time-evolution in the truncated basis with $\mathcal{E}_{\text{trunc}}/J_0 = 70$ and the evaluation of the energy transfer ΔE into the system. Figure 2.8 (a) shows the energy transfer averaged over the modulation time versus the modulation frequency ω of the lattice amplitude. Figure 2.8 (b) shows the energy spectrum in which the vertical lines point out the excitations predicted by the linear response analysis. The horizontal lines are just guides to the eye and confirm, that the excited states identified by the linear response analysis are indeed responsible for the fine-structure of the response function.

The energy transfer in Fig. 2.8 (a) also shows the barely visible resonance at $\omega = U_0/2$. Since this excitation is based on non-linear effects as mentioned earlier, it is not covered by the linear response analysis and therefore not observed in the spectrum in (b).

Saturation of the energy transfer

In the following, we examine the saturation behavior of a system with $I = N = 10$ at $U_0/J_0 = 20$. The number basis of the system is truncated with $\mathcal{E}_{\text{trunc}}/J_0 = 120$. Figure 2.9 illustrates the energy transfer averaged over the frequency interval $\omega/J_0 = 14.4$ to 25.6 (U-resonance) as function of time. The simulation starts with the ground state of the static Hamiltonian as initial state. The system shows transition phase in the time $tJ_0 = 0$ to 7 after which the energy transfer is saturated with a small temporal modulations. In

schematic	type	energy transfer
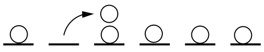	one-particle-one-hole (1p1h)	U_0
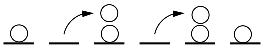	two-particle-two-hole (2p2h)	$2U_0$
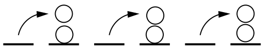	three-particle-three-hole (3p3h)	$3U_0$
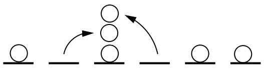	2p2h with two particles at same site	$3U_0$

Tab. 2.1.: Basic types of particle-hole excitations of first order, sorted by energy transfer.

the following simulations, we show resonance function represented by the time-averaged energy transfer as function of the modulation frequency. For the time averaging, we omit this transition phase and include the values in the saturated phase only.

2.4.2. Explicit time-evolution

In the following we analyze dynamic simulations for systems of 10 bosons on 10 sites of an optical lattice with interaction strengths ranging from $U_0/J_0 = 30$ in the Mott insulating regime to $U_0/J_0 = 3$ in the superfluid regime. All of the explicit time-evolutions have been performed with identical importance truncated bases with $\mathcal{E}_{\text{trunc}}/J_0 = 100$ constructed for $U_0/J_0 = 30$.

In order to integrate the time-dependent Schrödinger equation we employ the Crank-Nicholson (CN) scheme for the systems in the Mott-insulating regime. Although the predictor-corrector (PC) method is faster, it is not applicable for strong interactions, due to the structure of the states. The initial state (ground state) consists of a large number of extremely small expansion coefficients $c_m^{(0)}$ with large relative uncertainties, which result in the cumulation of the numerical errors and eventually in the break down. In the superfluid regime, however, the coefficients $c_m^{(0)}$ of the initial state are of sufficient magnitude that we can employ the PC method.

Each panel in Figs. 2.10 (a) to (f) shows the full time-resolved energy transfer in a density plot with the corresponding time-averaged values on top. The arrows in the plots of the time-averaged energy-transfer point to the modulation frequencies identified by linear response analysis.

Deep in the strongly interacting regime [Fig. 2.10 (a) and (b)] the strong U resonance in the region of the first Hubbard band $\omega \sim U$ is observed. The much weaker 3U res-

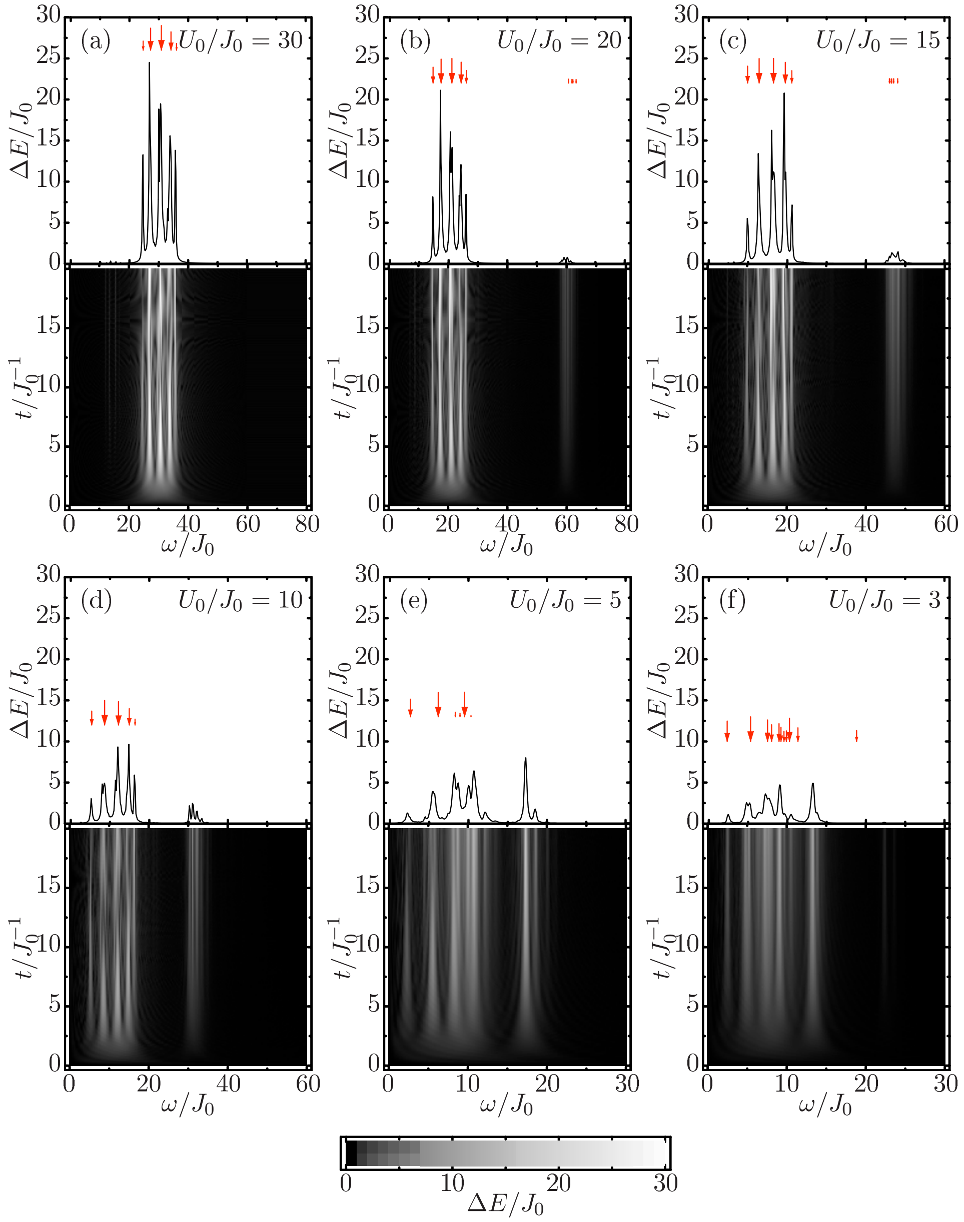

Fig. 2.10.: Energy transfer of 10 bosons on 10 lattice sites by frequency modulation at different interaction strengths due to the oscillation of the lattice amplitude. The density plots show the energy transfer over time and oscillation frequency; the relative modulation amplitude is $F = 0.1$. The plots on top show the energy transfer averaged over the full time. The sequence from (a) to (f) shows the results for the interaction to tunneling strength- ratios $U_0/J_0 = 30, 20, 15, 10, 5, 3$. The arrows in (a), (d), and (e) point out the excitation energies of eigenstates $|E_\nu\rangle$ which are connected to the ground state by the hopping operator $\mathbf{H}_J$. The time evolutions (a) and (b) are made using the Crank-Nicholson scheme, (c) to (f) by a 5th order predictor-corrector method.

onance appears at $\omega \sim 3U$, which corresponds to the excitations from the ground state to states in the third band. The strength of the 3U-resonance is increasing towards the superfluid regime [Fig. 2.10 (a) to (d)], which can be understood in a simple picture:

Since the resonance is based on excitations into states of the third band, whose composition is dominated by 3p3h-excited number-states $|3p3h\rangle$ (cf. Tab. 2.1 for the classification of the particle-hole excitations). Therefore, strong matrix elements $\langle 3p3h|\mathbf{H}_J|0\rangle$ require a certain contribution of 2p2h number-states in the ground state, since those are the only states directly connected to the 3p3h states via the hopping operator. Since the multiple occupations are unfavored in the ground state for stronger interactions, the coefficients of the 2p2h states are smaller and consequently the matrix elements into the third band are weaker, too.

Besides the U- and $3U$-resonance there appears also the even weaker U/2-resonance. This resonance can be explained by particle-hole excitations, i.e., putting one particle onto another on a different site, by two quanta of the energy $\omega = U/2$ [28].

As expected, the sequence from Fig. 2.10 (a) to (f) shows a successive broadening of the response function from the strongly interacting regime towards the superfluid phase. The former 3U-resonance is shifted towards higher energies [Fig. 2.10 (d) to (f)], which has also been observed in density-matrix RG (DMRG) studies for systems with boxed boundary conditions [24]. In this publication [24], the shift of the 3U resonance to the energy 4U in the superfluid regime is interpreted as a signature of a emerging superfluid character for systems with boxed boundary conditions. In contrast, we observe a further shift beyond 4U for even weaker interactions [Fig. 2.10 (f)] for periodic boundary conditions.

In summary, the estimates obtained with the linear response analysis are confirmed by the explicit time-evolution: One observes strong and discrete excitations in the strongly interacting regime which are a signature of the gapped energy spectrum. The decrease of the interaction strength results in a significant broadening of the resonances which corresponds to the increase of the widths of the Hubbard bands.

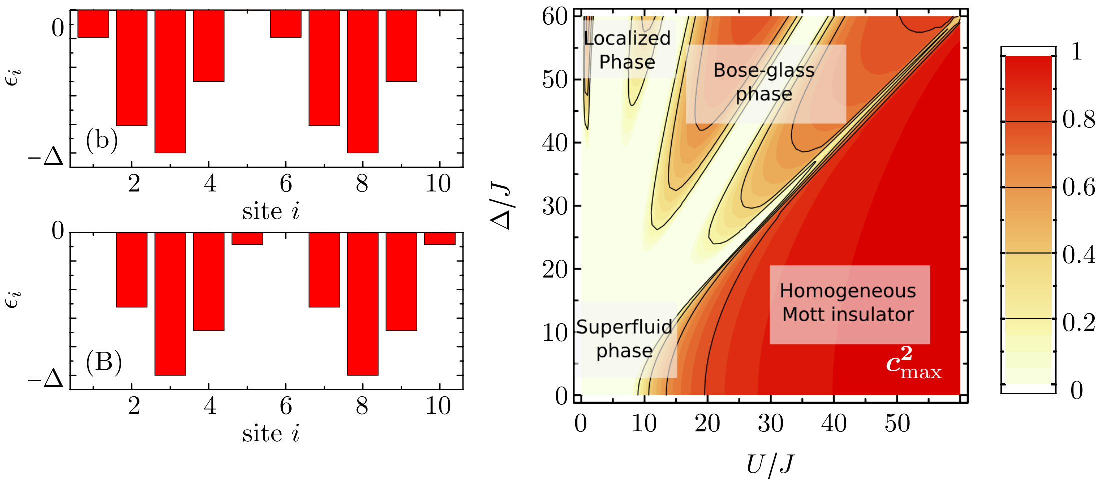

Fig. 2.11.: Left panels: two different sets of on-site energies ϵ_i of period-five two-color superlattices used in this section. Right panel: phase diagram of bosons in an optical superlattice (I=N=10) spanned by the interaction strength U/J and the superlattice amplitude Δ/J for the set (A) of on-site energies. Depicted is the maximum coefficient c^2_{max} of the number state expansion of the ground state.

2.5. Disordered systems

In this section we investigate the dynamics of a strongly interacting system in the presence of a disordering lattice component. The disorder is realized by a two-color superlattice potential, which we introduced in Sect. 1.3.3. The superlattice potential is realized in the following simulations by two sets of on-site energies ϵ_i as depicted in the left-hand panel of Fig. 2.11. The wave lengths of the superposed waves are identical in the sets (A) and (B), but the relative phases differs, which results in small deviations in the on-site energies. This allows to estimate the dependence of the response on the detailed topology of the superlattice.

The right-hand panel of Fig. 2.11 illustrates the phase-diagram of a system with the two-color superlattice (A) which we discussed in detail in Sect. 1.3.3. In the following, we focus on the strongly interacting regime and investigate the effect of an emerging superlattice amplitude Δ on the response structure. Therefore, we employ the linear response analysis and also fully dynamical calculations. In the final part of this section we investigate the quasi-momentum distribution of the U-resonance in combination with the superlattice.

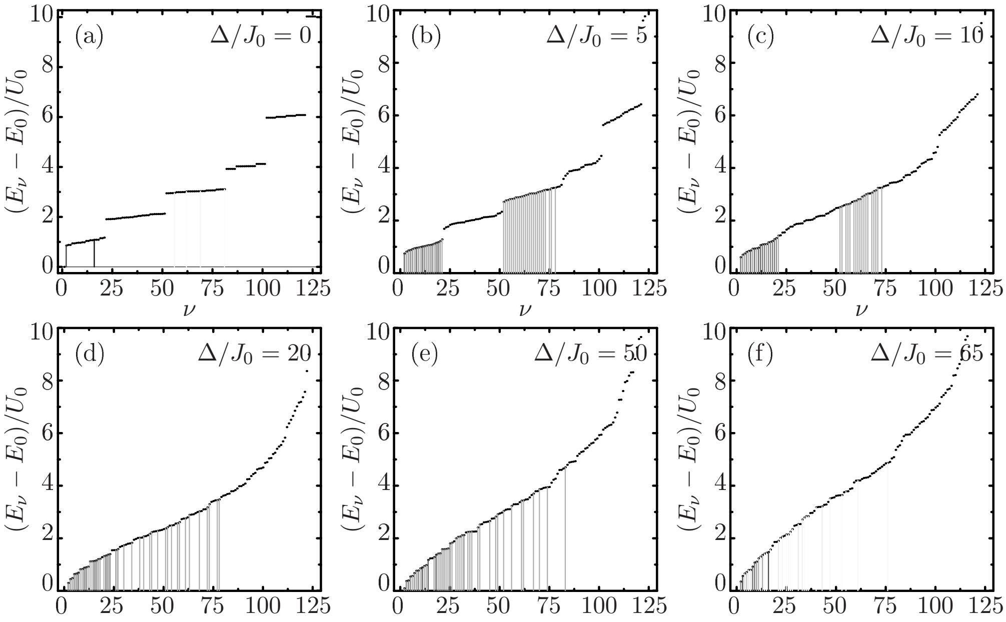

Fig. 2.12.: Depicted are the energy eigenvalues of 5 bosons on 5 sites at the fixed interaction strength $U_0/J_0 = 30$ and various superlattice amplitudes Δ/J_0. Note that the groundstate energy is shifted to zero. The vertical lines point out the eigenstates which are connected to the groundstate via the hopping operator $\mathbf{H}_J$.

2.5.1. Linear response analysis

In the following, we investigate systems of filling factor $N/I = 1$ at fixed interaction strength $U_0/J_0 = 30$ and various superlattice amplitudes. At first we look at the energy spectrum of a system of 5 sites and identify possible excitations by employing the linear response analysis. We have chosen a system consisting of the first five sites of superlattice (A) in Fig. 2.11 to be able to solve the complete eigenvalue problem.

Figure 2.12 illustrates the energy spectra in a sequence ranging from the pure Mott insulator case with $\Delta = 0$ (a) into the quasi Bose-glass phase (f). The vertical gray lines are the strongest matrix elements of the tunneling operator $\mathbf{H}_J$ between the ground state and the excited state $|E_\nu\rangle$.

For the pure Mott case in Fig. 2.12 (a) we observe the characteristic gapped spectrum and two strong matrix elements connecting the ground state to states in the first Hubbard band. These matrix elements suggest a two-peak fine-structure of the U resonance. Furthermore, one can observe a few very weak matrix elements of the ground state and state of the third band.

Already the small variation of the on-site energies at $\Delta/J_0 = 5$ in Fig. 2.12 (b) weakens the gapped structure of the spectrum and results in extended bands of sizable matrix elements from the ground state to states in the first and third Hubbard band.

For $\Delta/J_0 = 10$ in Fig. 2.12 (c) the gaps are not visible anymore from the spectrum itself. Their position can be guessed by the excitation energies indicated by the vertical lines. For $\Delta/J_0 = 20$ in Fig. 2.12 (d) the possible excitation energies are rather continuously distributed over a wider energy range from close to $E = 0$ up to $\sim 3.5 J_0$.

Inside the quasi Bose-glass phase in Fig. 2.12 (e) at $\Delta/J_0 = 50$, the excitation energies range down to $E = 0$, which suggests the emergence of low-lying strength. These low-lying excitations indicate the Bose-glass phase, but they are also a signature of the superfluid phase (cf. Sect. 2.4). For even stronger superlattice amplitudes $\Delta/J_0 = 65$ in Fig. 2.12 (f) the matrix elements at higher excitation energies are severely weakened and only the low-lying strength remain.

In conclusion, the inclusion of a superlattice potential results in a reduction of the energy gaps of the spectrum and spreading of the non-vanishing matrix elements over a wider energy range leading to a broadening of the resonances. In the quasi Bose-glass phase we observe low-lying strengths.

2.5.2. Explicit time-evolution

We now turn to fully dynamical simulations of Bose gases in time-dependent superlattices. We focus on a system of $N = 10$ bosons in the two-cell superlattices with $I = 10$ sites as defined by (A) and (B) in Fig. 2.12. All simulations are performed for a fixed interaction strength $U_0/J_0 = 30$ and various values for the superlattice amplitude Δ/J_0. As initial state we use the ground state of the static Bose-Hubbard Hamiltonian for the same parameters. In analogy to the procedure for regular potentials in Sect. 2.4 the lattice potential is modulated in time with a frequency ω and a fixed relative amplitude $F = 0.1$. All simulations shown Fig. 2.13 are performed with both of the two on-site energy distributions depicted in Fig. 2.12 in order to assess the impact of the specific distribution of the on-site energies $\Delta\epsilon_i$. The density plots in the lower part of each panel show the energy transfer as function of time and frequency for superlattice (A). The plots in the upper part represent the time-averaged energy transfer as function of the frequency for both superlattice topologies. The arrows above the individual peaks mark the excitation energies associated with the strongest matrix elements $\langle E_\nu | \mathbf{H}_J | E_0 \rangle$. The length of the arrows indicates the relative strength of the matrix elements.

Figure 2.13 (a) depicts the U resonance in the case of a regular lattice, i.e., for vanishing superlattice amplitude Δ/J_0. As for the homogeneous lattice discussed before, the excitation energies associated with the strongest matrix elements resulting from the linear response analysis nicely describe the position and fine-structure of the resonance. If we increase the superlattice amplitude to the value $\Delta/J_0 = 20$ — still remaining in

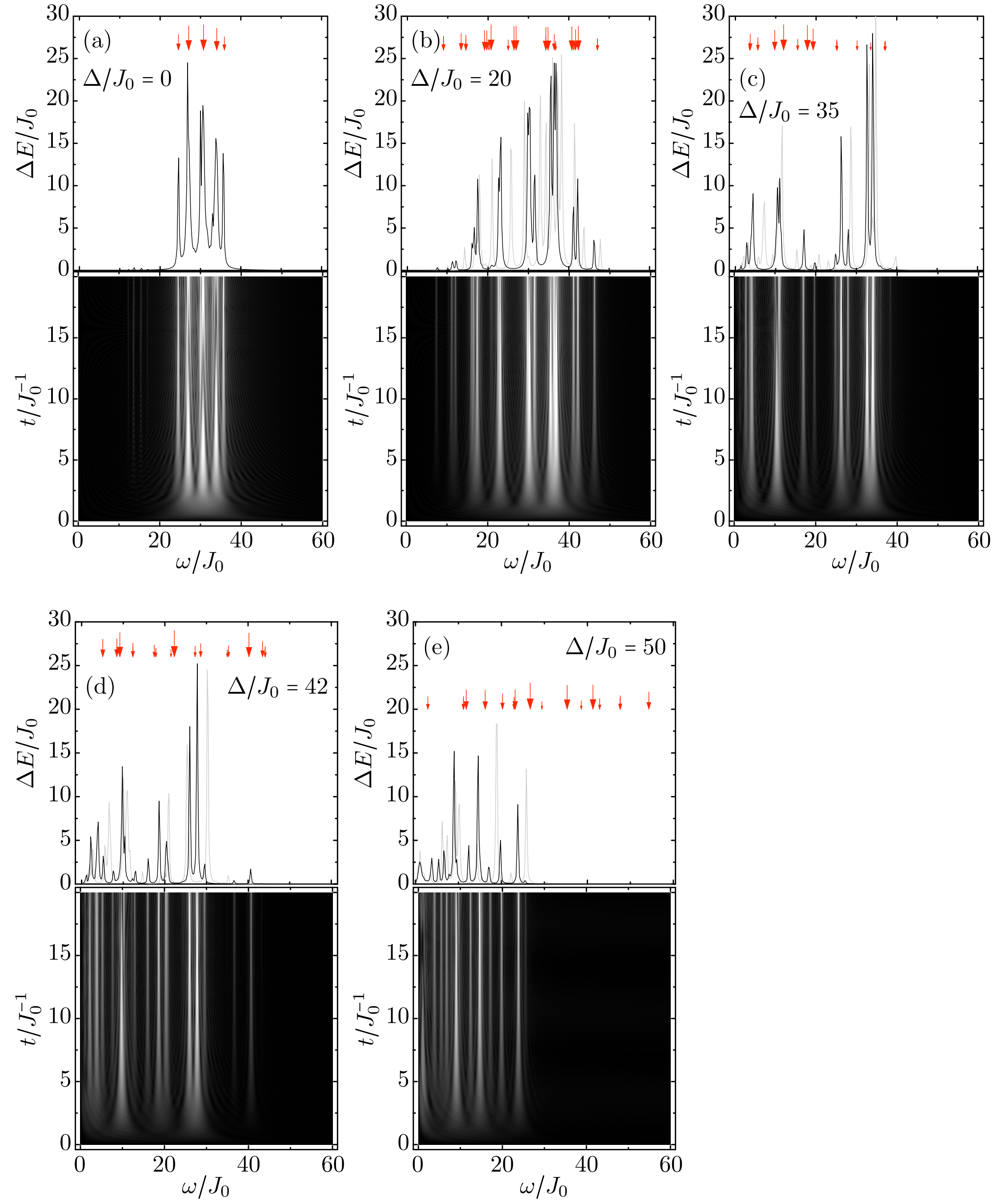

Fig. 2.13.: Bosonic system of 10 atoms on 10 sites at interaction strength $U_0/J_0 = 30$ for two superlattice amplitudes Δ/J_0 in the homogenous Mott phase. Depicted is the energy transfer due to a lattice modulation with the frequency ω and the relative amplitude $F = 0.1$. The black line (——) shows the results for superlattice (A), the gray line (——) for (B). The arrows point-out the excitation energies predicted by the linear response analysis. The density plots illustrate the energy transfer as a function of time and frequency for the superlattice (A).

the homogeneous Mott-insulator phase — the overall width of the resonance structure increases. The characteristic scale of the fine structure increases as well, and additional peaks emerge. This is in agreement with the results of the linear response analysis discussed previously.

An increase of the superlattice amplitude leads to a broadening of the Hubbard bands (see Fig. 2.12 (b)) which corresponds to the broadening of the resonance. This effect has also been observed in the experiment by Fallani [36]. The larger number of peaks in the resonance corresponds to the larger number of matrix elements. The comparison of the two different superlattice topologies shows that the envelopes of the resonance are practically identical in both cases. Only the details of the fine structure depend on the particular set of on-site energies ϵ_i used.

After crossing the transition to the quasi Bose-glass phase at $\Delta = U_0$, the resonance structure changes dramatically as shown in Fig. 2.13. Already at $\Delta/J_0 = 35$, i.e., slightly above the transition at $\Delta/J_0 = U_0/J_0 = 30$, the resonance is completely fragmented. There is no longer a smooth envelope with centroid at $\omega = U_0$. Instead, the strength is split into two groups of individual peaks: one group around the original resonance position and another group at low excitation energies. In particular, we observe low-lying resonances at $\omega/J_0 < 10$ – a regime where no response was observed for a system in the homogeneous Mott-insulator phase. With increasing superlattice amplitude, the response is shifted towards lower excitation energies, as indicated by the sequence of plots in Fig. 2.13. At $\Delta/J_0 = 50$, for instance, no response is left at the original resonance position $\omega = U_0$ and all peaks are concentrated at low excitation energies.

This characteristic behavior of the response appears to be a signature for the Mott-insulator to quasi Bose-glass transition for boson in superlattices, which is directly accessible to experiments. Nevertheless, the broadening of the resonance and emergence of low-lying strengths is similar to the response structure of the superfluid regime.

The comparison of the two different superlattice topologies, both with a period of five sites, demonstrates that the fine-structure of the response depends on the details of the superlattice, but that the gross characteristics are not affected.

Finally, one should note that the linear response analysis already hints at these substantial changes in the resonance spectrum. For larger superlattice amplitudes however, effects beyond the simple linear perturbation scheme become increasingly important and lead to significant discrepancies in comparison to the full time-dependent simulation (cf. Fig. 2.13 (c)).

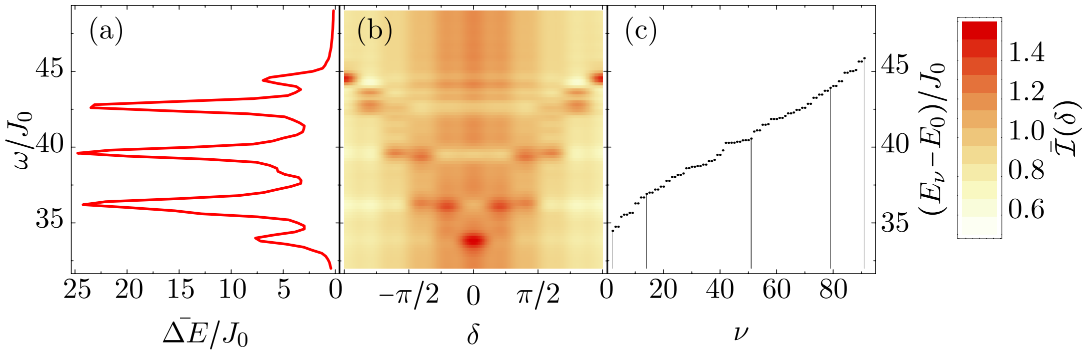

Fig. 2.14.: The U-resonance in a system with $I = N = 10$ at $U_0/J_0 = 40$ for a homogeneous lattice ($\Delta = 0$). Panel (a) illustrates the time-averaged energy transfer $\Delta\bar{E}$ versus the modulation frequency ω of the lattice. Panel (b) shows the corresponding time-averaged interference pattern which also represents the quasimomentum distribution. Panel (c) shows the energy spectrum in the region of the first Hubbard-band with the vertical lines indicating sizable matrix elements $\langle E_\nu | \mathbf{H}_J | E_0 \rangle$ (darker shadings refer to larger values). The truncation energy of the basis is $\mathcal{E}_{\text{trunc}}/J_0 = 120$.

2.5.3. Quasi-momentum distribution

General notes

In experiment, the response of a lattice system to a temporal modulation of the lattice amplitude is measured by the broadening of the central peak of the matter-wave interference pattern [36, 39]. The broadening of the central peak is related to changes in the quasimomentum distribution. In the following , we investigate the evolution of the interference pattern of the U-resonance of a system of 10 bosons on 10 sites of an homogeneous lattice. As a benchmark, we compare the results for different importance truncated bases. Finally, we investigate the evolution of the interference pattern and the quasimomentum distribution under an emerging superlattice potential in a system of 20 bosons on 20 sites.

Explicit time-evolution

In order to investigate the U-resonance and its structure in more detail, we perform an explicit time-evolution of a system of bosons in an optical lattice in the Mott regime and evaluate the quasi momentum expectation value $n_q(t_n)$ (1.30) at each time step t_n, which we introduced in Sect. 1.3.2. For the simulations, we focus on the modulation frequencies ω in the range of the U-resonance.

As a benchmark, we investigate a system of 10 boson on 10 sites of a homogeneous lattice at $U_0/J_0 = 40$. Figure 2.14 demonstrates the interplay of energy transfer, quasi momentum distribution, and the linear response analysis based on the static Hamiltonian at $t = 0$. Panel (a) 2.14 illustrates the energy transfer with the modulation frequency ω

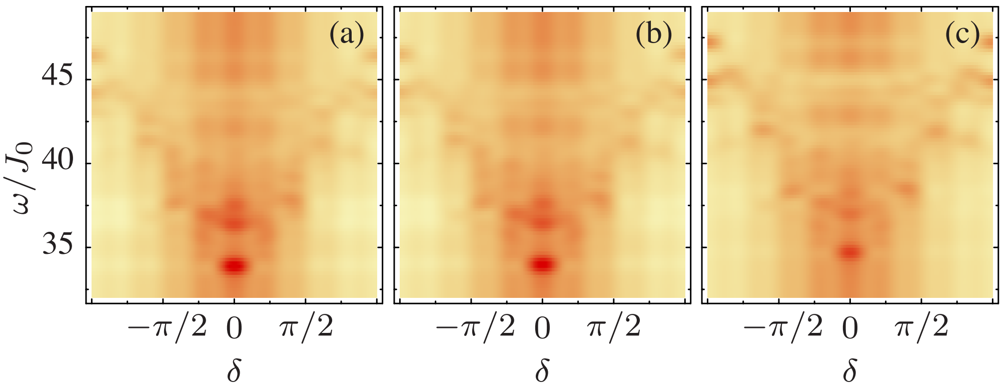

Fig. 2.15.: Interference pattern as function of ω in the region of the U resonance for a system with $I = N = 10$ at $U_0/J_0 = 40$ and $\Delta/J_0 = 2$ for truncation energies $E_{\text{trunc}}/J_0 = 120$ (a), $E_{\text{trunc}}/J_0 = 80$ (b), and $E_{\text{trunc}}/J_0 = 40$ (c). The shading is the same as in Fig. 2.14.

on the vertical axis.

Panel (c) of Fig. 2.14 shows the low energy part of the energy spectrum of the Hamiltonian at $t = 0$. The vertical lines indicate strong matrix elements $\langle E_\nu | \mathbf{H}_J | E_0 \rangle$ between ground state end excited states, which are susceptible to excitations via lattice modulations.

Panel (b) 2.14 represents the frequency-dependence of the quasimomentun-distribution in the region of the U resonance. Each horizontal cut through the density plot represents the time-averaged interference pattern for a certain modualtion frequency ω.

We assume that the lattice is switched off instantaneously after a certain evolution time in the modulated lattice — different from recent experiments which involve a rethermalization period in the superfluid regime [36, 39].

The general interference structure reveals a specific correlation between the frequency ω relative to the centroid of the U resonance and the quasimomentum distribution, i.e. the peaks of the interference pattern. Away from the resonance region, the intensity $\mathcal{I}(\delta)$ exhibits a broad background distribution characteristic for the Mott- insulating phase. For frequencies ω at the low-frequency end of the resonance a sharp interference peak emerges at $\delta = 0$ indicating the resonant transition to the $q = 0$ state. With increasing frequency ω this population moves to successively higher quasimomenta $|q|$, i.e. the interference peak splits and shifts towards larger $|\delta|$. The fine-structure of the resonance is thus mapped onto the interference pattern in an experimentally accessible way.

In order to perform these investigations on a system of experimentally relevant size, we have to employ a stronger truncated basis. We aim for a system of 20 sites and bosons. To analyze the impact of a smaller basis on the interference pattern, we evaluate the in-

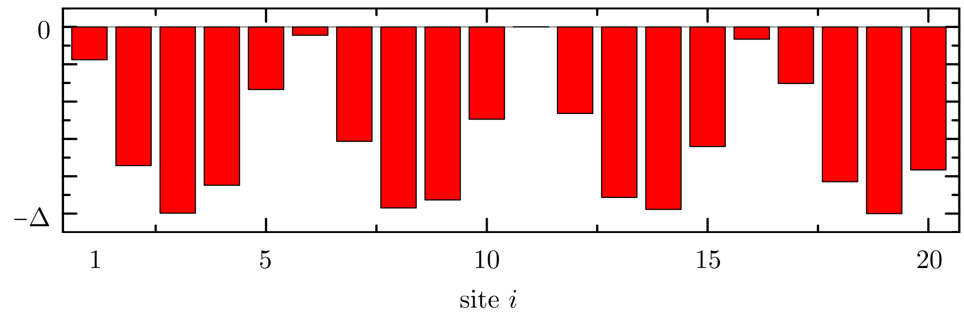

Fig. 2.16.: Distribution of the on-site energies ϵ_i of a superlattice of 20 sites. The superlattice is generated by superposition of two optical standing waves with incommensurate wave lengths.

terference pattern of a 10 site and boson system in the frequency range of the U resonance.

Figure 2.15 illustrates the insensitivity of the interference pattern on changes of $\mathcal{E}_{\text{trunc}}$. There is practically no difference when reducing the truncation energy from $\mathcal{E}_{\text{trunc}}/J_0 = 120$ (a) to 80 (b). Even for $\mathcal{E}_{\text{trunc}}/J_0 = 40$ (c) all relevant features are reproduced, although the intensity of the interference peaks shows slight deviations. As a consequence of the variational character of the importance trucation, the whole interference structure is shifted by $\sim J_0$ to higer modulation frequencies. Nevertheless, all qualitative conclusions regarding the correlations between frequency and quasimomentum distribution remain unaffected.

Quasimomentum distribution and superlattice potentials

Using the lowest truncation energy $\mathcal{E}_{\text{trunc}}/J_0 = 40$ we investigate the response of a system with $I = N = 20$ at $U_0/J_0 = 40$. The major focus is on the change of the response and the interference pattern if a two-color superlattice potential of increasing amplitude Δ is added. The distribution of the relative strengths ϵ_i for the superlattice used in the following are shown in Fig. 2.16. We have chosen a superlattice generated by the superposition of two optical standing waves with incommensurate wavelengths. That ensures that the four cells of the superlattice are not identical in their individual on-site energies ϵ_i, but show small deviations. This involves more energy steps in the system and has impact on the lobe structure of the quasi Bose-glass phase (cf. Sect. 1.3).

Figure 2.18 depicts the evolution of the interference structure as function of the superlattice amplitude Δ_0 for the in- commensurate case. The right-hand panels show the energy spectrum with vertical lines marking sizeable matrix elements $\langle E_\nu | \mathbf{H}_J | E_0 \rangle$. The left-hand panels depict the energy transfer as function of frequency. The result for $\Delta_0/J_0 = 0$ shown in (a) confirms our previous discussion of the smaller regular lattice in Fig. 2.14. The linear response analysis provides a good estimate for the resonance energies via the energies of those excited states that exhibit strong transition matrix elements to the ground state. Furthermore, the correlation between frequency ω and the quasimomentum distribution is even more pronounced. At the low-frequency end of the resonance quasimomentum states around $q \approx 0$ are populated, whereas for larger modulation frequencies successively higher quasi-momenta are occupied.

The results for a small superlattice amplitude $\Delta_0/J_0 = 1$ in (b) show minor changes in the quasimomentum structure and the energy transfer as compared to (a). Nevertheless, the number of possible excitations from the ground state increases. A further increase of the superlattice amplitude to $\Delta_0/J_0 = 2$ leads to a weak suppression of the interference structure as shown in (c). In comparison to the energy spectrum in (b) there are many more large matrix elements which are not localized at distinct energies but spread over the whole range. The occurrence of the small gaps at both ends of the energy band is also visible in the density plots as small shifts in the interference structure along the energy (vertical) axis. This also indicates the broadening of the resonance due to the superlattice [26, 36].

Further increase of the superlattice amplitude to $\Delta_0/J_0 = 4$ leads to the disappearance of the interference peaks as depicted in (d). The number of strong matrix elements which couple ground and excited states is further increased. Although the interference pattern does not show sharp peaks anymore, the energy transfer in these cases still exhibits a strong resonance behavior [26]. Only the fine-structure of the resonance in the energy transfer is affected by the superlattice. However, the distinct correlations between excitation frequency and quasimomentum distribution vanish far below the transition from the homogeneous Mott insulator to the Bose- glass phase at $\Delta_0 \approx U_0$.

The rapid change of the interference pattern can be explained in the linear response picture: In the absence of a superlattice, resonant transitions connect the ground state to a few excited states only — those characterized by large transition matrix elements $\langle E_\nu | \mathbf{H}_J | E_0 \rangle$ [Fig. 2.18(a) and (b)]. The many-body state $|\psi, t\rangle$ during the time evolution is dominated by these few states and exhibits well-defined interference peaks. With increasing superlattice amplitude Δ_0 more and more sizable transition matrix elements emerge and the time-evolved state is a superposition of a large number of eigenstates [Fig. 2.18 (c) and (d)]. The fragmentation of the state causes a fragmentation of the interference pattern and in effect a suppression of the distinct peaks. This mechanism can be confirmed within a simple toy-model by comparing the interference pattern of an excited eigenstate with the one resulting from a coherent superposition of a few neighboring eigenstates (Fig. 2.17). Note that this phenomenon is quite different from the Mott-insulator to Bose-glass transition, which appears at much larger superlattice amplitudes.

To sum up, we have shown that the interference pattern respectively the quasimomentum

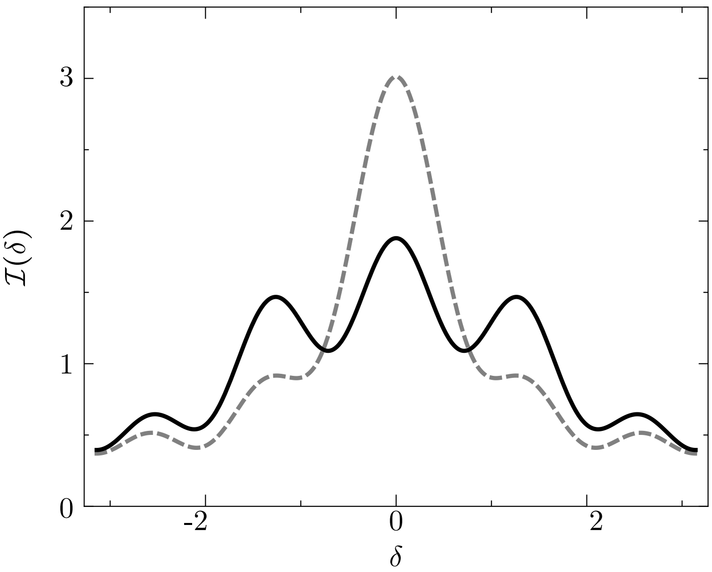

Fig. 2.17.: Interference pattern of the first excited state (– – –) and a coherent superposition of the first nine excited state (——) of a system with $I = N = 6$ and $U_0/J_0 = 20$.

distribution shows a strong correlation to the fine structure of the U resonance. More precisely, the individual peaks starting from the lower end of the resonance are based on excited states of successively increasing quasimomentum. Moreover, already weak admixtures of a superlattice potential lead to a smearing of the interference structure far below the transition to the quasi Bose-glass phase.

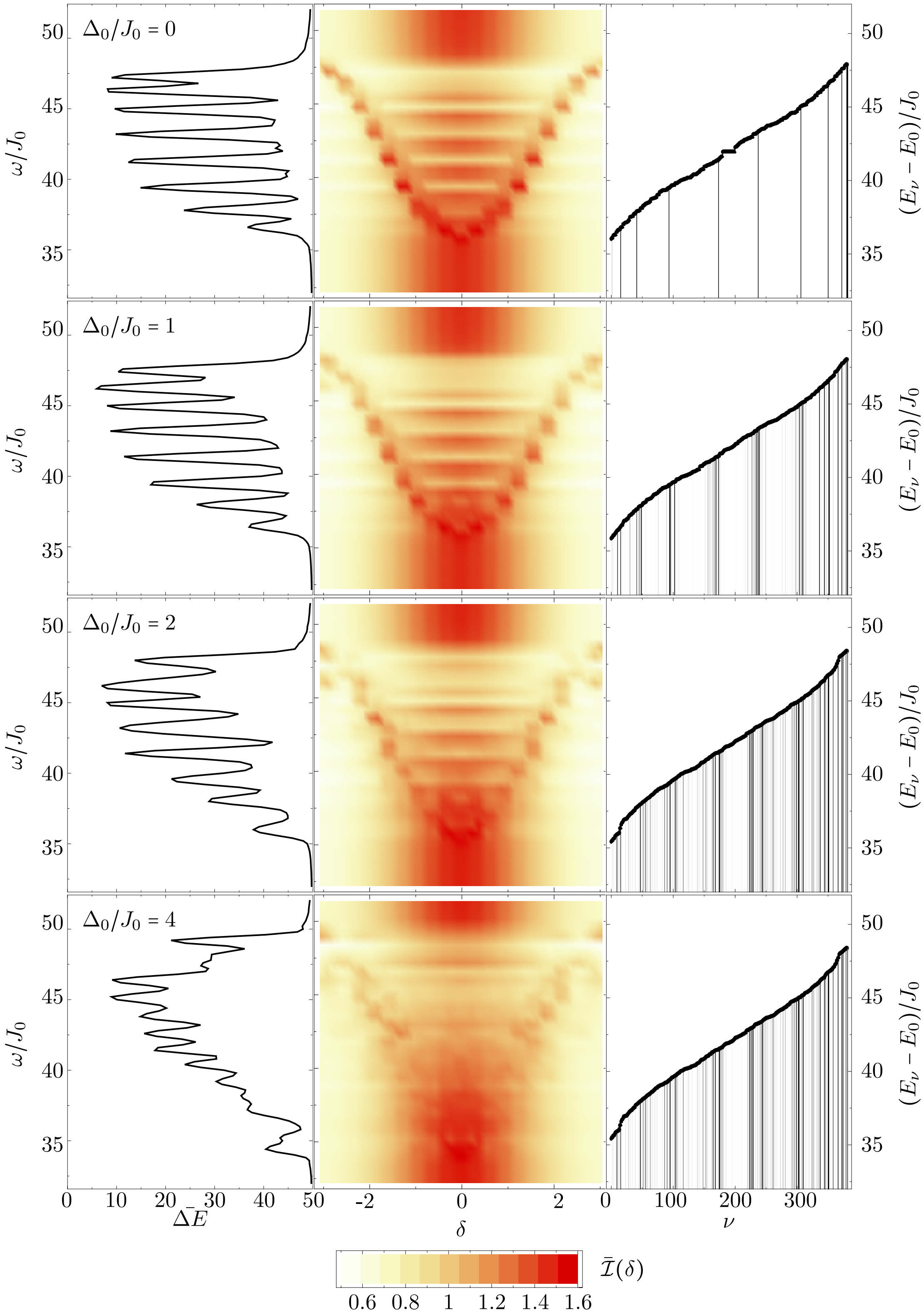

Fig. 2.18.: Energy transfer (left-hand panels), interference pattern (middle panels), and excitation spectrum (right-hand panels) of a system with $I = N = 20$ and $U_0/J_0 = 40$ for several superlattice amplitudes Δ_0 as indicated in the plots. The density plots illustrate the correlations between quasimomentum distribution and excitation frequency in the region of the U-resonance. The vertical lines in the energy spectra (right-hand panels) point out strong matrix elements $\langle E_\nu | \mathbf{H}_J | E_0 \rangle$

Chapter 3

Particle-hole methods

Particle-hole methods like the Tamm-Dancoff approximation (TDA) and the random-phase approximation (RPA) are valuable tools to study small amplitude modulations, like plasma oscillations [58] and collective excitations of atomic nuclei [59].

In this chapter, we want to adapt these methods to the Bose-Hubbard model (BHM), based on particle-hole excitations described in the number basis. Already for the importance truncation in Sect. 2.3 we utilized the feature that for strong interaction $U \gg J$, only a few number states are important to describe the low-lying eigenstates. This allows for a vast reduction of the numerical effort by retaining only a truncated model space spanned by the most important number states.

A corresponding reduction can also be achieved in the framework of TDA or RPA by describing the system in a space spanned by the particle-hole excitations of the ground state.

These methods allow for a very precise description of the low-energy properties of a bosonic lattice system under small lattice modulations. The U-resonance, in particular, is described by interacting particle-hole excitations.

3.1. Equations of motion (EOM)

An elegant way to introduce the Tamm-Dancoff approximation and the random-phase approximation is the *equations of motion* (EOM) method by Rowe [60]. We derive the

EOM in the following by starting with the Schrödinger equation (cf. Ref. [61]).

The stationary Schrödinger equation (SEQ) reads

$$\mathbf{H}\left|E_\nu\right\rangle = E_\nu \left|E_\nu\right\rangle, \tag{3.1}$$

with the eigenstates $\left|E_\nu\right\rangle$ and the energy eigenvalues E_ν. The excited states $\left|E_\nu\right\rangle$ with $\nu > 0$ can be written as an excitation of the ground state $\left|E_0\right\rangle$ by, what we will call in analogy to nuclei, the phonon operator

$$\left|E_\nu\right\rangle = \mathbf{Q}_\nu^\dagger \left|0\right\rangle. \tag{3.2}$$

In this formulation, the ground state is defined by $\mathbf{Q}_\nu \left|E_0\right\rangle = 0$, i.e., $\left|E_0\right\rangle$ is the *vacuum* of the phonon operators. The general structure of the phonon operators is given by

$$\mathbf{Q}_\nu^\dagger = \left|E_\nu\right\rangle\left\langle E_0\right| \qquad \text{and} \qquad \mathbf{Q}_\nu = \left|E_0\right\rangle\left\langle E_\nu\right| \tag{3.3}$$

in the projector notation. By plugging (3.2) into the Schrödinger equation (3.1) we get

$$\mathbf{H}\mathbf{Q}_\nu^\dagger \left|E_0\right\rangle = E_\nu \mathbf{Q}_\nu^\dagger \left|E_0\right\rangle.$$

With the subtraction of $\mathbf{Q}_\nu^\dagger \mathbf{H}\left|E_0\right\rangle$ on both sides one obtains the equations of motion (EOM) of the phonon operators,

$$[\mathbf{H}, \mathbf{Q}_\nu^\dagger]\left|E_0\right\rangle = E_{\nu 0}\mathbf{Q}_\nu^\dagger \left|E_0\right\rangle, \tag{3.4}$$

in which the eigenvalue relation for the ground state has been used on the right hand side and defined the excitation energy $E_{\nu 0} = E_\nu - E_0$.

With the multiplication of an arbitrary state $\left\langle E_0\right|\delta\mathbf{Q}$ from the left hand side, we can rewrite (3.4) into a stationary condition

$$\left\langle E_0\right|[\delta\mathbf{Q}, [\mathbf{H}, \mathbf{Q}_\nu^\dagger]]\left|E_0\right\rangle = E_{\nu 0}\left\langle E_0\right|[\delta\mathbf{Q}, \mathbf{Q}_\nu^\dagger]\left|E_0\right\rangle, \tag{3.5}$$

which has to be fulfilled any variation $\left\langle E_0\right|\delta\mathbf{Q}$. The outer commutators can be introduced since the extra terms vanish due to $\left\langle E_0\right|\mathbf{Q}_\nu^\dagger = \left\langle E_0\right|\mathbf{H}\mathbf{Q}_\nu^\dagger = 0$. In actual applications one resorts to approximate choices for the ground state (cf. Sect. 3.3.1). Since the hermiticity of equation (3.5) is not guaranteed for an approximate ground state [60], we generalize (3.5) to

$$\left\langle E_0\right|[\delta\mathbf{Q}, \mathbf{H}, \mathbf{Q}_\nu^\dagger]\left|E_0\right\rangle = E_{\nu 0}\left\langle E_0\right|[\delta\mathbf{Q}, \mathbf{Q}_\nu^\dagger]\left|E_0\right\rangle, \tag{3.6}$$

with the symmetrized double commutator

$$2[\delta\mathbf{Q}, \mathbf{H}, \mathbf{Q}_\nu^\dagger] = [\delta\mathbf{Q}, [\mathbf{H}, \mathbf{Q}_\nu^\dagger]] + [[\delta\mathbf{Q}, \mathbf{H}], \mathbf{Q}_\nu^\dagger]. \tag{3.7}$$

Equation (3.6) is the central equation in the following sections, since it provides the excitation energies and the phonon operators, which are related to the excited states.

3.2. Classification of particle-hole methods: phonon operator approximations

The equation of motion (3.6) is an exact equation, and its solution is therefore as demanding as the solution of the stationary Schrödinger equation. Since we are interested in the low-energy regime of the strongly interacting systems, only, we can resort to approximation schemes for the phonon operators that are able to describe the low-lying but not the high-lying energy eigenstates.

To achieve this, we expand the phonon operators in a set of operators which create particle-hole excitations up to a certain order. Since particle-hole excitations are the energetically lowest excitations in the BHM, one can approximate the phonon operators by retaining only the particle-hole terms.

Tamm-Dancoff approximation (TDA)

The most simple approximation of the phonon operators is the expansion in a series of operators $\mathbf{c}_k^\dagger$ which create 1-particle-1-hole excitations,

$$\mathbf{Q}_{\mathrm{TDA},\nu}^\dagger = \sum_k X_k^{(\nu)} \mathbf{c}_k^\dagger. \tag{3.8}$$

The precise form of $\mathbf{c}_k^\dagger$ is not yet defined and will be given in Sect. 3.3.2. Plugging the particle-hole operator (3.8) into the EOM (3.6) leads to the equations for the *Tamm-Dancoff approximation* (TDA). These equations are based on a space spanned by 1p1h-excitations of the ground state [61]. The solution of the TDA equation provides the amplitudes $X_k^{(\nu)}$ which then determine the excited states.

The TDA approach can be easily extended by adding higher-order particle-hole excitations. The phonon operator of the second (-order) TDA reads

$$\mathbf{Q}_{2^{\mathrm{nd}}\,\mathrm{TDA},\nu}^\dagger = \sum_k X_{1,k}^{(\nu)} \mathbf{c}_k^\dagger + \sum_{kk'} X_{2,kk'}^{(\nu)} \mathbf{c}_k^\dagger \mathbf{c}_{k'}^\dagger. \tag{3.9}$$

By also including $2p2h$ excitations, one introduces more correlations in the solutions which can possibly improve the accuracy. On the other hand, this enlarges the numerical problem to solve, and therefore requires more computational effort.

Random-phase approximation (RPA)

A more sophisticated approach is to include also particle-hole de-excitation operators $\mathbf{c}_{ph}$ backward terms. The lowest order terms of the phonon operator expansion reads

$$\mathbf{Q}_{\mathrm{RPA},\nu}^\dagger = \sum_k X_k^{(\nu)} \mathbf{c}_k^\dagger - \sum_k Y_k^{(\nu)} \mathbf{c}_k, \tag{3.10}$$

which leads to the equations of the random-phase approximation (RPA). In contrast to TDA, the additional particle-hole de-excitation terms also induce correlations in the ground state. Hence, the standard RPA presented here is the simplest particle-hole method which also improves on the ground state.

Due to the additional de-excitation terms, the dimension of the RPA matrices is twice as large as in TDA. The particle-hole methods like RPA provide the excited states via the phonon operators, but the construction of the ground state is non-trivial in general. In Fermi systems like nuclei, however, the reference state (Hartree-Fock state) is related to the RPA ground-state and can therefore be extracted from the phonon operators (Thouless theorem [62], cf. Ref. [61]). Since such a criterion does not exist for Bose systems, the RPA ground-state remains unknown.

3.3. Particle-hole methods and the Bose-Hubbard model

In order to define the equations of motion of the TDA and the RPA, we have to adapt the general expressions of the phonon-operators to the Bose-Hubbard model, which means to define the particle-hole excitation ($\mathbf{c}_k^\dagger$) and de-excitation ($\mathbf{c}_k$) operators and to find a reference state.

3.3.1. Reference state

Since the ground state is not known *a priori*, we require a suitable approximation to it, the so-called reference state $|\mathrm{ref}\rangle$. The most simple scenario is a system of N bosonic particles in $I = N$ sites of a homogeneous, translationally invariant, lattice. We are mainly interested in the dynamics in the strongly interacting regime, in which multiple occupancies of the lattice sites are suppressed due to the strong on-site interaction. Hence, the number state with one particle per site is a reasonable choice for the reference state.

In inhomogeneous lattices or systems with non-integer filling factor N/I, the reference state is usually not that simple. As an example we consider a system with 4 particles on 3 sites of a homogeneous lattice. In order to find an approximation to the ground state, a good starting point is to put the first 3 particles to individual sites. For the remaining particle there are three energetically degenerate options: we can put it on top of any one of the other three particles. Hence, a balanced choice for the reference state would be a superposition of all three states, a so-called *multi-reference state*:

$$|\mathrm{ref}\rangle = \frac{1}{\sqrt{3}} \left\{ |\overset{\circ}{\underline{\circ}}\,\underline{\circ}\,\underline{\circ}\rangle + |\underline{\circ}\,\overset{\circ}{\underline{\circ}}\,\underline{\circ}\rangle + |\underline{\circ}\,\underline{\circ}\,\overset{\circ}{\underline{\circ}}\rangle \right\}$$

Calculations with multi-reference states result in a much larger numerical effort, since the equations of motion have to be evaluated for each combination of states which make up the reference state. More precisely, the effort increases with the square of the number of states in the multi-reference state in comparison to a single reference calculation.

However, for the lattices in this work, a single number state with one particle per site is suitable, since we always consider an integer filling factor.

3.3.2. Particle-hole operators

The final ingredient to link the Bose-Hubbard model, i.e., the Hamiltonian (1.13), to the equations of motion (3.6) are the particle-hole operators, which we need to define the phonon operators completely. The task is, to find a set of operators $\mathbf{c}_k^\dagger$, $\mathbf{c}_k$ which can create and annihilate particle-hole excitations of the number states. The index k labels a certain particle-hole excitation, the so-called *configuration.*

As a particle-hole excitation of a number state we assume to take a particle from site j and place it on site i, hence, the the index pair i and j specifies a certain configuration k. We therefore use the notation $\mathbf{c}_{ij}^\dagger$ ($\mathbf{c}_{ij}$) for the particle-hole in the following. An example for a particle-hole excitation operator is

$$\mathbf{c}^\dagger_{31}\left|\underline{\circ}\,\underline{\circ}\,\underline{\circ}\,\underline{\circ}\right\rangle = \left|\underline{\ }\,\underline{\circ}\,\underline{\overset{\circ}{\circ}}\,\underline{\circ}\right\rangle. \tag{3.11}$$

and the corresponding particle-hole de-excitation operator reads

$$\mathbf{c}_{31}\left|\underline{\ }\,\underline{\circ}\,\underline{\overset{\circ}{\circ}}\,\underline{\circ}\right\rangle = \left|\underline{\circ}\,\underline{\circ}\,\underline{\circ}\,\underline{\circ}\right\rangle. \tag{3.12}$$

Naive two-operator approach

As a first ansatz, we employ the simple structure of particle-hole operators as used for Fermi systems [58, 60]. The state of a weakly interacting Fermi system of N particles is well approximated by a Slater determinant, in which the energetically lowest N single particle states are occupied. The highest occupied single-particle state defines the Fermi energy. A particle-hole excitation of such a state is produced by putting one particle from an occupied (hole) state into an unoccupied (particle) state above the Fermi energy. Such an excitation is realized by

$$\mathbf{c}^\dagger_{ph,\text{Fermi}} = \mathbf{a}^\dagger_{p,\text{Fermi}}\mathbf{a}_{h,\text{Fermi}}$$

and the according de-excitation is

$$\mathbf{c}_{ph,\text{Fermi}} = \mathbf{a}^\dagger_{h,\text{Fermi}}\mathbf{a}_{p,\text{Fermi}}.$$

The subscript *Fermi* in this case means that the particle creation and annihilation operators $\mathbf{a}^\dagger$, $\mathbf{a}$ obey the fermionic anticommutator relations.

We can try to map these particle-hole operators on a bosonic lattice system. We assume a homogeneous lattice with filling factor $N/I = 1$, i.e., the reference state is given by the number state with one particle per site, as discussed in Sect. 3.3.1. In a naive approach one might define the particle-hole creation operator via

$$\mathbf{c}^\dagger_{ij} = \frac{1}{\sqrt{2}}\mathbf{a}^\dagger_i\mathbf{a}_j \tag{3.13}$$

and the corresponding ph-annihilation operator via

$$\mathbf{c}_{ij} = \frac{1}{\sqrt{2}}\mathbf{a}^\dagger_j\mathbf{a}_i, \tag{3.14}$$

with the particle creation (annihilation) operators $\mathbf{a}^\dagger_i$ ($\mathbf{a}_i$), which obey the bosonic commutator relations. The indices i and j denote the sites where the operators are acting. As a consequence of the multiple occupation of the lattice sites in bosonic systems, we introduce the pre-factor $1/\sqrt{2}$ in the particle-hole operators, which ensures normalized excited number-states.

The factor is not strictly required for the equations of motion, because such a global factor does not change the solutions. However, without the pre-factors of the particle-hole operators one would have to normalize the excited states after extracting them from the phonon operators via $\big|E_\nu\big\rangle = \mathbf{Q}^\dagger_{(\nu)}\,\big|\mathrm{ref}\big\rangle$.

However, this naive approach of the particle-hole operators does not behave properly. This is due to the difference between an excitation in fermionic systems compared to bosonic lattice systems. In Fermi systems, the indices p and h refer to single-particle states, where h is restricted to occupied and p to unoccupied states [61]. In this case, the particle-hole excitation and de-excitation operators are well defined: For each pair of indices p and h, there exist exactly one particle-hole excitation operator which excites the particle in the state h (below the Fermi energy E_F) into the state p (above E_F), which can only be de-excited by exactly one particle-hole de-excitation operator. In the bosonic lattice systems, there exist no such particle (unoccupied) states. The naive approach to the particle-hole excitation operator (3.13) takes a particle from site $j = 2$ of the reference state $\big|\mathrm{ref}\big\rangle = \big|\underline{\circ}\,\underline{\circ}\,\underline{\circ}\,\underline{\circ}\,\underline{\circ}\big\rangle$ and places it on site $i = 4$,

$$\mathbf{c}^\dagger_{42}\,\big|\underline{\circ}\,\underline{\circ}\,\underline{\circ}\,\underline{\circ}\,\underline{\circ}\big\rangle = \big|\underline{\circ}\,\underline{}\,\underline{\circ}\,\underline{\overset{\circ}{\circ}}\,\underline{\circ}\big\rangle. \tag{3.15}$$

The respective de-excitation operator in the sense of the Fermi systems is $\mathbf{c}_{42}$,

$$\mathbf{c}_{42}\,\big|\underline{\circ}\,\underline{}\,\underline{\circ}\,\underline{\overset{\circ}{\circ}}\,\underline{\circ}\big\rangle = \big|\underline{\circ}\,\underline{\circ}\,\underline{\circ}\,\underline{\circ}\,\underline{\circ}\big\rangle. \tag{3.16}$$

However, if we apply this particle-hole de-excitation operator to the reference state we obtain

$$\mathbf{c}_{42}\,\big|\underline{\circ}\,\underline{\circ}\,\underline{\circ}\,\underline{\circ}\,\underline{\circ}\big\rangle = \big|\underline{\circ}\,\underline{\overset{\circ}{\circ}}\,\underline{\circ}\,\underline{}\,\underline{\circ}\big\rangle, \tag{3.17}$$

which is an excited state. That means, that the de-excitation operator can act as a particle-hole excitation operator, or in other words, the set of particle-hole creators contains exactly the same operators like the set of the annihilators.

In the fermionic case, both sets of operators are unique due to the restrictions to the indices p and h as discussed above. If we would try to de-excite a particle in single-particle state p of a slater determinant describing the ground state of a Fermi gas, the whole expression would vanish since p is not occupied. Consequently, we need to improve on the definition of the particle-hole operators in order to reproduce the behavior of the operators in Fermi systems.

Four-operator approach

In order to improve on the previous ansatz, we have to split the particle-hole excitation and particle-hole de-excitation operators in unique sets of operators. The key idea of the following approach is to prevent the particle-hole de-excitation operator from producing particle-hole excitations. For our reference state with one particle per site we achieve this by introducing an additional pair of particle creation and annihilation operators,

$$\begin{aligned}\mathbf{c}^\dagger_{ij} &= \frac{1}{\sqrt{2}}\mathbf{a}^\dagger_i\mathbf{a}^\dagger_i\mathbf{a}_i\mathbf{a}_j,\\ \mathbf{c}_{ij} &= \frac{1}{\sqrt{2}}\mathbf{a}^\dagger_j\mathbf{a}^\dagger_i\mathbf{a}_i\mathbf{a}_i.\end{aligned} \tag{3.18}$$

Due to its operator structure we call (3.18) the *four-operator approach.* If we apply the particle-hole de-excitation operator with $i = 4$ and $j = 2$ to the reference state we obtain

$$\mathbf{c}_{42}\,|\underline{\circ}\,\underline{\circ}\,\underline{\circ}\,\underline{\circ}\,\underline{\circ}\rangle = \frac{1}{\sqrt{2}}\mathbf{a}^\dagger_2\mathbf{a}^\dagger_4\mathbf{a}_4\mathbf{a}_4\,|\underline{\circ}\,\underline{\circ}\,\underline{\circ}\,\underline{\circ}\,\underline{\circ}\rangle = 0, \tag{3.19}$$

since the fourth site is singly occupied only. Hence, the structure of the de-excitation operator ensures, that it cannot excite the reference state, which is in analogy to the Fermi-gas example discussed before.

If we, however, de-excite a state which has been excited by $\mathbf{c}^\dagger_{42}$ before, we obtain

$$\mathbf{c}_{42}\left(\mathbf{c}^\dagger_{42}\,|\underline{\circ}\,\underline{\circ}\,\underline{\circ}\,\underline{\circ}\,\underline{\circ}\rangle\right) = \frac{1}{\sqrt{2}}\mathbf{a}^\dagger_2\mathbf{a}^\dagger_4\mathbf{a}_4\mathbf{a}_4\,|\underline{\circ}\,\underline{\;\;}\,\underline{\circ}\,\underline{\overset{\circ}{\circ}}\,\underline{\circ}\rangle = |\underline{\circ}\,\underline{\circ}\,\underline{\circ}\,\underline{\circ}\,\underline{\circ}\rangle, \tag{3.20}$$

which means, that the de-excitation operator works properly on that state in analogy to the fermionic example. At first glance, the four-operator approach seems to be the best choice, but besides $\mathbf{c}_{42}$ we can find $(I-1)$ additional particle-hole de-excitation operators which can act on the state $\mathbf{c}^\dagger_{42}\,|\underline{\circ}\,\underline{\circ}\,\underline{\circ}\,\underline{\circ}\,\underline{\circ}\rangle = |\underline{\circ}\,\underline{\;\;}\,\underline{\circ}\,\underline{\overset{\circ}{\circ}}\,\underline{\circ}\rangle$, i.e., those with $i = 4$ and $j \neq 2$. Exemplarily, we look at the operator $\mathbf{c}_{43}$,

$$\mathbf{c}_{43}\,|\underline{\circ}\,\underline{\;\;}\,\underline{\circ}\,\underline{\overset{\circ}{\circ}}\,\underline{\circ}\rangle = \frac{1}{\sqrt{2}}\mathbf{a}^\dagger_3\mathbf{a}^\dagger_4\mathbf{a}_4\mathbf{a}_4\,|\underline{\circ}\,\underline{\;\;}\,\underline{\circ}\,\underline{\overset{\circ}{\circ}}\,\underline{\circ}\rangle = \sqrt{2}\,|\underline{\circ}\,\underline{\;\;}\,\underline{\overset{\circ}{\circ}}\,\underline{\circ}\,\underline{\circ}\rangle = \mathbf{c}^\dagger_{32}\,|\underline{\circ}\,\underline{\circ}\,\underline{\circ}\,\underline{\circ}\,\underline{\circ}\rangle, \tag{3.21}$$

which just moves the double occupancy from the fourth to the third site. This is, strictly speaking, not a de-excitation of the state since the energy remains unchanged — the excited state was transferred into another excited state. In conclusion, for each particle-hole excited state $\mathbf{c}^\dagger_{ij}$, which can be de-excited by $\mathbf{c}_{ij}$, there are also $(I-1)$ operators $\mathbf{c}_{il}$ with $l \neq j$ which just transfer the excited state into an other excited state. We refer to this as the *double-occupancy-transfer* problem of the four-operator approach. Nevertheless, we use this set of operators in our calculations but should keep in mind, that they do not purely act as particle-hole creation/annihilation operators. The consequences of this behavior are addressed in later sections, when discussing the equations for TDA (Sect. 3.5) and RPA (Sect. 3.6).

Projector approach

In order to cure the *double-occupany-transfer* problem from the previous approach, we consider a third set of particle-hole operators. The basic requirements should be that the particle-hole creation operator $\mathbf{c}^\dagger_{ij}$ creates an excitation between sites i and j which can be de-excited by the according annihilator $\mathbf{c}_{ij}$, only. All other annihilators have to map the state to 0, i.e., the whole expression vanishes.

This can be achieved easily through a projector approach with the particle-hole creation operator

$$\mathbf{c}^\dagger_{ij} = \left|ij\right\rangle\left\langle\text{ref}\right| = \frac{1}{\sqrt{2}}\mathbf{a}^\dagger_i\mathbf{a}_j \left|\text{ref}\right\rangle\left\langle\text{ref}\right| \tag{3.22}$$

and the corresponding annihilation operator

$$\mathbf{c}_{ij} = \left|\text{ref}\right\rangle\left\langle ij\right| = \frac{1}{\sqrt{2}}\left|\text{ref}\right\rangle\left\langle\text{ref}\right|\mathbf{a}^\dagger_j\mathbf{a}_i\,. \tag{3.23}$$

The set $\{\left|ij\right\rangle\}$ contains all possible 1p1h-excited number states of the reference state $\left|\text{ref}\right\rangle$. The operators work as follows: In a first step, the particle-hole creator (3.22) projects the state on the reference state, which ensures that only the reference-state component can be excited. Then, a pair of particle creation/annihilation operators creates the 1p1h-state:

$$\mathbf{c}^\dagger_{ij}\left|\text{ref}\right\rangle = \left(\frac{1}{\sqrt{2}}\mathbf{a}^\dagger_i\mathbf{a}_j\left|\text{ref}\right\rangle\left\langle\text{ref}\right|\right)\left|\text{ref}\right\rangle = \frac{1}{\sqrt{2}}\mathbf{a}^\dagger_i\mathbf{a}_j\left|\text{ref}\right\rangle = \left|ij\right\rangle. \tag{3.24}$$

In case $\mathbf{c}^\dagger_{ij}$ acts on a state which is orthogonal to the reference state $\left|\text{ref}\right\rangle$, the whole expression vanishes. Since the number states are orthogonal by construction (cf. Sect. 1.2.2), this happens for every number state except the reference state.

This behavior of the particle-hole creator is a limitation of the approach, since it is not possible to excite an already excited number state any further. This has no impact on the TDA and RPA versions discussed in this work, but might be an issue for higher order methods like second RPA.

The particle-hole annihilation operator $\mathbf{c}_{ij}$ (3.23) works in the opposite direction. First, a particle is taken from site i and put on site j. After that, the state is projected onto the reference state in order to ensure that only states, which are excited by $\mathbf{c}^\dagger_{ij}$, can be de-excited,

$$\mathbf{c}_{ij}\left|ij\right\rangle = \left(\frac{1}{\sqrt{2}}\left|\text{ref}\right\rangle\left\langle\text{ref}\right|\mathbf{a}^\dagger_j\mathbf{a}_i\right)\left|ij\right\rangle = \left|\text{ref}\right\rangle\left\langle\text{ref}|\text{ref}\right\rangle = \left|\text{ref}\right\rangle. \tag{3.25}$$

Otherwise, the whole expression vanishes due to the orthogonality of the number state basis.

In conclusion, we have presented three ansätze for particle-hole operators which enable us to formulate the general EOM (3.6) in the number basis representation of the Bose-Hubbard model. In the following sections, we will derive the equations of TDA and RPA based on the *projector* and *four-operator* approach and discuss the results we obtained with it. As an overview, table 3.1 summarizes all three approaches.

ansatz	suitable	properties
$\frac{1}{\sqrt{2}}\mathbf{a}_i^\dagger \mathbf{a}_j$		• creation and annihilation operators belong to identical sets
$\frac{1}{\sqrt{2}}\mathbf{a}_i^\dagger \mathbf{a}_i^\dagger \mathbf{a}_i^\dagger \mathbf{a}_j$	✓	• particle-hole operators can act as hopping operators • can be extended easily by extension of the strings of operators (higher excitations)
$\frac{1}{\sqrt{2}}\mathbf{a}_i^\dagger \mathbf{a}_j \left\vert \mathrm{ref} \right\rangle \left\langle \mathrm{ref} \right\vert$	✓	• reproduces creation/annihilation operator properties accurately • no straight forward extension as the previous approach due to the projection on the reference state

Tab. 3.1.: Comparison of the three approaches for the particle-hole operators

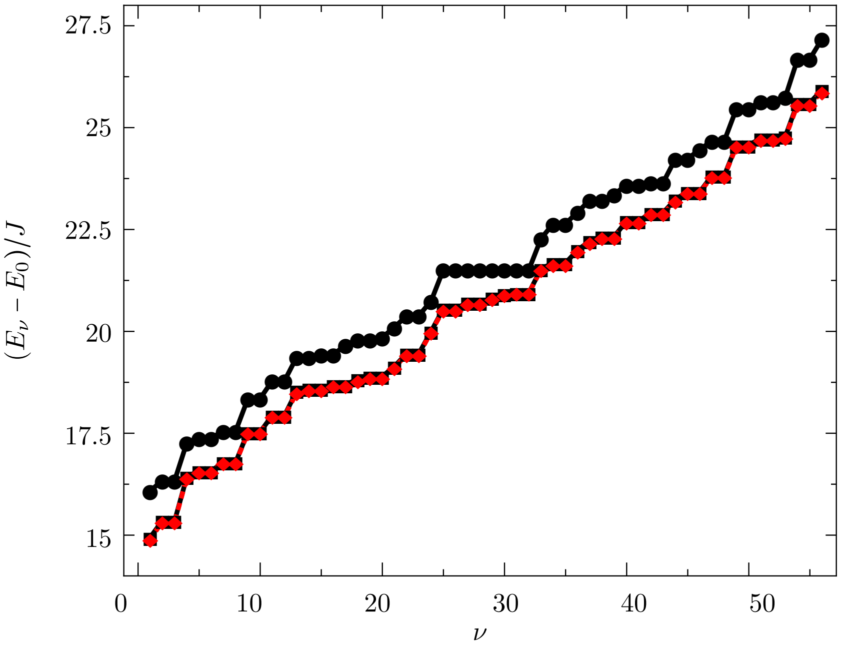

Fig. 3.1.: Excitation energies $(E_\nu - E_0)$ of the first Hubbard band for a system with $I = N = 8$ and $U/J = 20$ obtained by solving the Schrödinger equation in 0p0h+1p1h- (—●—), 0p0h+1p1h+2p2h- (—■—), and 0p0h+1p1h+2p2h+3p3h-space (—◆—).

3.4. Schrödinger equation in particle-hole space

Before we turn to particle-hole methods like TDA and RPA, we perform some calculations to compare with. From the discussion in the previous sections we have shown, that the equation of motion along with the approximation of the phonon operator is closely related to solving the Schrödinger equation in a limited particle-hole space. Therefore, it would be convenient to study the Schrödinger equation in the model space spanned by particle-hole excitations with respect to the reference state as benchmark calculation.

The basic difference between solving the Schrödinger equation (SEQ) and solving the TDA for example is inclusion of the reference state in the model space for the SEQ. Figure 3.1 illustrates the energies of the first Hubbard band of a system with $I = N = 8$ and the interaction strength $U/J = 20$ obtained by solving the Schrödinger equation in different particle-hole spaces. Let us look at the two results in the larger spaces at first. The energies obtained in 0p0h+1p1h+2p2h- (S2PH) and in 0p0h+1p1h+2p2h+3p3h-space (S3PH) show no significant deviations from each other. That means, that the additional 3p3h-states of the S3PH does not provide important contributions to the energies of the first Hubbard band. Since larger model spaces just include even more energetically unfavorable number states (4p4h-states and beyond), we use the S2PH calculations as reference in the following sections.

The energies from the solution in 0p0h+1p1p-space (SPH) lie a few J above the solutions in the larger model spaces, which is indicates the variational character of the truncation (Hyleraas-Undheim theorem [56]). Nevertheless, we use the SPH results for the comparison with the TDA in the next section, since both methods operate in the same model space and are, therefore, closely related.

3.5. Tamm-Dancoff approximation (TDA)

3.5.1. Phonon operators and TDA equation

The Tamm-Dancoff approximation is based on the simplest approximation for the phonon operators entering into the equations of motion (3.6). The phonon operator leading to the TDA equations consists of 1-particle-1-hole excitation terms only,

$$\mathbf{Q}^{\dagger}_{\mathrm{TDA},\nu} = \sum_{\{ij\}} X^{(\nu)}_{ij} \mathbf{c}^{\dagger}_{ij}, \tag{3.26}$$

where the sum is running over all possible pairs of site indices $\{ij\}$ with $i \neq j$. The method is, therefore, limited to 1p1h-excitations of the reference state. Plugging the phonon operator (3.26) into the equation of motion (3.6) leads to

$$\langle \mathrm{ref} | \, [\delta \mathbf{Q}, \mathbf{H}, \mathbf{Q}^{\dagger}_{\mathrm{TDA},\nu}] | \mathrm{ref} \rangle = E_{\nu 0} \langle \mathrm{ref} | \, [\delta \mathbf{Q}, \mathbf{Q}^{\dagger}_{\mathrm{TDA},\nu}] | \mathrm{ref} \rangle, \tag{3.27}$$

with the excitation energy $E_{\nu 0} = E_{\nu} - E_0$. By substitution of the variation

$$\delta \mathbf{Q}^{\dagger} = \sum_{\{i'j'\}} \delta X_{i'j'} \mathbf{c}^{\dagger}_{i'j'} \tag{3.28}$$

and the phonon operator (3.26) into equation (3.27) we obtain

$$\sum_{\{i'j'\}\{ij\}} \langle \mathrm{ref} | \, [\mathbf{c}_{i'j'}, \mathbf{H}, \mathbf{c}^{\dagger}_{ij}] | \mathrm{ref} \rangle X^{(\nu)}_{ij} \delta X_{i'j'} = E_{\nu 0} \sum_{\{i'j'\}\{ij\}} \langle \mathrm{ref} | \, [\mathbf{c}_{i'j'}, \mathbf{c}^{\dagger}_{ij}] | \mathrm{ref} \rangle X^{(\nu)}_{ij} \delta X_{i'j'}. \tag{3.29}$$

We can now bring both terms of equation (3.29) to one side and reorganize the sums to

$$0 = \sum_{\{i'j'\}} \left(\sum_{\{ij\}} \langle \mathrm{ref} | \, [\mathbf{c}_{i'j'}, \mathbf{H}, \mathbf{c}^{\dagger}_{ij}] | \mathrm{ref} \rangle X^{(\nu)}_{ij} - E_{\nu 0} \sum_{\{ij\}} \langle \mathrm{ref} | \, [\mathbf{c}_{i'j'}, \mathbf{c}^{\dagger}_{ij}] | \mathrm{ref} \rangle X^{(\nu)}_{ij} \right) \delta X_{i'j'}. \tag{3.30}$$

Since equation (3.30) has to be true for any $\delta X_{i'j'}$, the expression in the parentheses has to be identically zero, which leads to the equations of motion of the TDA,

$$\sum_{\{ij\}} \langle \mathrm{ref} | \, [\mathbf{c}_{i'j'}, \mathbf{H}, \mathbf{c}^{\dagger}_{ij}] | \mathrm{ref} \rangle X^{(\nu)}_{ij} = E_{\nu 0} \sum_{\{ij\}} \langle \mathrm{ref} | \, [\mathbf{c}_{i'j'}, \mathbf{c}^{\dagger}_{ij}] | \mathrm{ref} \rangle X^{(\nu)}_{ij}. \tag{3.31}$$

The sums on both sides of equation (3.31) can be expressed as matrix-vector products, where we identify the matrix elements

$$A_{iji'j'} = \langle \mathrm{ref} | \, [\mathbf{c}_{i'j'}, \mathbf{H}, \mathbf{c}^{\dagger}_{ij}] | \mathrm{ref} \rangle. \tag{3.32}$$

on the left hand side of (3.31) which are multiplied by the vector $X^{(\nu)}_{ij}$. On the right hand side of (3.31) we can define the metric matrix $\underline{M}$, which is an identity matrix since the particle-hole operators obey the bosonic commutator relations,

$$M_{iji'j'} = \langle \mathrm{ref} | [\mathbf{c}_{i'j'}, \mathbf{c}^{\dagger}_{ij}] | \mathrm{ref} \rangle = \delta_{ii'} \delta_{jj'}. \tag{3.33}$$

With the definitions (3.32) and (3.33) the variational TDA equation (3.31) can be formulated as a compact eigenproblem

$$\underline{A}X^{(\nu)} = E_{\nu 0}X^{(\nu)}, \tag{3.34}$$

in which the metric matrix has been left out for clarity.

To solve the eigenproblem (3.34) we have to construct the matrix $\underline{A}$ by evaluating the matrix elements (3.32). In order to reduce the numerical effort, we should check, whether there are terms of the matrix elements which always vanish. Table 3.2 summarizes this for the individual terms of the double commutator in (3.32) for the particle-hole operators.

Analysis of the TDA matrix elements

The expanded the double commutator of $A_{iji'j'}$ reads

$$\begin{aligned} A_{iji'j'} =& \big\langle \mathrm{ref} \big| \big[\mathbf{c}_{ij}, \mathbf{H}, \mathbf{c}^{\dagger}_{i'j'} \big] \big| \mathrm{ref} \big\rangle \\ =& \frac{1}{2}\Big(\quad 2\big\langle \mathrm{ref} \big| \mathbf{c}_{ij}\mathbf{H}\mathbf{c}^{\dagger}_{i'j'} \big| \mathrm{ref} \big\rangle & (3.35) \\ & - \big\langle \mathrm{ref} \big| \mathbf{c}_{ij}\mathbf{c}^{\dagger}_{i'j'}\mathbf{H} \big| \mathrm{ref} \big\rangle & (3.36) \\ & - \big\langle \mathrm{ref} \big| \mathbf{H}\mathbf{c}_{ij}\mathbf{c}^{\dagger}_{i'j'} \big| \mathrm{ref} \big\rangle & (3.37) \\ & - \big\langle \mathrm{ref} \big| \mathbf{H}\mathbf{c}^{\dagger}_{i'j'}\mathbf{c}_{ij} \big| \mathrm{ref} \big\rangle & (3.38) \\ & - \big\langle \mathrm{ref} \big| \mathbf{c}^{\dagger}_{i'j'}\mathbf{c}_{ij}\mathbf{H} \big| \mathrm{ref} \big\rangle & (3.39) \\ & + 2\big\langle \mathrm{ref} \big| \mathbf{c}^{\dagger}_{i'j'}\mathbf{H}\mathbf{c}_{ij} \big| \mathrm{ref} \big\rangle \Big). & (3.40) \end{aligned}$$

The particle-hole de-excitation operators do map the reference state to zero by construction, hence, the term $-\big\langle \mathrm{ref} \big| \mathbf{H}\mathbf{c}^{\dagger}_{i'j'}\mathbf{c}_{ij} \big| \mathrm{ref} \big\rangle$ (3.38) vanishes trivially. Analogously, the terms $-\big\langle \mathrm{ref} \big| \mathbf{c}^{\dagger}_{i'j'}\mathbf{c}_{ij}\mathbf{H} \big| \mathrm{ref} \big\rangle$ (3.39) and $2\big\langle \mathrm{ref} \big| \mathbf{c}^{\dagger}_{i'j'}\mathbf{H}\mathbf{c}_{ij} \big| \mathrm{ref} \big\rangle$ (3.40) vanish, since the creation operator is applied to the reference state on the left hand side.

The first term $2\big\langle \mathrm{ref} \big| \mathbf{c}_{ij}\mathbf{H}\mathbf{c}^{\dagger}_{i'j'} \big| \mathrm{ref} \big\rangle$ (3.35) does not vanish. The operators on both sides of the Hamiltonian in this term produce particle-hole excited states, so this term represents the Hamiltonian expanded in the 1p1h-space with respect to the reference state.

For the remaining two terms $-\big\langle \mathrm{ref} \big| \mathbf{c}_{ij}\mathbf{c}^{\dagger}_{i'j'}\mathbf{H} \big| \mathrm{ref} \big\rangle$ (3.36) and $-\big\langle \mathrm{ref} \big| \mathbf{H}\mathbf{c}_{ij}\mathbf{c}^{\dagger}_{i'j'} \big| \mathrm{ref} \big\rangle$ (3.37) the four-operator-type and projector-type particle-hole operator show a different behavior. Since (3.37) is of the form of the complex conjugate of (3.36),

$$\big\langle \mathrm{ref} \big| \mathbf{c}_{ij}\mathbf{c}^{\dagger}_{i'j'}\mathbf{H} \big| \mathrm{ref} \big\rangle^{*} = \big\langle \mathrm{ref} \big| \big(\mathbf{c}_{ij}\mathbf{c}^{\dagger}_{i'j'}\mathbf{H} \big)^{\dagger} \big| \mathrm{ref} \big\rangle = \big\langle \mathrm{ref} \big| \mathbf{H}\mathbf{c}_{i'j'}\mathbf{c}^{\dagger}_{ij} \big| \mathrm{ref} \big\rangle,$$

we discuss (3.36) only.

The operator $\mathbf{c}_{ij}$ in (3.36) creates a 1-particle-1-hole state $\langle ph|$ on the left hand side and the tunneling term of the Bose-Hubbard Hamiltonian (1.13) can produce a next-neighbor 1-particle-1-hole excited state $|\mathrm{nn}ph\rangle$, hence, we obtain for (3.36)

$$\langle \mathrm{ref}|\,\mathbf{c}_{ij}\mathbf{c}^{\dagger}_{i'j'}\mathbf{H}_J|\mathrm{ref}\rangle = \langle ph|\,\mathbf{c}^{\dagger}_{i'j'}|\mathrm{nn}ph\rangle. \tag{3.41}$$

This general expression is valid for both approaches of the particle-hole operators. The difference between them emerges when applying the particle-hole creation operator to the ket on the right hand side (3.41):

- **Projector-type particle-hole operator.** The term vanishes for the projector-type operator, since it projects on the reference state first, which is orthogonal to the next-neighbor excited state,

  $$\langle ph|\,\mathbf{c}^{\dagger}_{i'j'}|\mathrm{nn}ph\rangle = \langle ph|\,\left(\mathbf{a}^{\dagger}_{i'}\mathbf{a}_{j'}\,|\mathrm{ref}\rangle\langle\mathrm{ref}|\,\right)\,|\mathrm{nn}ph\rangle = 0. \tag{3.42}$$

- **Four-operator type particle-hole operator.** For the discussion, we assume a system of 4 bosons on 4 sites and the states $|ph\rangle = |\underline{\circ}\,\underline{}\,\underline{\circ}\,\underline{\overset{\circ}{\circ}}\rangle$ and $|\mathrm{nn}ph\rangle = |\underline{\circ}\,\underline{}\,\underline{\overset{\circ}{\circ}}\,\underline{\circ}\rangle$, without loss of generality. Equation (3.41) reads then

  $$\langle ph|\,\mathbf{c}^{\dagger}_{i'j'}|\mathrm{nn}ph\rangle = \frac{1}{\sqrt{2}}\langle\underline{\circ}\,\underline{}\,\underline{\circ}\,\underline{\overset{\circ}{\circ}}|\,\mathbf{a}^{\dagger}_{i'}\mathbf{a}^{\dagger}_{i'}\mathbf{a}_{i'}\mathbf{a}_{j'}\,|\underline{\circ}\,\underline{}\,\underline{\overset{\circ}{\circ}}\,\underline{\circ}\rangle. \tag{3.43}$$

  If we now consider the indices $i' = 4$ and $j' = 3$, the string of operators of the right hand side of (3.43) *transfers* the double occupation from the third to the fourth site in the ket on the right hand side, hence, the term is finite.

For the interaction term and the on-site potential term of the Hamiltonian (1.13) both particle-hole operator approaches behave identically. As an example, we evaluate the interaction term of the Hamiltonian (1.13) $\mathbf{H}_U$:

$$\langle \mathrm{ref}|\,\mathbf{c}_{ij}\mathbf{c}^{\dagger}_{i'j'}\mathbf{H}_U\,|\mathrm{ref}\rangle = \langle \mathrm{ref}|\,\mathbf{c}_{ij}\mathbf{c}^{\dagger}_{i'j'}\left(\frac{1}{2}\sum_{k=1}^{I}\mathbf{n}_k(\mathbf{n}_k - 1)\right)|\mathrm{ref}\rangle. \tag{3.44}$$

Since the number basis is the eigenbasis of the interaction and the on-site energy operator of the Hamiltonian, the reference state on the right hand side is just scaled by the respective value of the matrix element $\langle \mathrm{ref}|\,\mathbf{H}_U|\mathrm{ref}\rangle = \frac{1}{2}\sum_{k=1}^{I} n_k(n_k - 1)$

$$\langle \mathrm{ref}|\,\mathbf{c}_{ij}\mathbf{c}^{\dagger}_{i'j'}\mathbf{H}_U\,|\mathrm{ref}\rangle = \frac{1}{2}\sum_{k=1}^{I} n_k(n_k - 1)\langle \mathrm{ref}|\,\mathbf{c}_{ij}\mathbf{c}^{\dagger}_{i'j'}\,|\mathrm{ref}\rangle, \tag{3.45}$$

with the occupation numbers n_k of the sites k of the reference state.

The matrix element $\langle \mathrm{ref}|\,\mathbf{c}_{ij}\mathbf{c}^{\dagger}_{i'j'}\,|\mathrm{ref}\rangle$ evaluates trivially to

$$\langle \mathrm{ref}|\,\mathbf{c}_{ij}\mathbf{c}^{\dagger}_{i'j'}\,|\mathrm{ref}\rangle = \delta_{ij}\delta_{i'j'} \tag{3.46}$$

$\mathbf{c}_{ij}^\dagger$	$\langle \mathrm{ref} \vert \mathbf{c}_{ij}\mathbf{H}\mathbf{c}_{i'j'}^\dagger \vert \mathrm{ref}\rangle$	$-\langle \mathrm{ref} \vert \mathbf{c}_{ij}\mathbf{c}_{i'j'}^\dagger\mathbf{H} \vert \mathrm{ref}\rangle$	$-\langle \mathrm{ref} \vert \mathbf{H}\mathbf{c}_{ij}\mathbf{c}_{i'j'}^\dagger \vert \mathrm{ref}\rangle$
$\frac{1}{\sqrt{2}}\mathbf{a}_i^\dagger\mathbf{a}_j \vert \mathrm{ref}\rangle\langle \mathrm{ref}\vert$	•	○	○
$\frac{1}{\sqrt{2}}\mathbf{a}_i^\dagger\mathbf{a}_i^\dagger\mathbf{a}_i^\dagger\mathbf{a}_j$	•	•	•

Tab. 3.2.: Comparison of the non-trivially vanishing terms of the TDA matrix elements $A_{iji'j'}$ for a homogeneous lattice system and filling factor $N/I = 1$. As reference state the number state with one particle per site is assumed. (○ vanishing, • non-vanishing)

for both types of particle-hole operators. Hence, for the reference state with one particle per site the contribution from the interaction term is vanishing.

For our standard reference state with one particle per site the matrix element (3.45) vanishes, however, for a reference state with multiply occupied sites one would obtain diagonal elements ($i = i'$ and $j = j'$). For the on-site potential term of the Hamiltonian (1.13), which is proportional to $\mathbf{n}_k$ rather than $\mathbf{n}_k(\mathbf{n}_k - 1)$ one obtains diagonal elements generally for any reference state.

In summary, we obtain differences in some TDA matrix elements (3.32) for the projector-type and four-operator-type particle-hole operator when evaluating the hopping operator $\mathbf{H}_J$ of the Hamiltonian. The differences in the individual terms of the matrix element are summarized in table 3.2 for a system with filling factor $N/I = 1$.

3.5.2. Projector-type TDA vs. SPH

The TDA equations are solved via a matrix eigenproblem (3.34). For the projector-type ansatz of the particle-hole operators we have found that only one term of the double commutator (3.32) contributes to the matrix elements,

$$A_{iji'j'} = \langle \mathrm{ref} \vert \mathbf{c}_{ij}\mathbf{H}\mathbf{c}_{i'j'}^\dagger \vert \mathrm{ref}\rangle. \tag{3.47}$$

For our reference state, these matrix elements are identical to those of the Hamiltonian

$$\langle \mathrm{ref} \vert \mathbf{c}_{ij}\mathbf{H}\mathbf{c}_{i'j'}^\dagger \vert \mathrm{ref}\rangle = \langle ij \vert \mathbf{H} \vert i'j'\rangle = H_{iji'j'}, \tag{3.48}$$

expanded in the 1p1h-space, with the index i representing the *excited* (doubly occupied) site and j the un-occupied site in the state $\vert ij\rangle$.

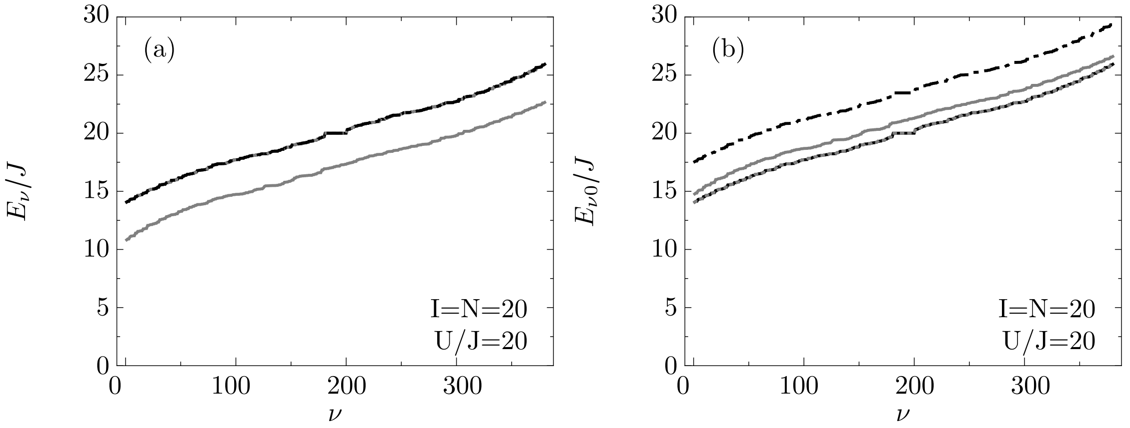

Fig. 3.2.: Absolute energies (a) and excitation energies (b) of the first Hubbard band of 20 bosons on 20 sites of an homogeneous lattice at $U/J = 20$. Shown are the solutions obtained via SPH (-·-·-), S2PH (——), 4TDA (------) and pTDA (——). The pTDA and 4TDA results are equal in (a) and (b) since TDA provides excitation energies, only.

3.5.3. Energy spectra

In this section, we discuss the energy spectra of a system of 20 bosons in an homogeneous optical lattice of 20 sites in the strongly interacting regime obtained via TDA. We present the results for the projector-type particle-hole operators (pTDA) and four-operator-type particle-hole operators (4TDA). Due to the similarities between pTDA and solving the Schrödinger equation in 0p0h+1p1h-space (SPH) we include also the SPH results. As benchmark we employ solutions of the Schrödinger equation in 0p0h+1p1h+2p2h-space (S2PH) we discussed in Sect. 3.4.

Let us at first compare the absolute energies computed by the different methods in Fig. 3.2 (a). We know from direct comparison to S3PH calculations [cf. Sect. 3.4] that the S2PH (solution of the Schrödinger equation in 0p0h+1p1h+2p2h-space) provides precise results for the first Hubbard band at strong interactions. Hence, we employ the S2PH energies as reference.

The similarity between the SPH, pTDA, and 4TDA manifests in the matching energies in Fig. 3.2 (a). The energies obtained by these methods lie about $4J$ above the S2PH energies, which reflects the more severe truncation to the 0p0h+1p1h-space [56].

Qualitative differences between the TDAs and SPH emerge when comparing the excitation energies $\Delta E_\nu = E_\nu - E_0$ in Fig. 3.2 (b). Since the TDAs provide the excitation energies directly, their values remain unchanged. Both TDA results lie close to the energies of the S2PH, which are shifted by the ground-state energy $E_\nu^{\mathrm{S2PH}}/J = -3.95$. The excitation energies of the SPH, however, are shifted by $E_\nu^{\mathrm{SPH}}/J = -3.47$ and lie $4J$ above the reference energies.

In conclusion, the excitation energies of pTDA and 4TDA are in good agreement with the benchmark calculation (S2PH). This is remarkable, since the dimension of the eigenproblems of the TDAs and S2PH differ by two orders of magnitude ($D_{\mathrm{xTDA}} = 380$ and $D_{\mathrm{S2PH}} = 32871$). Moreover, the TDAs show a vast improvement on the excitation energies in comparison to the SPH calculations despite their similar model spaces.

3.5.4. Strength functions

Based on the excitation energies and the excited states of a system one can define the strength function which allows for the comparison with the response in lattice modulation experiments [36, 39]. In Sect. 2.2 we have identified the tunneling operator as the operator responsible for the transition between the ground state and the excited states by linearization of the Bose-Hubbard Hamiltonian [24, 25].

We can apply these findings to evaluate the strength functions based on the Tamm-Dancoff approximation. An important ingredient of the strength functions is the transition amplitude from the reference state $|\mathrm{ref}\rangle$ to an excited state $|E_\nu\rangle$. These transition amplitudes can be calculated directly using the phonon operators $\mathbf{Q}^\dagger_{\mathrm{TDA},\nu}$, which we obtain from the solution of TDA,

$$\begin{aligned} \langle E_\nu | \mathbf{H}_J | E_0 \rangle = \langle E_0 | \mathbf{Q}_{\mathrm{TDA},\nu} \mathbf{H}_J | E_0 \rangle &= \langle E_0 | [\mathbf{Q}_{\mathrm{TDA},\nu}, \mathbf{H}_J] | E_0 \rangle && (3.49) \\ &\approx \langle \mathrm{ref} | [\mathbf{Q}_{\mathrm{TDA},\nu}, \mathbf{H}_J] | \mathrm{ref} \rangle. && (3.50) \end{aligned}$$

We can introduce the commutator in the last step, since $\mathbf{Q}_{\mathrm{TDA},\nu} |E_0\rangle$ vanishes. In the present definition, pTDA and 4TDA are able to describe the U-resonance which is based on excitations from the ground state to states in the first Hubbard band.

As benchmark for the TDA results we also show the strength function based on solutions of the Schrödinger equation (SPH and S2PH). The solutions of the Schrödinger equation (SPH and S2PH) provide the excited states $|E_\nu\rangle$ directly and the excitation energies are given by $E_{\nu 0} = E_\nu - E_0$. We employ the gaussian strength function (GSF) and the perturbative strength function (PSF) which we defined in Sect. 2.2 for the linear response analysis.

Gaussian strength function (GSF)

The Gaussian strength function (GSF) is given by weighting the product of a Gaussian function $G_\sigma(\omega - E_{\nu 0})$ of the width σ and a transition probability from the reference state $|\mathrm{ref}\rangle$ into the excited state $|E_\nu\rangle$ with the according excitation energy $E_{\nu 0}$,

$$R_{\mathrm{GSF}}(\omega) = \sum_\nu E_{\nu 0}\, G_\sigma(\omega - E_{\nu 0}) |\langle \mathrm{ref} | [\mathbf{Q}_{\mathrm{TDA},\nu}, \mathbf{H}_J] | \mathrm{ref} \rangle|^2. \tag{3.51}$$

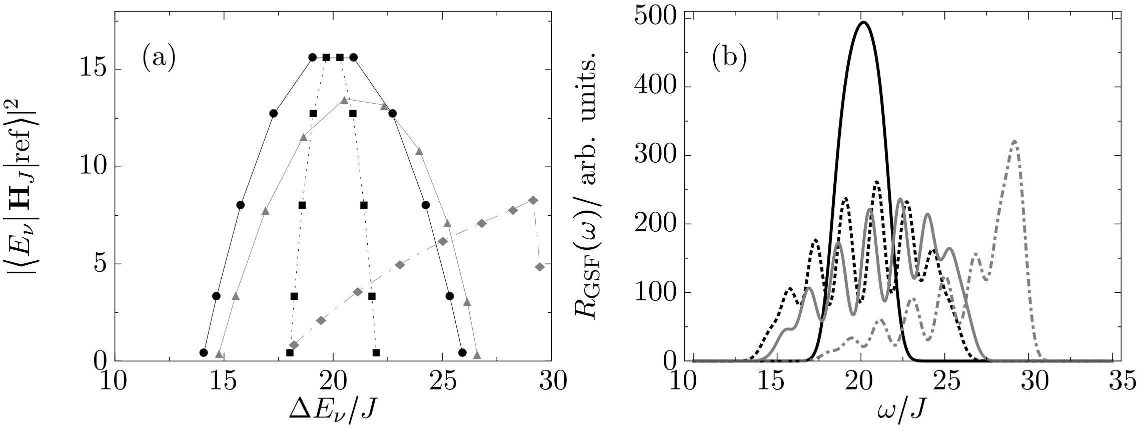

Fig. 3.3.: Absolute square of the transition amplitudes $|\langle\text{ref}|\,[\mathbf{Q}_{\text{TDA},\nu},\mathbf{H}_J]|\text{ref}\rangle|^2$ plotted vs. the excitation energy of $E_{\nu 0}$ (a) and Gaussian based strength functions (GSF) as function of the modulation frequency ω (b) for 20 boson on 20 sites of a homogeneous optical lattice at $U/J = 20$. Shown are the solutions of the SPH (-·-·-), S2PH (———), pTDA (······) and 4TDA (———). The lines in (a) are a guide to the eye.

In case of the SPH and S2PH the corresponding ground state $|E_0\rangle$ is used instead of the approximate reference state. Note, that the GSF provides just a rough estimate of the response of a system, since it has no knowledge of the proper modulation time τ. The GSF is therefore employed for a qualitative study of the model only.

In order to obtain the GSF of a system of 20 bosons on 20 sites we evaluate the excitation energies as well as the transition amplitudes via solution of the TDA equation. As interaction strength we choose $U/J = 20$, hence the system is in the Mott insulating phase.

Figure 3.3 (a) illustrates the absolute square of the non-vanishing transition amplitudes $|\langle\text{ref}|\,[\mathbf{Q}_{\text{TDA},\nu},\mathbf{H}_J]|\text{ref}\rangle|^2$ plotted versus the excitation energy $E_{\nu 0}$. Shown are the results for pTDA and 4TDA as well as SPH and S2PH as benchmark calculations. The non-vanishing values are represented by the symbols, the lines are just a guide to the eye. For each of the functions we obtain 10 non-vanishing transition amplitudes, which predict 10 states which are susceptible to an excitation by lattice modulations. Note, that the first Hubbard band of this system consists of 380 states, which means that 370 states lead to vanishing transition amplitudes.

Figure 3.3 (b) illustrates the strength functions $R_{\text{GSF}}(\omega)$ obtained via pTDA and 4TDA as well as SPH and S2PH with $\sigma/J = 0.5$. The reference function obtained via S2PH shows a resonance structure located in the range of the modulation frequencies $\omega/J = 14$ to 17, with a fine-structure of 7 visible peaks.

The strength function obtained with the pTDA in Fig. 3.3 (b) is in good agreement with the reference function. The shift between both functions in the modulation energy by about $1.5J$ corresponds to the shift in their energy spectra as discussed in the previous section in Fig. 3.2 (b).

The strength function obtained with the 4TDA in Fig. 3.3 (b) shows a much smaller width of ~ $5J$ in comparison to the other results. Therefore, the elementary Gaussians are squeezed to a smaller frequency interval and overlap stronger whereby the resonance shows an increased height and the fine-structure gets washed out. The smaller width is caused by the extra terms in the TDA matrix elements (3.32) when evaluated with the four-operator-type particle-hole operators as discussed in Sect. 3.5.1. We will address these deviations and its origin in Sect. 3.5.5 and appendix D.

The strength function obtained via SPH shows strong deviations from the benchmark calculation (S2PH). Although the SPH is closely related to the pTDA calculation, it shows a strong asymmetry due to an overestimation of the higher lying transition amplitudes as visible in Fig. 3.3 (a). Since the reference state of the pTDA and the SPH ground state are similar with an overlap of ~87% for this system, the origin of this deformation seems to result from the structure of the excited states. We will therefore investigate the excited states in Sect. 3.5.5.

Perturbative strength function (PSF)

A more realistic definition of the strength function can be obtained by evaluating the transition probabilities with time-dependent perturbation theory which we introduced in Sect. 2.2 and in appendix B). The perturbative strength function (PSF) reads

$$R_{\mathrm{PSF}}(\omega) = \sum_{\nu} E_{\nu}\, P^{(\tau)}_{0\to\nu}(\omega). \tag{3.52}$$

The transition probabilities are given by

$$P^{(\tau)}_{0\to\nu}(\omega) = \left| J V_0 F \left(\frac{d\ln J}{d\tilde{V}_0}\bigg|_{V_0} - \frac{d\ln U}{d\tilde{V}_0}\bigg|_{V_0} \right) \big\langle \mathrm{ref} \big| \left[\mathbf{Q}_{\mathrm{TDA},\nu}, \mathbf{H}_J \right] \big| \mathrm{ref} \big\rangle \right|^2 \frac{\sin^2[(\omega_{\nu 0} - \omega)\tau/2]}{(\omega_{\nu 0} - \omega)^2}, \tag{3.53}$$

with the frequencies $\hbar\omega_{\nu 0} = E_{\nu} - E_0$. In the limit of $\tau \to \infty$ equation (3.53) leads to Fermis *golden rule*. Equation (3.53) describes the probability to excite the state $|E_{\nu}\rangle$ from the reference state or the ground state, respectively, when modulating for the time τ with the frequency ω.

We evaluate the PSF using experimental parameters rather than the generic parameters J and U of the Hubbard model. The experimental parameters are based on a recent experiment by Stöferle *et al.* [39], where the response of an ultracold gas of ^{87}Rb was studied in a modulated optical lattice. The lattice wave length is $\lambda_1 = 826$ nm and the s-wave scattering length is given by $a_S = 100\, a_0$. As shown in chapter 1.2, these parameters enter the Bose-Hubbard model via the Hubbard parameters U and J, and the ratio U/J

is proportional to the amplitude of the laser s_1. The natural energy scale is given by the recoil energy,

$$E_{\mathrm{R},i} = \frac{\hbar^2 \lambda_i^2}{2m}, \tag{3.54}$$

with the atomic mass m of $^{87}\mathrm{Rb}$.

Figure 3.4 shows the U-resonance of a system of 20 bosons in a homogeneous optical lattice with 20 sites. The interaction strength is $U/J = 20$ in Hubbard parameters which corresponds to a laser amplitude of $s_1 = 8.2\ \mathrm{E_R}$. The lattice amplitude is modulated in time by 10 % ($F = 0.1$) for $\tau = 20$ ms.

Analogueously to the GSF we observe a narrow U-resonance for the 4TDA in Fig. 3.4 (a) located at the modulation frequency $\omega/2\pi = 2$ kHz.

In direct comparison to the reference function (S2PH) in Fig. 3.4 (d) the strength function obtained via pTDA (b) shows a centroid slightly above the modulation frequency $\omega/2\pi = 2$ kHz, which corresponds to the energy U. Moreover, it shows a more symmetric shape to the centroid frequency $\omega/2\pi = 2$ kHz.

As for the GSF, the strength function based on SPH in Fig. 3.4 (c) shows a strong deviation and underestimates the transition amplitudes on the lower end of the resonance and overestimates them for the high-frequency end.

In conclusion, we have seen that both versions of the strength function (GSF and PSF) based on the solutions of the pTDA are in good agreement to the benchmark calculation (S2PH), and by comparing the dimension of the model spaces — $D = 380$ for TDA and $D = 32871$ for S2PH — we achieve this with a vastly reduced numerical effort.

Level scheme

Figure 3.5 combines the level schemes of all four presented methods, the 4TDA and pTDA as well as SPH and S2PH. It shows again the matching energies of the 4TDA, pTDA, and SPH, which all are based on similar model spaces. The larger model space of the benchmark calculation (S2PH) offers much more flexibility for the variation and provides therefore lower energies.

Figure 3.5 also points out the excited states which correspond to non-vanishing transition amplitudes based on the matrix elements $\langle \mathrm{ref} | [\mathbf{Q}_{\mathrm{TDA},\nu}, \mathbf{H}_J] | \mathrm{ref} \rangle$. The states with non-vanishing transition amplitudes are emphasized in black and the relative strength of the transition is denoted by their horizontal length. Since the two solutions of the Schrödinger equation also provide the ground state, we can evaluate the transition amplitudes in two ways: We evaluate the transition matrix-element of the ground state and the excited state $\langle E_\nu | \mathbf{H}_J | E_0 \rangle$ and of the reference state and the excited state $\langle \mathrm{ref} | [\mathbf{Q}_{\mathrm{TDA},\nu}, \mathbf{H}_J] | \mathrm{ref} \rangle$.

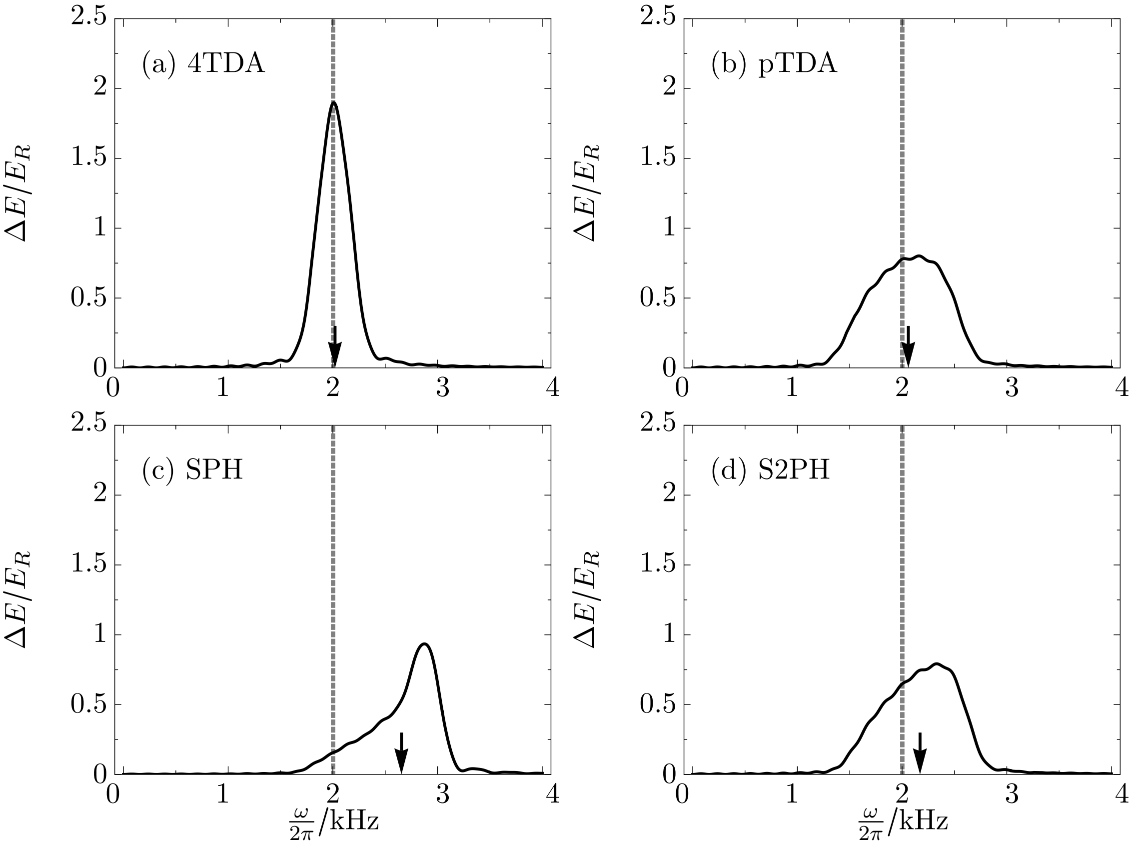

Fig. 3.4.: Strength functions $R_{\mathrm{PSF}}(\omega)$ based on the perturbative transition amplitude for a system of 20 bosons on 20 sites of a modulated homogeneous optical lattice. The interaction strength is $U/J = 20$ and the modulation time is $\tau = 20$ ms. The vertical gray line marks the modulation frequency corresponding to the energy U and the black arrow marks the centroid of the function.

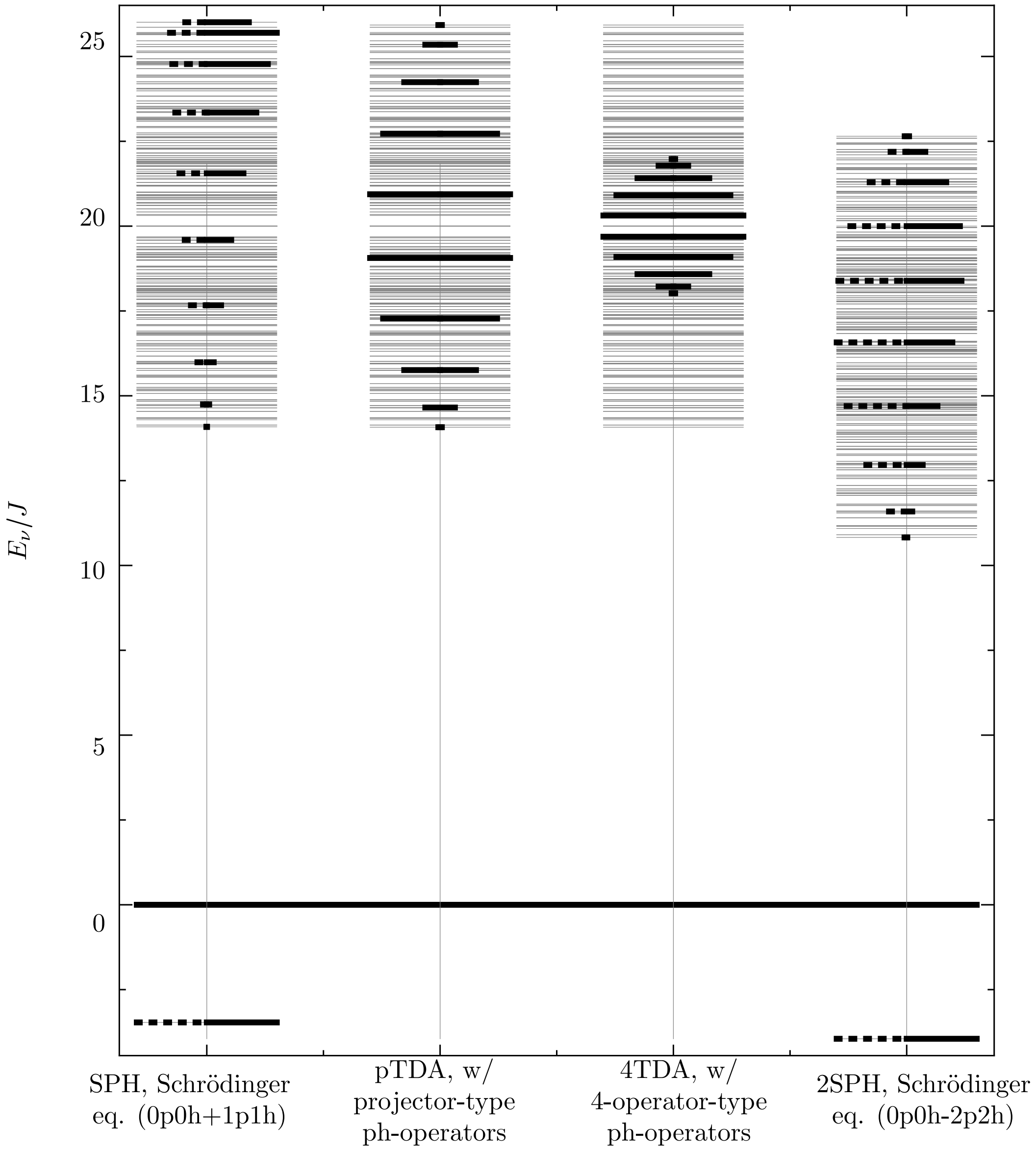

Fig. 3.5.: Energies of the first Hubbard band for 20 bosons on 20 sites of an homogeneous optical lattice at the interaction strength $U/J = 20$: SPH, pTDA and 4TDA and S2PH as reference. The grey lines mark the eigenenergies and the black ones point out eigenenergies of excited states which are connected to the ground state (respectively the reference state for TDA) via the hopping operator $\mathbf{H}_J$. The horizontal length of the black lines is scaled relative to the strength of the transition matrix elements $|\langle\text{ref}|\,[\mathbf{Q}_{\text{TDA},\nu},\mathbf{H}_J]|\text{ref}\rangle|^2$ (———) and $|\langle E_\nu|\,\mathbf{H}_J|E_0\rangle|^2$ (-------) with the ground state $|E_0\rangle$.

We include both versions in 3.5 by plotting the amplitudes based on the ground state from the center to the left hand side (dotted line) and those based on the reference state in the opposite direction (solid line).

For the SPH, the matrix elements calculated with the reference state $\left|\text{ref}\right\rangle$ are stronger than those calculated with the ground state $\left|E_0\right\rangle$ in the first column of Fig. 3.5. This can be explained by the looking at the structure of both states and how the tunneling operator $\mathbf{H}_J$ is acting on them:

The tunneling operator couples $\left|\text{ref}\right\rangle$ to the 1-particle-1-hole space, which is covered by the model space of the SPH. The ground state $\left|E_0\right\rangle$ obtained via SPH consists of the reference state by 87% and the remaining 13% are 1p1h-states. Since the tunneling operator couples 1p1h-states mostly[1] to the 2p2h-space, their contribution to the transition amplitude is lost.

The transition amplitudes of the pTDA and the 4TDA in the second and third columns of Fig. 3.5 reflect the structure of the strength functions discussed in the previous paragraph. For the 4TDA, the states with non-vanishing transition amplitude are squeezed to a small energy interval around $E/J = 20$, whereas for pTDA and for the solution of the Schrödinger equation these amplitudes are spread over the whole band. We investigate the structure of the excited states with non-vanishing transtion-amplitudes in the next section.

3.5.5. Structure of the excited states

All methods to obtain a response function, either via the energy transfer from the exact time-evolution (Sect. 2.4) or via the strength function from the particle-hole methods show a certain fine structure of the U-resonance. This structure is related to the system size: a lattice with 20 sites and bosons shows a 10-peak fine-structure, for 8 sites and bosons we see a 4-peak structure [63]. For homogeneous lattices with filling factor $N/I = 1$ and periodic boundary conditions we observe that the U-resonance is made up of $I/2$ peaks.

As discussed in Sect. 2.2, the U-resonance is based on excitations from the ground state into states in the first Hubbard band which lies at the energy U. The bulk contribution to the eigenstates of the first Hubbard band comes from $1p1h$- number states, which is obvious since these number states have the energy U (see Sect. 2.3).

The transition amplitude we employed in the linear response analysis in Sect. 2.3 and for the strength functions of the particle-hole methods in this chapter incorporate the knowledge on which states are susceptible to lattice amplitude modulation. These results correspond to time-evolution simulations based on the tDMRG method (time-dependent

---

[1] The tunneling operator $\mathbf{H}_J$ (1.13) has at most one term which de-excites the $1p1h$ excitation and produces, therefore, the state $\left|\text{ref}\right\rangle$, which is an element of the Hilbert space.

hopping distance	examples
next-neighbor	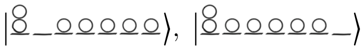
next-to-next-neighbor	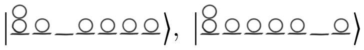
next-to-next-to-next-neighbor	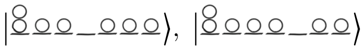

Tab. 3.3.: Classification of the $1p1h$ number states by the hopping distance when exciting the number state $\left|1,1,1,1,1,1\right\rangle$ in a system with 6 sites and 6 bosons and periodic boundary conditions.

density matrix renormalization group method [24] and exact time-evolution [26] (see also Sect. 2.4).

In the following, we will analyze the transition probability based on the matrix element $\left\langle E_0\right|\mathbf{H}_J\left|E_\nu\right\rangle$ to identify, which properties of a state make it susceptible to lattice modulations.

Since the main contribution to the ground state comes from the number state with one boson per site, we consider this state as the approximate ground state $\left|E_0\right\rangle$, and without loss of generality a 6-site lattice. The matrix element $T_{0\to\nu}$ reads

$$T_{0\to\nu} = \left\langle E_0\right|\mathbf{H}_J\left|E_\nu\right\rangle =$$ 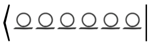 $$\mathbf{H}_J\left|E_\nu\right\rangle, \qquad (3.55)$$

where ν labels an excited state of the first band. The excited states can be expanded in the number state basis $\{\left|m\right\rangle\}$

$$T_{0\to\nu} =$$  $$\mathbf{H}_J\left(\sum_m c_m^{(\nu)}\left|m\right\rangle\right), \qquad (3.56)$$

with the expansion coefficients $c_m^{(\nu)}$. The right hand side of equation (3.56) can be rearranged as sum over matrix elements[2]

$$T_{0\to\nu} = \sum_m c_m^{(\nu)}$$ 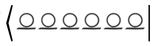 $$\mathbf{H}_J\left|m\right\rangle. \qquad (3.57)$$

Consequently, the only non-vanishing terms are those with number states $\left|m\right\rangle$, that are coupled to the state 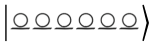 via the tunneling operator $\mathbf{H}_J$. Since the tunneling

---

[2] This reformulation is also very useful for the computation of the matrix element $\left\langle\nu\right|\mathbf{H}_J\left|\mathrm{ref}\right\rangle$. The matrix elements between the reference state and all number states $\left\langle m\right|\mathbf{H}_J\left|\mathrm{ref}\right\rangle$ can be pre-calculated and arranged as a vector. The transition matrix-element of a specific excited state is then given as the dot-product of this vector and the vector of the coefficients $c_m^{(\nu)}$.

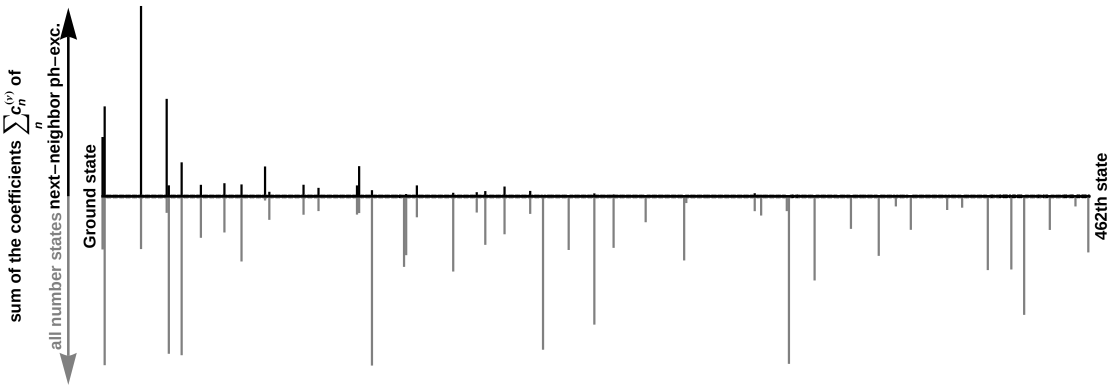

Fig. 3.6.: Sums over the number-basis expansion-coefficients $c_n^{(\nu)}$ of the 426 eigenstates of 6 bosons on a 6 site lattice at $U/J = 20$. Black lines refer to coefficients of next-neighbor particle-hole excited number-states of the state $\left|1,1,1,1,1,1\right\rangle$, only, and the gray ones show the sum over the coefficients of all number states. The black lines are scaled by a factor 3.

operator transfers a single particle to an adjacent site only, we can restrict the full number basis $\{\left|m\right\rangle\}$ to the subspace with next-neighbor particle-hole excited states (see Tab. 3.3). The sum in (3.57) collapses to

$$T_{0\to\nu} = \sum_{\substack{\{ij\}\\|i-j|=1}} c_{ij}^{(\nu)} \left\langle \underline{\circ}\,\underline{\circ}\,\underline{\circ}\,\underline{\circ}\,\underline{\circ}\,\underline{\circ}\right| \mathbf{H}_J \left|ij\right\rangle, \tag{3.58}$$

where the $\left|ij\right\rangle$ span the subspace of particle-hole excited number states of the full basis $\{\left|m\right\rangle\}$, where i and j are the indices of the site that are involved in the 1p1h-excitation. Please note, that the $c_{ij}^{(\nu)}$ are the subset of all coefficients $c_m^{(\nu)}$ corresponding to the 1p1h-states $\left|ij\right\rangle$. The matrix element

$$\left\langle \underline{\circ}\,\underline{\circ}\,\underline{\circ}\,\underline{\circ}\,\underline{\circ}\,\underline{\circ}\right| \mathbf{H}_J \left|ij\right\rangle = \sqrt{2}\,\delta_{1,|i-j|}, \tag{3.59}$$

acts like a delta-distribution, which picks only the coefficients of next-neighbor excited number-states in (3.57). The second requirement for a non-vanishing transition matrix-element $T_{0\to\nu}$ is, that the remaining coefficients sum up to a finite value,

$$T_{0\to\nu} \overset{(3.57)}{=} \sum_m c_m^{(\nu)} \left\langle \underline{\circ}\,\underline{\circ}\,\underline{\circ}\,\underline{\circ}\,\underline{\circ}\,\underline{\circ}\right| \mathbf{H}_J \left|m\right\rangle \overset{(3.59)}{=} \sum_{\{ij\}} c_{ij}^{(\nu)} \sqrt{2}\,\delta_{1,|i-j|} \neq 0. \tag{3.60}$$

Figure 3.6 illustrates that states $\left|E_\nu\right\rangle$ with a non-vanishing sum over the coefficients $\sum_m c_m^{(\nu)} \neq 0$, i.e., states where these coefficients add up coherently are a surprisingly rare

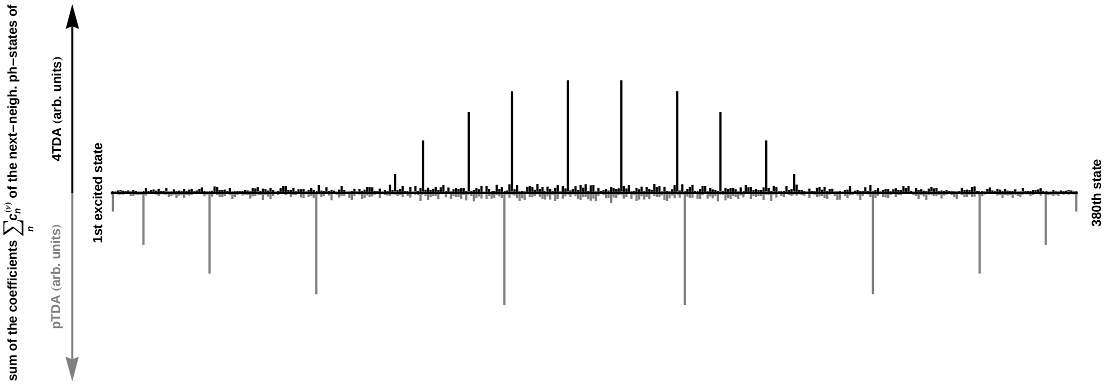

Fig. 3.7.: Relative distribution of the sums over the number-basis expansion-coefficients $c_m^{(\nu)}$ of only the next-neighbor excited 1-particle-1-hole states for the first Hubbard band of 20 bosons on a 20 site lattice at $U/J = 20$. Shown are the results for the 4TDA (black lines) and pTDA (gray lines).

phenomenon. In this system with $I = N = 6$ the coefficients of ~ 10 % of the eigenstates show finite sums only. In Fig. 3.6, the sum over the expansion coefficients $c_m^{(\nu)}$ of each state $|E_\nu\rangle$ is plotted. The black lines plotted upwards refer to the sum over coefficients of next-neighbor 1p1h-states number-states only, the gray lines plotted downwards represent the sum over all $c_m^{(\nu)}$ of the state $|E_\nu\rangle$.

The black lines in Fig. 3.6 indicate states $|E_\nu\rangle$ that are excited by lattice modulations. For instance, the first four black lines on the very left end of Fig. 3.6 are the sum of the coefficients of the ground state and the 3 of the 30 excited states in the first Hubbard band, which are sensitive to lattice modulations. Furthermore, the gray lines prove, that the vanishing of the sum over $c_m^{(\nu)}$ is not limited to the next-neighbor 1p1h excited-states but is also true for the sum over the coefficients of all number states.

Figure 3.7 compares the sums over 1p1h-states of 4TDA and pTDA in a similar manner. Shown are the sums over the coefficients of next-neighbor 1p1h excited-states of the first band only, i.e., the coefficients that are important for the transition amplitude $T_{0\to\nu}$. The black lines refer to the solutions of the 4TDA, and the gray lines to the pTDA. The envelopes of both distributions in Fig. 3.7 resemble the shape of the strength functions we discussed in Fig. 3.3 (b) and Figs. 3.4 (a) and (b) in Sect. 3.5.4.

Figure 3.7 clearly shows that the states responsible for the excitation by lattice modulations are located in a smaller interval in the middle of the first band for 4TDA. In contrast, these states are spread over the whole band for pTDA. From the studies of the strength functions in Sect. 3.5.4 we know that this is also true for the solutions of the Schrödinger equation (S2PH and SPH). Hence, the deviations in the matrix elements of the 4TDA as discussed in Sect. 3.5.1 have a severe impact on the structure of the eigenstates.

In summary, the energy eigenstates which are excited by lattice modulations as well as the ground state have in common that the expansion coefficients of next-neighbor excited number states sum up to a finite value. The coefficients of all other eigenstates sum up zero. This is a result of the sensitivity of the transition operator $\mathbf{H}_J$ to the phase of the states involved. Moreover, we have shown that the eigenstates for which these coefficients sum up to a finite value lie energetically in the center of the first band for the 4TDA. This causes the more narrow resonance shape one obtains in this approach. In contrast to the 4TDA, the pTDA-eigenstates with non-vanishing sums of the expansion coefficients are distributed over the whole band.

3.5.6. Dynamics of the superfluid to Mott-insulator transition

In this section, the transition between the superfluid and the Mott insulating phase is investigated within TDA. The aim is to characterize specific dynamical signatures of the system in each of the quantum phases and in the transition regime.

The quantum phase transition from the superfluid to the Mott insulating regime occurs for a one-dimensional system in the region between $U/J = 4$ to 5 [29]. In the following, we simulate a system of 20 bosons on 20 sites of a homogeneous lattice with periodic boundary conditions. In the range from $U/J = 2$ to 30 we evaluate the U-resonance using the Gaussian strength function (GSF) based on the solutions of pTDA and 4TDA. As width for the Gaussians in the GSF we have chosen $\sigma/J = 1.0$.

Figure 3.8 (upper panel) shows the evolution of the U-resonance obtained via the pTDA. Each of the strength functions is plotted as function of the modulation frequency ω given in units of the corresponding interaction strength U. In how far the representation in units of U reflects the characteristics assumed in the experiment is discussed in Sect. 3.5.7.

One observes a rather strong and sharp resonance for strong interactions which gets broader and weaker towards the superfluid regime located at $\omega = U$. For interactions closer to the superfluid regime at $U/J \leq 10$, the centroid of the resonance shifts clearly to higher modulation frequencies as illustrated by the black line in the $\omega - U$-plane.

The maximum of the response drops at most linearly with decreasing interaction strength and the width[3] of the response broadens simultaneously, as denoted by the gray area in the $\omega - U$-plane. These features are in perfect agreement with the linear response analysis in the full space for a small system with 6 bosons (Sect. 2.2) as well as the explicit time-evolution in importance truncated model spaces in Sect. 2.4.2.

The strength function obtained via 4TDA in the lower panel of Fig. 3.8 shows the same

---

[3] We use the variance of the response function as its width via $\Delta\omega^2 = \int d\omega\omega^2 R(\omega) - (\int d\omega\omega R(\omega))^2$.

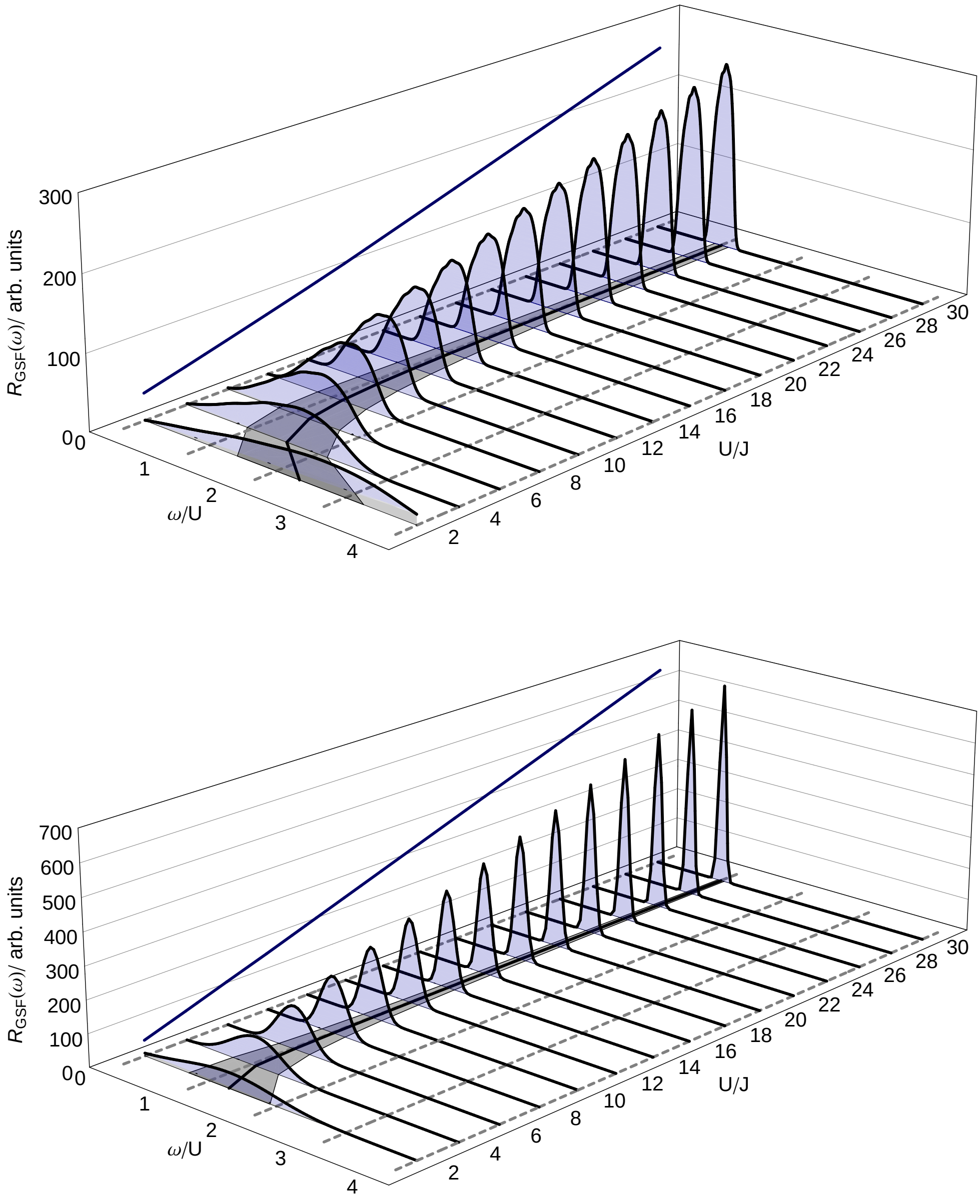

Fig. 3.8.: Evolution of the U-resonance from the superfluid to the strongly interacting phase. Shown are the results for a homogeneous lattice with $I = N = 20$. The upper panel shows the Gaussian strength function with $\sigma/J = 1.0$ obtained via the pTDA, the lower panel those of the 4TDA. The black line and the gray-shaded area in the U-ω plane illustrate the evolution of the centroid and the width of the resonance. The line in the U-R_{GSF} plane depicts the evolution of the maxima of the strength function.

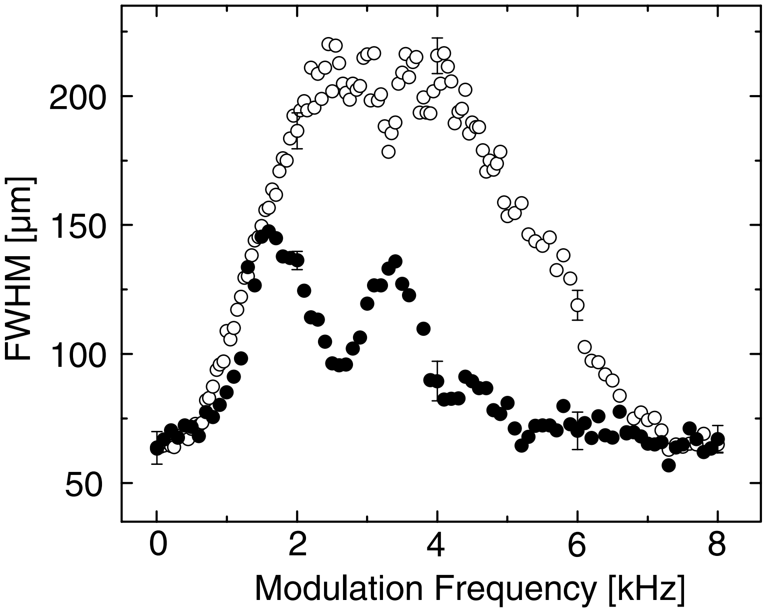

Fig. 3.9.: Experimental spectroscopy of the superfluid phase (open circles, $U/J \approx 2.3$) and the Mott phase (solid circles, $U/J \approx 14$) of bosons in a 1D optical lattice by Stöferle *et al.* [39]. Measured is the width (full width half maximum, FWHM) of the central momentum peak of the interference pattern as function of the modulation frequency of the lattice, which corresponds to the energy transferred into the system. The plot is taken from [39].

qualitative behavior as for pTDA. The response functions are narrower an show an increased height. The shift of the centroid from the $\omega = U$-line to higher frequencies is not as distinct as for the pTDA.

3.5.7. Generic Hubbard parameters vs. experimental parameters

Modulation time & energy transfer

In the previous section, we have illustrated the U-resonance for several interaction strengths in the strongly interacting and superfluid regime. The studies in the previous section were completely based on the generic Hubbard parameters, i.e., energies and frequencies, respectively, were given in units of U and J.

In these simulations we have observed a decline of the strength of the resonances, i.e., the height of the peaks, with a decrease of the interaction strength. However, we know from the modulation experiments by Stöferle et al. [39] that the response is broad and strong in the superfluid regime whereas it is sharp and weaker in the Mott regime (cf. Fig. 3.9).

In the experiment a Bose gas in a one-dimensional is probed by lattice modulations.

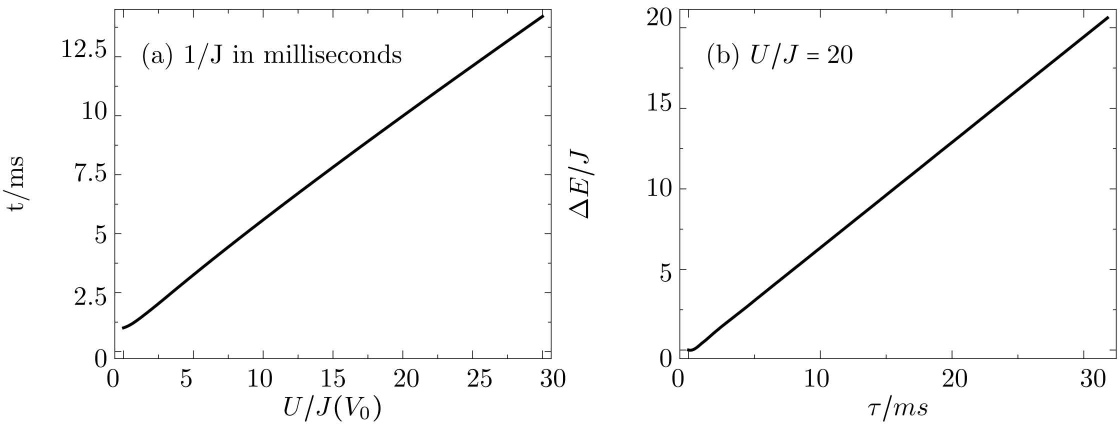

Fig. 3.10.: Panel (a) illustrates schematically the translation of the time unit $1/J$ in generic Hubbard parameters into milliseconds as function of the interaction strength $U/J(V_0)$, which is itself a function of the lattice depth V_0. Panel (b) shows the averaged energy transfer of the U-resonance as function of the modulation time for a system of 10 bosons on 10 sites at $U/J = 20$. The results obtained via solving the Schrödinger equation in up to 2p2h-space. For averaging of the energy transfer we integrated over the whole U-resonance (frequency interval $\omega/2\pi = 0 - 4\,\text{kHz}$).

The response is measured via the broadening of the central peak of the interference pattern, which is identified with an energy transfer into the gas. Figure 3.9 shows the width of the central momentum peak as function of the modulation frequency from [39].

The reason for this discrepancy is the non-trivial relation between the generic Hubbard parameters U and J and the experimental ones. Figure 3.10 (a) illustrates the translation of the time $1/J$ to milliseconds. It turns out, that the translation from $1/J$ to milliseconds depends on the lattice depth V_0, which is expressed in the ration U/J on the x-axis in Fig. 3.10 (a). Hence, a fixed modulation time $\tau J = 20$, which we considered in previous calculations, means, that we modulate for longer real time at stronger interactions.

Since the energy transfer ΔE scales linearly with the modulation time τ for the strength functions [cf. Fig. 3.10 (b)], the response seems stronger for stronger interactions, i.e., deeper lattices, in Fig. 3.8.

Resonance widths

In the Sect. 3.5.6, we have presented the evolution of the U-resonance when the interaction strength is varied between the Mott insulating and the superfluid phase. We have seen, that the U-resonance gets broader for weaker interactions when plotted as function

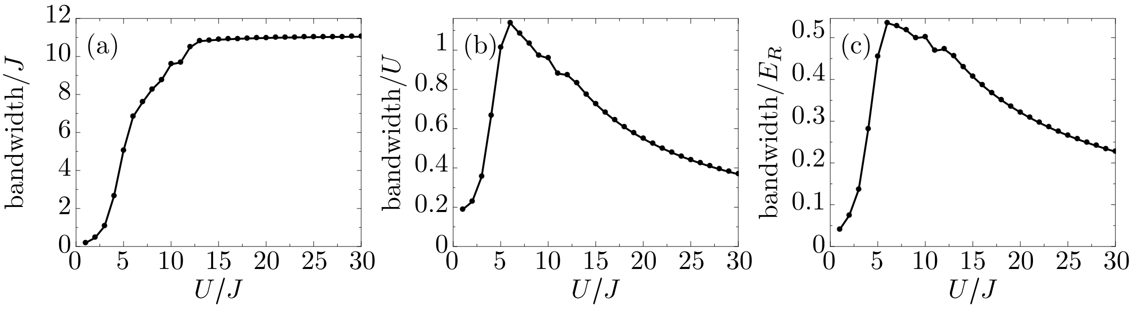

Fig. 3.11.: Energetic width of the first Hubbard band of a system of 8 bosons on 8 sites as function of the interaction strength U/J. As the bandwidth the energy difference of the first and the last states in the band are taken and plotted in units of J (a), U (b), and the recoil energy E_r (c). The recoil energy is based on the parameters of Rubidium-87 in a lattice made up with a laser of the wavelength 826 nm [39].

of the modulation frequency in units of U.

The foremost reason to present the strength functions in Fig. 3.8 as function of the modulation frequency ω in units of U is that we are able to study the evolution of the centroid and the width of the response. One might ask, wether the representation of ω in units of U reflects the true characteristics of centroid and width as they appear in experiment.

Since the width of the first Hubbard band is a good estimate for the width of the resonance, we plot it for an exactly solved system of 8 bosons on 8 sites in Fig. 3.11 as function of the interaction strength, represented in different units of the energy. Figure 3.11 (a) shows the bandwidth in units of J with a strong positive slope in the superfluid up to $U/J \approx 12$. Starting from there, the bandwidth shows a constant increase towards stronger interactions.

In units of U as depicted in Fig. 3.11 (b), the bandwidth shows a stronger positive slope in the superfluid up until $U/J \approx 5.5$. Starting from there, it drops slowly to zero, since the states in the first band are energetically degenerated for $U/J \to \infty$ (cf. Fig. 1.3 (b)).

The representation of the bandwidth in units of the recoil energy E_R shows qualitatively the same behavior as the plot in units of U in Fig. 3.11 (c). It shows a steep positive slope in the superfluid regime and starting from $U/J \approx 5.5$ a slow decline.

In conclusion, the representation of the strength function as function of the modulation frequency ω in units of U as in Fig. 3.8 reflects qualitatively the behavior as assumed for a natural frequency unit Hz.

U-resonance evolution from an experimental point of view

In this paragraph we study the U-resonance of a system with $I = N = 50$ in the parameter region of the experiment by Stöferle *et al.* [39]. For the translation of the Hubbard parameters into the experimental control parameters we assume a gas of Rubidium-87 and a lattice of the wavelength $\lambda_1 = 826$ nm. The atomic mass and the wavelength λ_1 define an energy scale via the recoil energy

$$E_{\mathrm{R},1} = \frac{\hbar^2 k_1^2}{2m}, \tag{3.61}$$

with $k_1 = 2\pi/\lambda_1$. Figures 3.12 (pTDA) and 3.13 (4TDA) show the energy transfer as function of the modulation frequency of a homogeneous system with $N = I = 50$. The energy transfer ΔE is evaluated using the perturbative strength function (PSF) with the time $\tau = 20$ ms and the modulation amplitude $F = 0.1$.

For both versions of the TDA we illustrate the energy transfer in the region of the U-resonance for interaction strengths from $U/J = 30$ in the strongly interacting regime in Figs. 3.12 and 3.13 (a) to $U/J = 2$ in the superfluid phase in (o). The modulation frequency corresponding to the energy U is marked by the gray vertical line and the centroid of the resonance is displayed by the black arrow.

In the strongly interacting regime for $U/J = 30$ we observe the U-resonance at 2.1 kHz of the width 1.7 kHz in Fig. for the pTDA in Fig. 3.12 (a). The centroid of the resonance is slightly above 2.1 kHz, hence, it is close to the modulation frequency that corresponds to the energy U. For decreasing interaction strength the centroid moves slowly away from $\omega = U$-line towards higher frequencies as shown in the sequence from Fig. 3.12 (b) to (m) ($U/J = 28$ to 6).

Along with the decreasing interaction strength the width of the resonance increases from 1.7 kHz for $U/J = 28$ to 2.2 kHz for $U/J = 12$ and the overall strength of the resonance increases continuously. Both effects are in perfect agreement with the experimental findings of Stöferle *et al.* which are shown in Fig. 3.9 and 1.9.

For weaker interactions ($U/J = 6$ and lower) we observe a decreasing overall strength of the resonance in contrast to the experiment [cf. Fig. 3.9]. This can be explained when comparing the structure of the true ground state for small U/J with the reference state: for small U/J, the particles are strongly delocalized. The number basis, however, is spanned by product states of localized Wannier states. To cope with the strong delocalization of the particles, the ground state has to include strong correlation to all basis states. It is, therefore, delicate to employ our simple reference state as ground-state approximation in this regime.The importance of the correlations is indicated by the maximum coefficient of the number basis expansion of the ground state $c^2_{\max}$ in Fig. 1.4 (a).

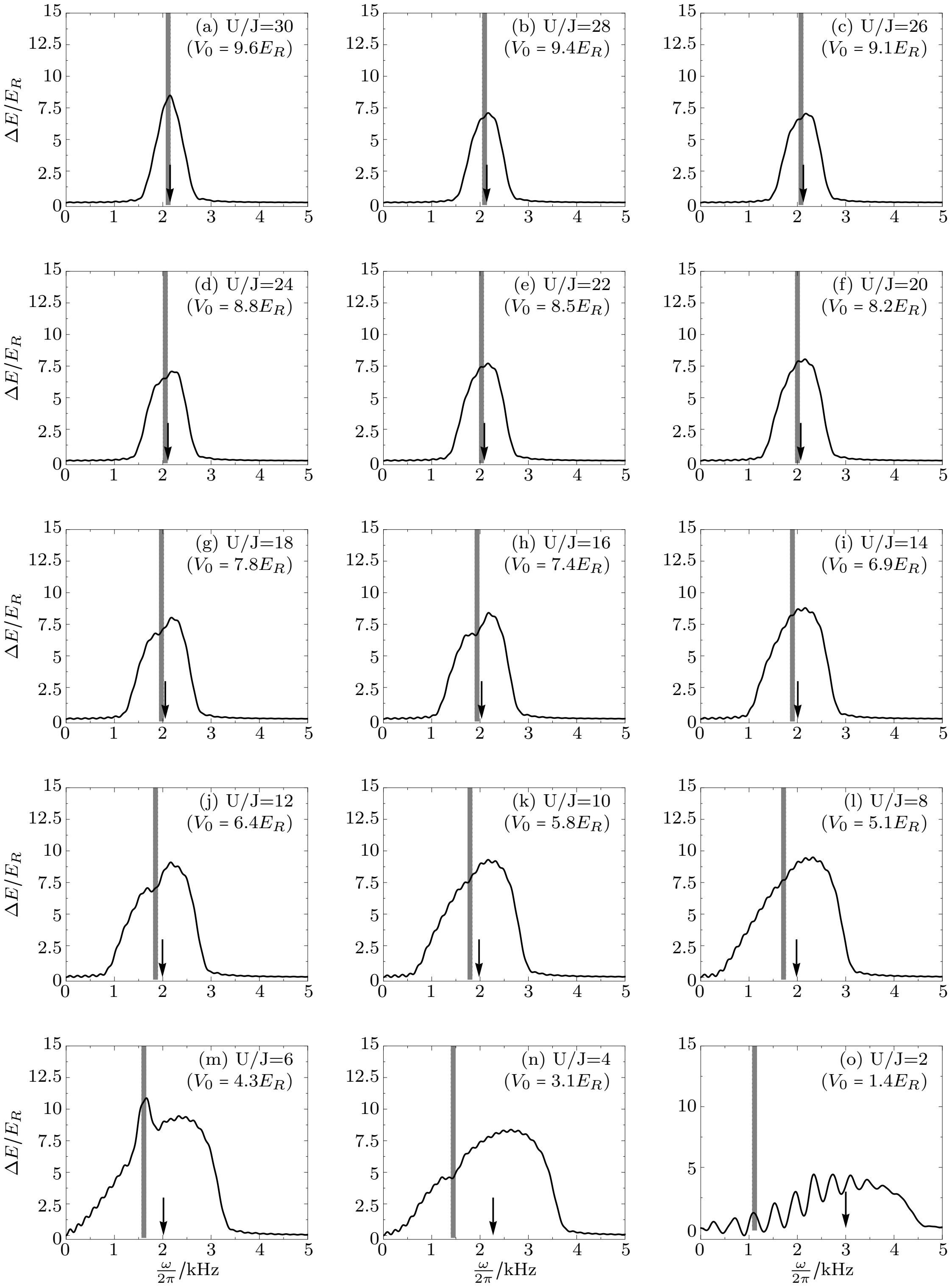

Fig. 3.12.: Energy transfer of a system of 50 bosons on 50 sites obtained via linear response based on time-dependent perturbation theory and the projector-type TDA. The modulation time is fixed to τ = 20ms. The vertical gray lines denote the modulation frequency corresponding to the energy U and the black arrow points to the resonances centroid.

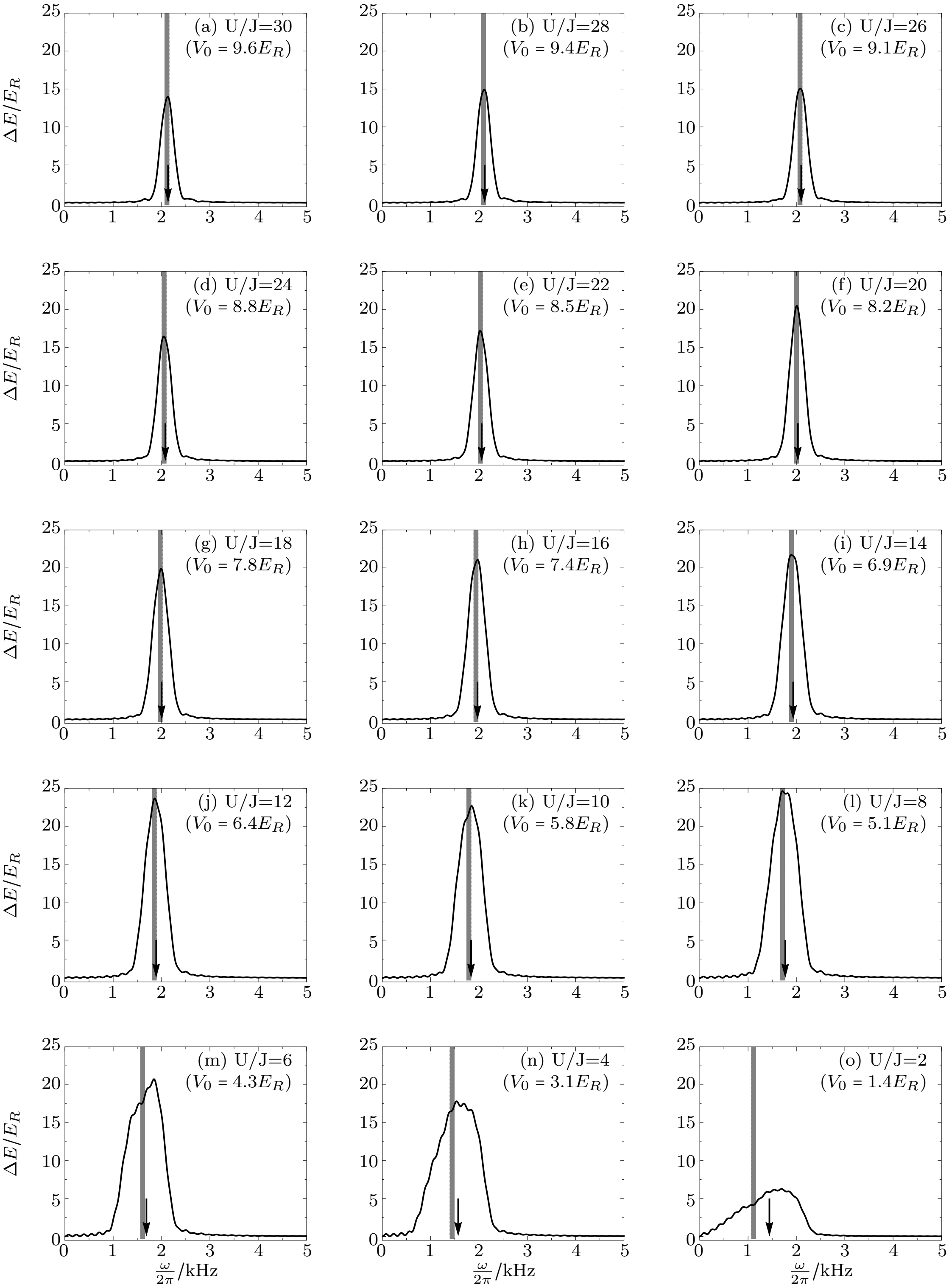

Fig. 3.13.: Energy transfer of a system of 50 bosons on 50 sites obtained via linear response based on time-dependent perturbation theory and the four-operator type TDA. The modulation time is fixed to τ = 20ms. The vertical gray lines denote the modulation frequency corresponding to the energy U and the black arrow points to the resonances centroid.

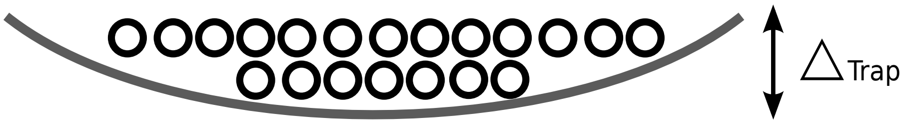

Fig. 3.14.: Schematic of the wedding-cake structure of the ground state in a strongly interacting lattice system with harmonic confinement.

However, the TDA was designed for the strongly interacting regime from the outset, hence, deviations at weak interactions are expected.

The 4TDA results shown in Fig. 3.13 match perfectly those of the pTDA on the qualitative level. As discussed earlier in this chapter, the strength functions obtained via the 4TDA show narrower resonances and along with this an increased height. The width (variance of the response function) of the resonances is 0.75 kHz for $U/J = 30$ in Fig. 3.13 (a), which is about 44% of the according pTDA strength function in Fig. 3.12 (a).

In correspondence to the pTDA we observe an increase of the overall resonance strength for decreasing interaction strength and a shift of the centroid to higher frequencies in Figs. 3.13 (b) to (l). Finally, starting from $U/J = 8$, we also observe a decrease of the resonance strength in the weakly interacting regime.

In conclusion, the TDA enables us to reproduce the experimental findings by Stöferle *et al.* [39] rather well. Additionally, the TDAs allow these results with minimal numerical effort — the computation of the strength functions presented in Fig. 3.12 takes only a few hours on a standard laptop computer, including the calculation of the TDA matrix elements. The limitation is the solution of the TDA eigenproblem. Though the eigenproblem is sparse since only next neighbor hopping is involved [cf. equation (3.32)], we require all eigenvalues and eigenvectors. Hence, we cannot resort on Lanzcos-type eigenproblem solvers, which are suitable for a few eigenvalues and eigenvectors only.

3.5.8. Effects of a harmonic trap

In the previous paragraph we have shown that the TDA can reproduce the U-resonance as observed in experiments [36,39]. However, in addition to the U-peak one observes also a $2U$-resonance peak in experiments [cf. Figs. 3.9 and 1.9], which is not visible in our simulations. The reason is that the $2U$-resonance is an effect of excitations between a singly and a doubly occupied site, as they appear in a harmonically trapped system.

Analogous to the discussion in Sect. 1.3.3 for the superlattice, the harmonic profile enters the Bose-Hubbard Hamiltonian via the on-site potential term,

$$\mathbf{H} = J\sum_{i=1}^{I}\left(\mathbf{a}_i^\dagger \mathbf{a}_{i+1} + \mathbf{a}_{i+1}^\dagger \mathbf{a}_i\right) + \frac{U}{2}\sum_{i=1}^{I}\mathbf{n}_i(\mathbf{n}_i - 1) + \sum_{i=1}^{I}\epsilon_i \mathbf{n}_i, \tag{3.62}$$

in which the ϵ_i reflect the on-site energies. Figure 3.14 illustrates this situation.The on-site potential is increasing from the center of the lattice towards the sites at the boundaries. Hence, if the on-site potential of the outer sites overcomes the interaction energy in the center of the lattice, it is energetically favorable to have a doubly occupied site at the center. The ground state of the system is thus dominated by a number state with a *wedding-cake* structure as depicted in Fig. 3.14.

The existence of two different *Mott-domains*, i.e. insulating regions with single and double occupations, has impact on the response of the system to small amplitude modulations. We consider a simple 8-site state in a trapped system as approximation to the ground state,

$$\big|\text{ref}\big\rangle = \big|\_\,\circ\,\circ\,\overset{\circ}{\circ}\,\overset{\circ}{\circ}\,\circ\,\circ\,\_\big\rangle.$$

Besides the particle-hole excitations between sites of equal occupation with the excitation energy U, also excitation at the borders of the domains occur. Next-neighbor particle-hole excitations at the boundaries of the domains require the energy $2U$, which explains the secondary peak in the experiments,

$$\big\langle\_\,\circ\,\_\,\overset{\circ}{\overset{\circ}{\circ}}\,\overset{\circ}{\circ}\,\circ\,\circ\,\_\big|\mathbf{H}\big|\_\,\circ\,\_\,\overset{\circ}{\overset{\circ}{\circ}}\,\overset{\circ}{\circ}\,\circ\,\circ\,\_\big\rangle - \big\langle\_\,\circ\,\circ\,\overset{\circ}{\circ}\,\overset{\circ}{\circ}\,\circ\,\circ\,\_\big|\mathbf{H}\big|\_\,\circ\,\circ\,\overset{\circ}{\circ}\,\overset{\circ}{\circ}\,\circ\,\circ\,\_\big\rangle = 4U - 2U = 2U.$$

The on-site potential difference between neighboring sites is small compared to the interaction strength, hence, it is neglected in the calculations above.

Since the observation of the $2U$-resonance requires different Mott-domains in the system, it is taken as a measure for the incommensurability of the filling factor [28]. In the following, we investigate a system of 20 sites and filling factors ranging from $N/I = 1$ to 1.5 in a harmonically trapped system. We simulate the experimental setup of Fallani *et al.* [36] with a lattice depth of $V_0 = 16E_R$ ($U/J \approx 134$) and a trapping frequency of 75 Hz. The trapping potential is realized via the on-site potential energies ϵ_i with a maximum potential difference of $\max(\{\epsilon_i\}) - \min(\{\epsilon_i\}) = 3$ J.

Figure 3.15 shows the perturbative strength functions obtained via the pTDA for a lattice amplitude modulation with $F = 0.1$. The energy transfer ΔE is obtained via the perturbative strength function (PSF) with $\tau = 20$ ms. Since the trapping potential is very weak, the system with $N/I = 1$ in (a) has only one Mott domain and thus shows the U-resonance only.

With two additional particles we observe the emergence of a weak $2U$-resonance in Fig. 3.15 (b). A further increase of the filling factor up to $N/I = 1.5$ does not change the strength of the $2U$ resonance. This is not surprising, since $2U$-resonance is an effect that relies on the boundary between the domains. Since in an one-dimensional lattice the boundary between the domains is represented by two sites only, it is independent of the number of particles in the lattice. Hence, there will not be any additional possibilities for

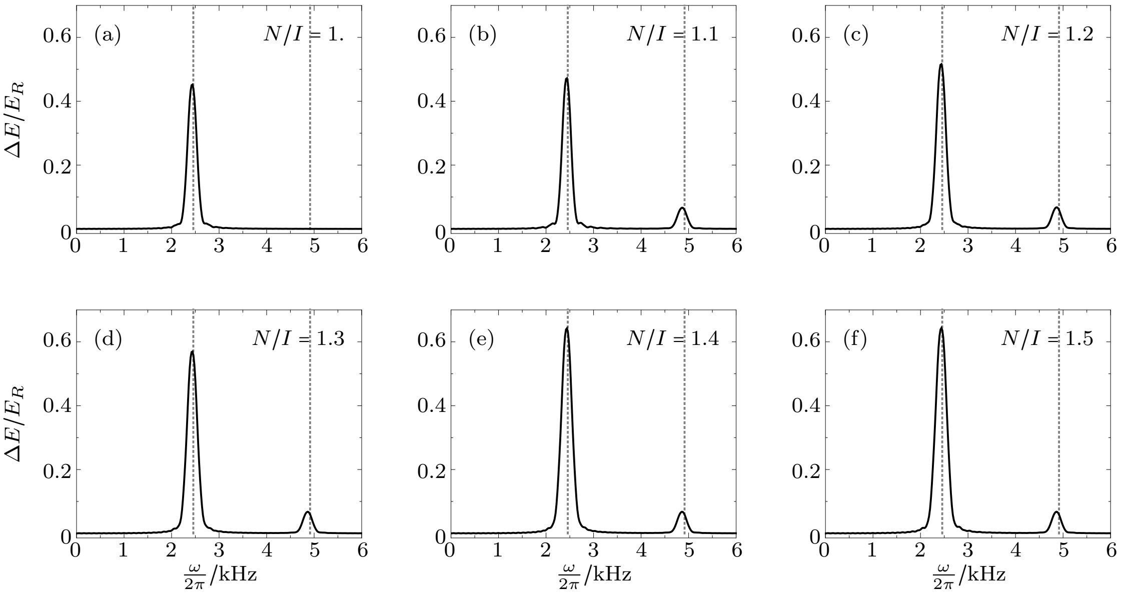

Fig. 3.15.: Energy transfer of a 20 site system with a harmonic trapping potential of the frequency $\omega_{\text{trap}}/(2\pi) = 75$ Hz at a lattice depth of $V_0 = 16\ E_{\text{R}}$ for ^{87}Rb (equivalent to $U/J = 134$ and $\Delta/J = 3$ at the boundaries). The sequence of plots from (a) to (f) shows the U-resonance for several filling factors.

$2U$-excitations.

However, we observe an increasing strength of the U-resonance with increasing filling factor in the sequence of strength functions in Fig. 3.15. This can be explained by looking at the tunneling matrix-elements which are an ingredient to the strength function. We consider two types of excitation:

1. A system with the reference state $\left|\underline{\circ}\,\underline{\circ}\,\underline{\circ}\,\underline{\circ}\right\rangle$, which is excited to $\left|\underline{\circ}\,\underline{}\,\underline{\substack{\circ\\\circ}}\,\underline{\circ}\right\rangle$. The hopping matrix-element reads

$$\left\langle\underline{\circ}\,\underline{}\,\underline{\substack{\circ\\\circ}}\,\underline{\circ}\right|\mathbf{H}_J\left|\underline{\circ}\,\underline{\circ}\,\underline{\circ}\,\underline{\circ}\right\rangle = \left\langle\underline{\circ}\,\underline{}\,\underline{\substack{\circ\\\circ}}\,\underline{\circ}\right|\mathbf{a}_3^\dagger\mathbf{a}_2\left|\underline{\circ}\,\underline{\circ}\,\underline{\circ}\,\underline{\circ}\right\rangle = \sqrt{2}. \tag{3.63}$$

2. A system with the reference state $\left|\underline{\substack{\circ\\\circ}}\,\underline{\substack{\circ\\\circ}}\,\underline{\substack{\circ\\\circ}}\,\underline{\substack{\circ\\\circ}}\right\rangle$, which is excited to $\left|\underline{\substack{\circ\\\circ}}\,\underline{\circ}\,\underline{\substack{\circ\\\circ\\\circ}}\,\underline{\substack{\circ\\\circ}}\right\rangle$. In this case, the hopping matrix-element reads

$$\left\langle\underline{\substack{\circ\\\circ}}\,\underline{\circ}\,\underline{\substack{\circ\\\circ\\\circ}}\,\underline{\substack{\circ\\\circ}}\right|\mathbf{H}_J\left|\underline{\substack{\circ\\\circ}}\,\underline{\substack{\circ\\\circ}}\,\underline{\substack{\circ\\\circ}}\,\underline{\substack{\circ\\\circ}}\right\rangle = \left\langle\underline{\substack{\circ\\\circ}}\,\underline{\circ}\,\underline{\substack{\circ\\\circ\\\circ}}\,\underline{\substack{\circ\\\circ}}\right|\mathbf{a}_3^\dagger\mathbf{a}_2\left|\underline{\substack{\circ\\\circ}}\,\underline{\substack{\circ\\\circ}}\,\underline{\substack{\circ\\\circ}}\,\underline{\substack{\circ\\\circ}}\right\rangle = \sqrt{6}. \tag{3.64}$$

This shows, that although the excitation requires the same energy, it results in an increased strength for the multiple occupied sites in an incommensurate system. This

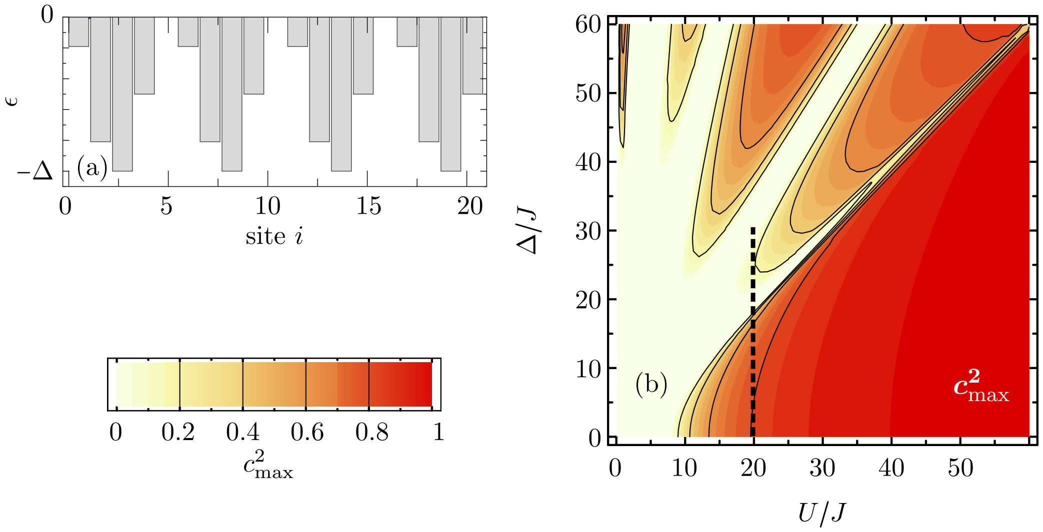

Fig. 3.16.: On-site potential energies ϵ_i of the period-five superlattice with 20 sites (a) and the phase diagram of a system with $I = N = 10$ (b). The black dotted line represents a route from the homogeneous Mott insulator phase to the Bose-glass phase at $U/J = 20$.

means for our simulations in Fig. 3.15, that the larger fraction of doubly occupied sites for larger filling factors is responsible for the stronger U-resonance.

In conclusion, we have shown that the TDA can reproduce the $2U$-resonance that appears in experiments due to multiple Mott domains. However, the strength of the $2U$-resonance is underestimated as compared to the experimental findings.

3.5.9. U-resonance in a two-color superlattice

In this section, we come back to systems in a two-color superlattice, which we also investigated with the explicit time-evolution in Sect. 2.5. As discussed in Sect. 1.3.3, the superlattice enters the Bose-Hubbard Hamiltonian (3.62) via an on-site potential term, in which the ϵ_i reflect the lattice topology. The values of the on-site potential energies are depicted in Fig. 3.16 (a).

In the following, we present the strength functions of a system with $I = N = 20$ in a two-color superlattice for several superlattice amplitudes Δ. We employ the Gaussian strength functions (GSF) based on the solutions of the pTDA. The interaction strength is fixed to $U/J = 20$, and Fig. 3.16 (b) illustrates the route we take through the phase-diagram. Note, that Fig. 3.16 (b) is the phase diagram of a system with $I = N = 10$.

Figure 3.17 shows the evolution of the U-resonance along the route depicted by the

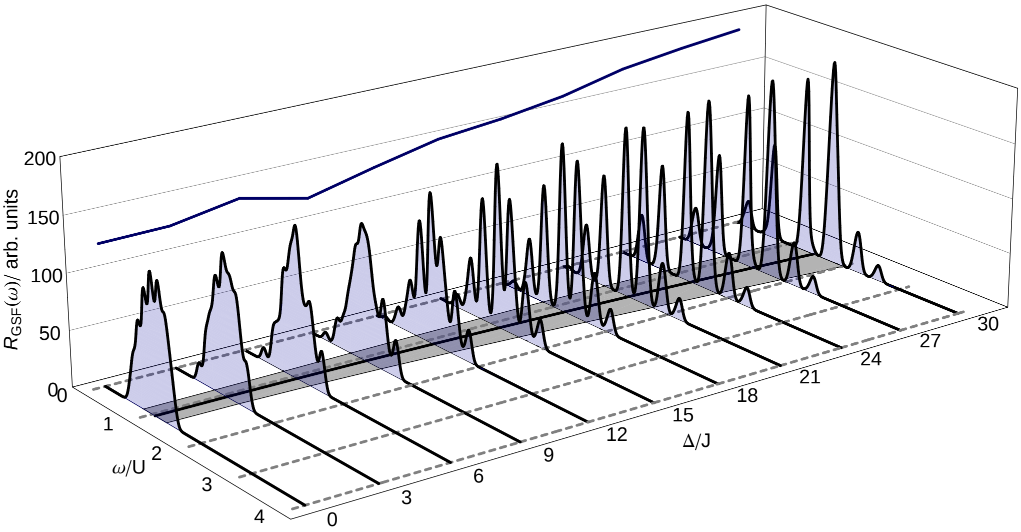

Fig. 3.17.: U-resonance of a system with $I = N = 20$ at $U/J = 20$ for several superlattice modulation amplitudes Δ. The resonance is represented by the gaussian strength function (GSF) with $\sigma/J = 1.0\ J$, based on the solution of the pTDA. The gray area and the black line in the $\omega - U$-plane illustrate the evolution of the width and the centroid of the strength function, the line in the U-R_{GSF} plane depicts the evolution of the maxima of the strength function.

dotted line in Fig. 3.16 (b). For $\Delta = 0$ we observe the resonance shape of the homogeneous system. As the superlattice amplitude is increased the U-resonance broadens and develops a stronger fragmentation starting from $\Delta/J = 9$. At the same time, the centroid of the strength function shifts to higher modulation frequencies as illustrated by the black line in the $\omega - U$-plane of Fig. 3.17.

With a further increase of the superlattice amplitude towards $\Delta = U$ low-lying strength emerges — at this point one leaves the homogeneous Mott-insulator phase and enters the Bose-glass phase. Now the response ranges down to $\omega = 0$, which reflects the loss of the gapped excitation spectrum. In conclusion, the qualitative study of the transition from the homogeneous Mott-insulator regime is in good agreement with the experimental observations by Fallani *et al.*, who reported the broadening of the resonance structure in a superlattice [36].

Superlattice based on experimental control parameters

In this final section, we want to simulate the experiment by Fallani *et al.* with a gas of Rubidium-87 using the experimental control parameters [36]. The depth of the primary

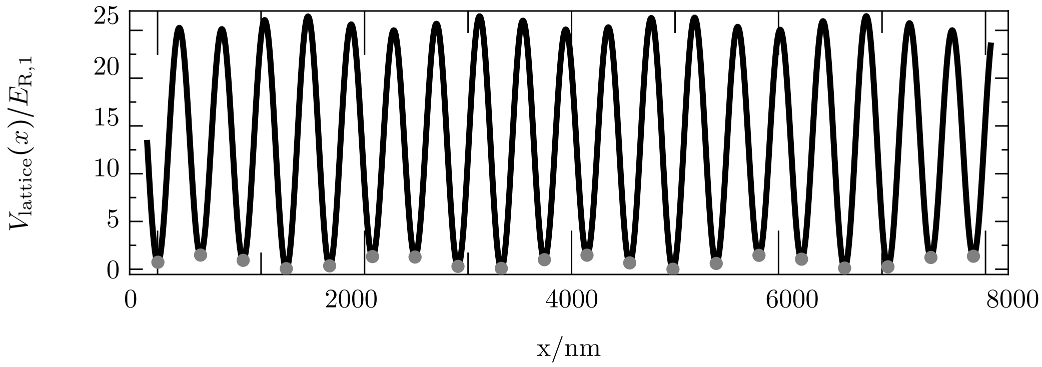

Fig. 3.18.: Superlattice structure adopted for the simulations from the experiment by Fallani et al. [36] with Rubidium-87. The primary lattice is generated by a laser with the wavelength $\lambda_1 = 830$ nm and fixed at a amplitude $V_1 = 25\ E_{\text{R}}$. The superposition of the weaker secondary laser ($\lambda_2 = 1076$ nm) leads to the spatial modulation. The intensity of the secondary laser can be varied in order to adjust the strength of the superlattice amplitude. The plot shows the situation for $V_2 = 2.5\ E_{\text{R}}$.

lattice is $V_1 = 16\ E_{\text{R},1}$ ($\sim U/J = 134$) with a wave length of $\lambda_1 = 830$ nm. The secondary laser, which accounts for the spatial modulation, has a wavelength of $\lambda_2 = 1076$ nm and produces an adjustable depth of $V_2 = 0 - 2.5\ E_{\text{R},2}$ ($\Delta/J = 0 \sim 279$). Figure 3.18 illustrates the modulated superlattice, in which the gray dots in the minima represent the lattice sites.

Based on the solutions of the pTDA we evaluate the perturbative strength function (PSF) with $\tau = 30$ ms for several depths of the secondary laser V_2. In contrast to the underlying experiment [36] we use a temporal modulation amplitude of $F = 0.1$ instead of $F = 0.3$, in order stay within with the linear response regime, which the perturbative strength function relies on.

In Fig. 3.19 (a) the U-resonance of the homogeneous lattice with $V_2 = 0$ is depicted. The vertical gray line marks the modulation frequency corresponding to the energy U and the black arrow points to the centroid of the strength function. Already for weak V_2 we observe a significant broadening of the resonance at $V_2 = 0.25\ E_{\text{R},2}$ [Fig. 3.19 (b)] and $V_2 = 0.25\ E_{\text{R},2}$ (c) and a shift of the centroid of the resonance towards higher modulation frequencies. At the same time, the height of the resonance structure drops continuously.

Starting from the transition into the Bose-glass phase for $U > \Delta$ in Figs. 3.19 at $V_2 \approx 134\ E_{\text{R},2}$ (f) the response reaches down to low modulation frequencies $\omega/(2\pi)$, which indicates the vanishing of the energy gap in the excitation spectrum. By entering the Bose-glass phase from the Mott regime, we also have to modify the reference state $|\text{ref}\rangle$

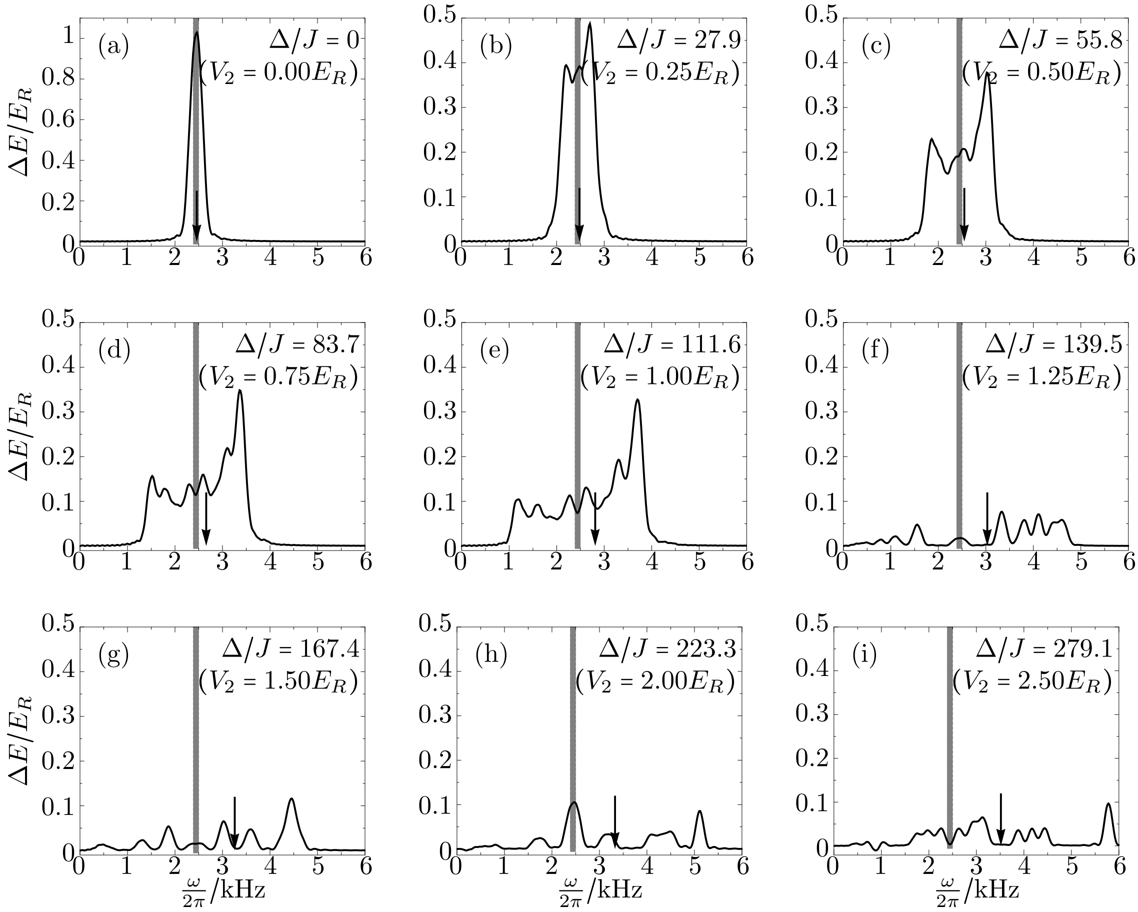

Fig. 3.19.: Energy transfer of a system of 20 bosons on 20 sites in a two-color superlattice according to the experiment [36]. The primary lattice depth is $V_1 = 16\ E_{\mathrm{R},1}$ ($U/J \approx 134$), the secondary varies from $V_2 = 0 - 2.5\ E_{\mathrm{R},2}$ ($\Delta/J = 0 \sim 279$). The modulation time is 30 ms and the modulation amplitude is $F = 0.1$. The vertical gray line marks the frequency according to the energy U and the arrow points to the centroid of the resonance structure. Note the different scale of the energy axis in(a).

of the TDA. In the Mott phase, the ground state is system is dominated by the number state with exactly one particle per site, which we then take as the reference state in this regime. However, since the on-site potential energies of the superlattice and the interaction strength are of comparable magnitude in the Bose-glass phase, it is energetically more favorable to occupy sites of lower on-site potential doubly. In the Bose-glass phase we, therefore, set the reference state to the most probable number state, which complies with the current superlattice. The reference states are switched for $V_2 = 1.25\ E_{\mathrm{R},2}$ (MI-BG transition) and for $V_2 = 1.5\ E_{\mathrm{R},2}$.

For a further increase of V_2 the resonance structure gets broader and weaker and the initial strong resonance structure of the Mott insulator phase is completely lost, which is in perfect agreement with the findings in the experiment [36].

3.6. Random-phase approximation (RPA)

3.6.1. Phonon operators and RPA equations

In this section, we try to refine the results of the Tamm-Dancoff approximation by improving on the phonon-operator expansion. The random-phase approximation is based on a phonon operator which also includes particle-hole de-excitations. The phonon operator (3.10) of the RPA reads

$$\mathbf{Q}^\dagger_{\mathrm{RPA},\nu} = \sum_{\{ij\}} X^{(\nu)}_{ij} \mathbf{c}^\dagger_{ij} - \sum_{\{ij\}} Y^{(\nu)}_{ij} \mathbf{c}_{ij}, \tag{3.65}$$

with the particle-hole excitation (de-excitation) operators $\mathbf{c}^\dagger_{ij}$ ($\mathbf{c}_{ij}$) and the expansion coefficients $X^{(\nu)}_{ij}$ and $Y^{(\nu)}_{ij}$. The sums in (3.65) run over pairs of site indices $\{i,j\}$ with $i \neq j$. The equation of motion (3.6) reads

$$\big\langle \mathrm{ref} \big| [\delta\mathbf{Q}, \mathbf{H}, \mathbf{Q}^\dagger_{\mathrm{RPA},\nu}] \big| \mathrm{ref} \big\rangle = E_{\nu 0} \big\langle \mathrm{ref} \big| [\delta\mathbf{Q}, \mathbf{Q}^\dagger_{\mathrm{RPA},\nu}] \big| \mathrm{ref} \big\rangle, \tag{3.66}$$

with the variations

$$\delta\mathbf{Q} = \quad \textstyle\sum_{\{ij\}} \delta X_{ij} \mathbf{c}^\dagger_{ij} \text{ and} \tag{3.67}$$

$$\delta\mathbf{Q} = \quad -\textstyle\sum_{\{ij\}} \delta Y_{ij} \mathbf{c}_{ij}. \tag{3.68}$$

In order to evaluate the RPA equation we substitute the phonon operator (3.65) into (3.66) and obtain a set of coupled equations for both variations (3.67) and (3.68). Plugging the variation (3.67) into (3.66) results in

$$\begin{aligned} &\sum_{\{i'j'\}\{ij\}} \big\langle \mathrm{ref} \big| [\mathbf{c}_{i'j'}, \mathbf{H}, \mathbf{c}^\dagger_{ij}] \big| \mathrm{ref} \big\rangle X^{(\nu)}_{ij} \delta X_{i'j'} - \sum_{\{i'j'\}\{ij\}} \big\langle \mathrm{ref} \big| [\mathbf{c}_{i'j'}, \mathbf{H}, \mathbf{c}_{ij}] \big| \mathrm{ref} \big\rangle Y^{(\nu)}_{ij} \delta X_{i'j'} = \\ &E_{\nu 0} \Bigg(\sum_{\{i'j'\}\{ij\}} \big\langle \mathrm{ref} \big| [\mathbf{c}_{i'j'}, \mathbf{c}^\dagger_{ij}] \big| \mathrm{ref} \big\rangle X^{(\nu)}_{ij} \delta X_{i'j'} - \sum_{\{i'j'\}\{ij\}} \big\langle \mathrm{ref} \big| [\mathbf{c}_{i'j'}, \mathbf{c}_{ij}] \big| \mathrm{ref} \big\rangle Y^{(\nu)}_{ij} \delta X_{i'j'} \Bigg). \end{aligned} \tag{3.69}$$

We can rearrange this equation by bringing both terms to the left hand side,

$$\begin{aligned} \sum_{\{i'j'\}} \Bigg\{ &\sum_{\{ij\}} \big\langle \mathrm{ref} \big| [\mathbf{c}_{i'j'}, \mathbf{H}, \mathbf{c}^\dagger_{ij}] \big| \mathrm{ref} \big\rangle X^{(\nu)}_{ij} - \sum_{\{ij\}} \big\langle \mathrm{ref} \big| [\mathbf{c}_{i'j'}, \mathbf{H}, \mathbf{c}_{ij}] \big| \mathrm{ref} \big\rangle Y^{(\nu)}_{ij} - \\ &E_{\nu 0} \Bigg(\sum_{\{ij\}} \big\langle \mathrm{ref} \big| [\mathbf{c}_{i'j'}, \mathbf{c}^\dagger_{ij}] \big| \mathrm{ref} \big\rangle X^{(\nu)}_{ij} - \sum_{\{ij\}} \big\langle \mathrm{ref} \big| [\mathbf{c}_{i'j'}, \mathbf{c}_{ij}] \big| \mathrm{ref} \big\rangle Y^{(\nu)}_{ij} \Bigg) \Bigg\} \delta X_{i'j'} = 0. \end{aligned} \tag{3.70}$$

Since equation (3.70) has to be true for any $\delta X_{i'j'}$, each summand of the outer sum in (3.70) has to be identical zero,

$$\begin{aligned} &\sum_{\{ij\}} \big\langle \mathrm{ref} \big| [\mathbf{c}_{i'j'}, \mathbf{H}, \mathbf{c}^\dagger_{ij}] \big| \mathrm{ref} \big\rangle X^{(\nu)}_{ij} - \sum_{\{ij\}} \big\langle \mathrm{ref} \big| [\mathbf{c}_{i'j'}, \mathbf{H}, \mathbf{c}_{ij}] \big| \mathrm{ref} \big\rangle Y^{(\nu)}_{ij} = \\ &\qquad E_{\nu 0} \Bigg(\sum_{\{ij\}} \big\langle \mathrm{ref} \big| [\mathbf{c}_{i'j'}, \mathbf{c}^\dagger_{ij}] \big| \mathrm{ref} \big\rangle X^{(\nu)}_{ij} - \sum_{\{ij\}} \big\langle \mathrm{ref} \big| [\mathbf{c}_{i'j'}, \mathbf{c}_{ij}] \big| \mathrm{ref} \big\rangle Y^{(\nu)}_{ij} \Bigg). \end{aligned} \tag{3.71}$$

We can treat the second variation (3.68) analogously and obtain

$$
\begin{aligned}
&-\sum_{\{ij\}} \big\langle \mathrm{ref} \big| \, [\mathbf{c}\dagger_{i'j'}, \mathbf{H}, \mathbf{c}^{]}_{ij} \big| \mathrm{ref} \big\rangle X^{(\nu)}_{ij} + \sum_{\{ij\}} \big\langle \mathrm{ref} \big| \, [\mathbf{c}\dagger_{i'j'}, \mathbf{H}, \mathbf{c}_{ij}] \big| \mathrm{ref} \big\rangle Y^{(\nu)}_{ij} = \\
&\qquad E_{\nu 0} \Bigg(-\sum_{\{ij\}} \big\langle \mathrm{ref} \big| \, [\mathbf{c}\dagger_{i'j'}, \mathbf{c}_{ij}] \big| \mathrm{ref} \big\rangle X^{(\nu)}_{ij} + \sum_{\{ij\}} \big\langle \mathrm{ref} \big| \, [\mathbf{c}\dagger_{i'j'}, \mathbf{c}_{ij}] \big| \mathrm{ref} \big\rangle Y^{(\nu)}_{ij} \Bigg). \qquad (3.72)
\end{aligned}
$$

The coupled equations (3.71) and (3.72) are represented by a general eigenproblem,

$$
\begin{pmatrix} \underline{A} & \underline{B} \\ -\underline{B} & -\underline{A} \end{pmatrix} \begin{pmatrix} X^{(\nu)} \\ Y^{(\nu)} \end{pmatrix} = \Delta E_\nu \begin{pmatrix} \underline{S} & -\underline{T} \\ -\underline{T} & \underline{S} \end{pmatrix} \begin{pmatrix} X^{(\nu)} \\ Y^{(\nu)} \end{pmatrix}. \qquad (3.73)
$$

with the matrix elements

$$
\begin{aligned}
A_{i'j'ij} &= \langle 0 | [\mathbf{c}_{i'j'}, \mathbf{H}, \mathbf{c}^\dagger_{ij}] | 0 \rangle &&= A_{iji'j'}, &&(3.74)\\
B_{i'j'ij} &= -\langle 0 | [\mathbf{c}_{i'j'}, \mathbf{H}, \mathbf{c}_{ij}] | 0 \rangle &&= B_{iji'j'}, &&(3.75)\\
S_{i'j'ij} &= \langle 0 | [\mathbf{c}_{i'j'}, \mathbf{c}^\dagger_{ij}] | 0 \rangle &&= S_{iji'j'}, &&(3.76)\\
T_{i'j'ij} &= \langle 0 | [\mathbf{c}_{i'j'}, \mathbf{c}_{ij}] | 0 \rangle &&= -T_{iji'j'}. &&(3.77)
\end{aligned}
$$

Note, that the we already used that the matrix elements are real. Since the particle-hole operators, four-operator type as well as projector-type (cf. Sect. 3.3.2), obey the bosonic commutator relations, the matrix $\underline{S}$ is the identity and $\underline{T}$ is zero and thus the metric matrix on the right-hand side of (3.73) is the identity. Consequently, (3.73) simplyfies to

$$
\begin{pmatrix} \underline{A} & \underline{B} \\ -\underline{B} & -\underline{A} \end{pmatrix} \begin{pmatrix} X^{(\nu)} \\ Y^{(\nu)} \end{pmatrix} = \Delta E_\nu \begin{pmatrix} X^{(\nu)} \\ Y^{(\nu)} \end{pmatrix}. \qquad (3.78)
$$

Analogously to the TDA eigenproblem in Sect. 3.5.1 its solution provides the excitation energies $E_{\nu 0}$ as well as the amplitudes $X^{(\nu)}_{ij}$ and $Y^{(\nu)}_{ij}$ which define the phonon operators $\mathbf{Q}^\dagger_{\nu,\mathrm{RPA}}$ and the excited state $\big| E_\nu \big\rangle$, respectively.

3.6.2. Analysis of the matrix elements

Submatrix $\underline{\mathsf{A}}$

In the following we analyze the matrix elements of the RPA equation (3.78). As reference state we consider the number state with one particle per site. The matrix $\underline{A}$ is identical to the TDA matrix, hence, our findings in Sect. 3.5.1 apply here as well, and we will just briefly recall them for both approaches of particle-hole operators.

Projector-type particle-hole operator. For the projector-type particle-hole operators we found that the matrix $\underline{A}$ is identical to the Hamiltonian represented in the space of 1p1h-excited states,

$$
A_{i'j'ij} = \big\langle \mathrm{ref} \big| \, [\mathbf{c}_{i'j'}, \mathbf{H}, \mathbf{c}^\dagger_{ij}] \big| \mathrm{ref} \big\rangle. \qquad (3.79)
$$

Four-operator particle-hole operator. For the four-operator particle-hole operators we found that they do not behave exactly as pure creation (annihilation) operators of particle-hole excitations. We referred to this as the *double-occupancy-transfer* problem (cf. Sect. 3.3.2). This behavior results in the transition between different particle-hole excited number states which affects a few matrix elements of $\underline{A}$. As a consequence of the deviations in the TDA matrix we observe modifications in the structure of the excited states which manifested in a more narrow response structure when evaluating strength functions.

Submatrix $\underline{B}$

For the matrix elements of $\underline{B}$ we unfold the double commutator in (3.75) first,

$$\begin{aligned} B_{i'j'ij} = \frac{1}{2}\Big(& 2\langle \mathrm{ref}|\,\mathbf{c}_{i'j'}\mathbf{H}\mathbf{c}_{ij}|\mathrm{ref}\rangle + 2\langle \mathrm{ref}|\,\mathbf{c}_{ij}\mathbf{H}\mathbf{c}_{i'j'}|\mathrm{ref}\rangle \\ & -\langle \mathrm{ref}|\,\mathbf{H}\mathbf{c}_{i'j'}\mathbf{c}_{ij}|\mathrm{ref}\rangle - \langle \mathrm{ref}|\,\mathbf{H}\mathbf{c}_{ij'}\mathbf{c}_{i'j'}|\mathrm{ref}\rangle \\ & -\langle \mathrm{ref}|\,\mathbf{c}_{i'j'}\mathbf{c}_{ij}\mathbf{H}|\mathrm{ref}\rangle - \langle \mathrm{ref}|\,\mathbf{c}_{ij}\mathbf{c}_{i'j'}\mathbf{H}|\mathrm{ref}\rangle\Big). \end{aligned} \tag{3.80}$$

In the first four terms of (3.80), a particle-hole de-excitation operator is applied to the reference state on the right-hand side, hence, those terms are trivially zero for both approaches of particle-hole operators.

Since the remaining two terms in (3.80) are of identical structure we discuss the last term only. The interaction part as well as the on-site energy part of the Hamiltonian cannot change a number state, hence, the particle-hole annihilation operator on the right-hand side in $\langle \mathrm{ref}|\,\mathbf{c}_{ij}\mathbf{c}_{i'j'}\mathbf{H}|\mathrm{ref}\rangle$ acts on the reference state and thus vanishes.

The tunneling part of the Hamiltonian, however, produces a linear combination of all next-neighbor particle-hole excitations on the right-hand side and $\mathbf{c}_{ij}$ applied to the left-hand side results in the bra state $\langle ij|$,

$$\langle \mathrm{ref}|\,\mathbf{c}_{ij}\mathbf{c}_{i'j'}\mathbf{H}|\mathrm{ref}\rangle = \sum_{\{|\mathrm{nn}ph\rangle\}} \langle ij|\,\mathbf{c}_{i'j'}|\mathrm{nn}ph\rangle. \tag{3.81}$$

Since both particle-hole operator behave differently starting from here, we discuss them separately in the following.

Projector-type particle-hole operator. The remaining particle-hole de-excitation operator in (3.81) can only de-excite the next-neighbor excited state $|\mathrm{nn}ph\rangle$ which is equal to $|i'j'\rangle$, all other kets will be mapped to zero. However, in case, the state $|\mathrm{nn}ph\rangle$ has been de-excited into the reference state $|\mathrm{ref}\rangle$, the expression vanishes due to the orthogonality of the number states,

$$\left\langle ij \middle| \mathrm{ref} \right\rangle = 0. \tag{3.82}$$

Consequently, the matrix element as well as the whole matrix $\underline{B}$ is zero. A vanishing matrix $\underline{B}$ results in a decoupling of the RPA equation (3.78), which is then identical to the solution of the corresponding TDA equation.

Four-operator particle-hole operator. Due to the *double-occupancy-transfer* behavior of the four-operator particle-hole operator, the particle-hole annihilator can transfer the next-neighbor excited ket on the right-hand of (3.81) into the bra state on the left-hand side for certain combinations i, j, i', j'. Hence, particular matrix elements $B_{i'j'ij}$ remain finite.

In summary, we can formulate the RPA equation with the four-operator approach of the particle-hole operators only, since the matrix $\underline{B}$ vanishes for the projector-type operators. Nevertheless, the non-vanishing matrix elements in $\underline{B}$ result purely from the *double-occupancy-transfer* behavior of the four-operator particle-hole operator and might therefore be artificial.

3.6.3. Contribution of particle-hole de-excitations to the solutions

The general advantage of RPA are the back-correlations described by the particle-hole annihilation operators in the phonon operator (3.65). A simple measure for the importance of these correlations is given by the $Y_{ij}^{(\nu)}$ amplitudes one obtains from the RPA eigenproblem (3.78). Figure 3.20 depicts the mean square norm of the amplitudes $X^{(\nu)}$ and $Y^{(\nu)}$ as function of U/J for a system with $I = N = 20$.

From $U/J = 0$ to 5 $\langle |X^{(\nu)}|^2 \rangle$ shows a linearly decline from $\langle |Y^{(\nu)}|^2 \rangle = 0.5$ to 0.03 with a kink to a shallow shape of the function starting from $U/J \approx 5$. In the region from $U/J = 5$ to 16 the $\langle |Y^{(\nu)}|^2 \rangle$ goes asymptotic from 0.03 to ~ 0. Hence, in this region, we can expect differences from the TDA results. For stronger interactions, $\langle |Y^{(\nu)}|^2 \rangle$ vanishes which means, that the RPA phonon-operators are fully described by particle-hole excitations but not de-excitations.

3.6.4. Strength functions

We briefly review the Gaussian strength function in view of the RPA phonon operator in this section. The Gaussian strength function

$$R_{\mathrm{GSF}}(\omega) = \sum_{\nu} E_{\nu 0} G_{\sigma}(\omega - E_{\nu 0}) |\left\langle \mathrm{ref} \right| [\mathbf{Q}_{\nu}, \mathbf{H}_J] \left| \mathrm{ref} \right\rangle|^2 \tag{3.83}$$

has been introduced in Sect. 3.5.4 with the transition matrix-element $\left\langle \mathrm{ref} \right| [\mathbf{Q}_{\nu}, \mathbf{H}_J] \left| \mathrm{ref} \right\rangle$. We assume the phonon operator of RPA (3.65) and unfold the commutator of the matrix

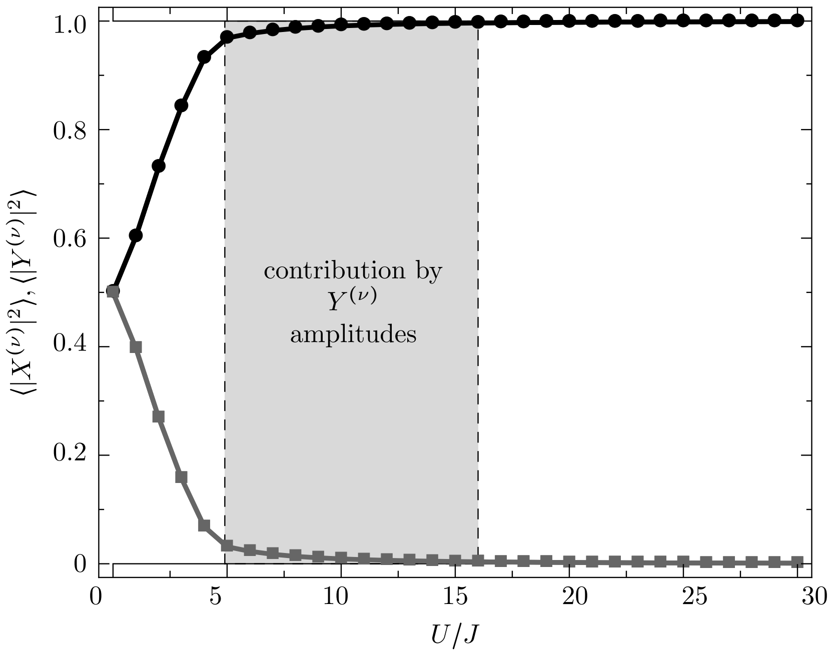

Fig. 3.20.: Average squared norm of the $X^{(\nu)}$ (—●—) and $Y^{(\nu)}$ (—■—) amplitudes plotted versus the interaction strength of a system of 20 bosons on 20 sites of a homogeneous lattice. The reference state for the RPA calculations is the number state with one particle per site.

element,

$$\begin{aligned}
\big\langle \mathrm{ref} \big| [\mathbf{Q}_\nu, \mathbf{H}_J] \big| \mathrm{ref} \big\rangle &= \big\langle \mathrm{ref} \big| \mathbf{Q}_\nu \mathbf{H}_J \big| \mathrm{ref} \big\rangle - \big\langle \mathrm{ref} \big| \mathbf{H}_J \mathbf{Q}_\nu \big| \mathrm{ref} \big\rangle && (3.84) \\
&= \sum_{ij} X_{ij}^{(\nu)*} \big\langle \mathrm{ref} \big| \mathbf{c}_{ij} \mathbf{H}_J \big| \mathrm{ref} \big\rangle - \sum_{ij} Y_{ij}^{(\nu)*} \big\langle \mathrm{ref} \big| \cancelto{0}{\mathbf{c}_{ij}^\dagger} \mathbf{H}_J \big| \mathrm{ref} \big\rangle && (3.85) \\
&\quad - \sum_{ij} X_{ij}^{(\nu)*} \big\langle \mathrm{ref} \big| \mathbf{H}_J \cancelto{0}{\mathbf{c}_{ij}} \big| \mathrm{ref} \big\rangle + \sum_{ij} Y_{ij}^{(\nu)*} \big\langle \mathrm{ref} \big| \mathbf{H}_J \mathbf{c}_{ij}^\dagger \big| \mathrm{ref} \big\rangle . && (3.86)
\end{aligned}$$

By dropping terms including the $Y_{ij}^{(\nu)}$ amplitudes we obtain the TDA matrix elements, which proofs that it is formally equivalent to $\big\langle \mathrm{ref} \big| \mathbf{Q}_\nu \mathbf{H}_J \big| \mathrm{ref} \big\rangle$ in this case. For the RPA, however, the commutator provides a second term which accounts for the back correlations in the ground state via the $Y_{ij}^{(\nu)}$. Hence, the introduction of the commutator in the transition matrix-element (3.84) is mandatory in order to take advantage of RPA full solution.

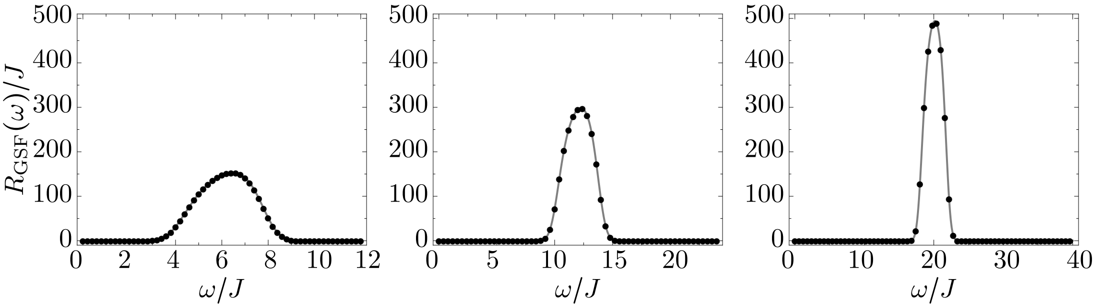

Fig. 3.21.: The U-resonance represented by the Gaussian strength function ($\sigma/J = 0.5$) for $I = N = 20$ and $U/J = 6$ (a), 12 (b), and 20 (c). Shown are the results of the RPA (solid line) and the 4TDA (dots).

3.6.5. Comparison of RPA and 4TDA

In order to investigate the impact of the $Y^{(\nu)}$ amplitudes on the solutions we compare the RPA with the corresponding 4TDA results. For both methods we employ the four-operator type particle-hole operators (cf. Sect. 3.3.2). Figure 3.21 illustrates the U-resonance for a system with $I = N = 20$ represented by Gaussian strength function (3.83). The strength function is based on the solutions of RPA and 4TDA for $U/J = 6$ (a), 12 (b), and 20 (c). The line represents the RPA results and the dots refer to the corresponding 4TDA solution. The plots show, that independent of the ratio U/J there is no visible difference between the RPA and 4TDA results. On one hand, this shows that the RPA suffers in the same way as the 4TDA from the *double-occupancy-transfer* behavior of the particle-hole operators. On the other hand, we observe that the $Y^{(\nu)}$ amplitudes do not have an effect on the solutions, though on would that expect in the vicinity of $U/J = 6$ from Fig. 3.20.

Since we know that the strength functions are based on eigenstates $|E_\nu\rangle$ with non-vanishing $|\langle\mathrm{ref}|\,[\mathbf{Q}_\nu, \mathbf{H}_J]|\mathrm{ref}\rangle|^2$, the $Y^{(\nu)}$ amplitudes seem not to play a role in their description. In order to check this, Fig. 3.22 shows the mean square of the $Y^{(\nu)}$ only for the states $|E_\nu\rangle$ with $|\langle\mathrm{ref}|\,[\mathbf{Q}_\nu, \mathbf{H}_J]|\mathrm{ref}\rangle|^2 \neq 0$. For $U/J = 0$ to 3 one observes a drop of the $Y^{(\nu)}$ from 0.5 to ~ 0.01 and for $U/J \gg 6$ its is 0. Hence, the contribution of the back-correlations is negligible in the strongly interacting regime.

RPA and pTDA

We discard the *problematic* terms in the $\underline{A}$-matrix of the RPA by replacing it with the corresponding pTDA matrix. Recall, that the pTDA is based on the projector-type particle-hole operators (cf. Sect. 3.3.2), which cured the *double-occupancy transfer* problem of the 4TDA. Moreover, the pTDA-matrix is the Hubbard Hamiltonian represented

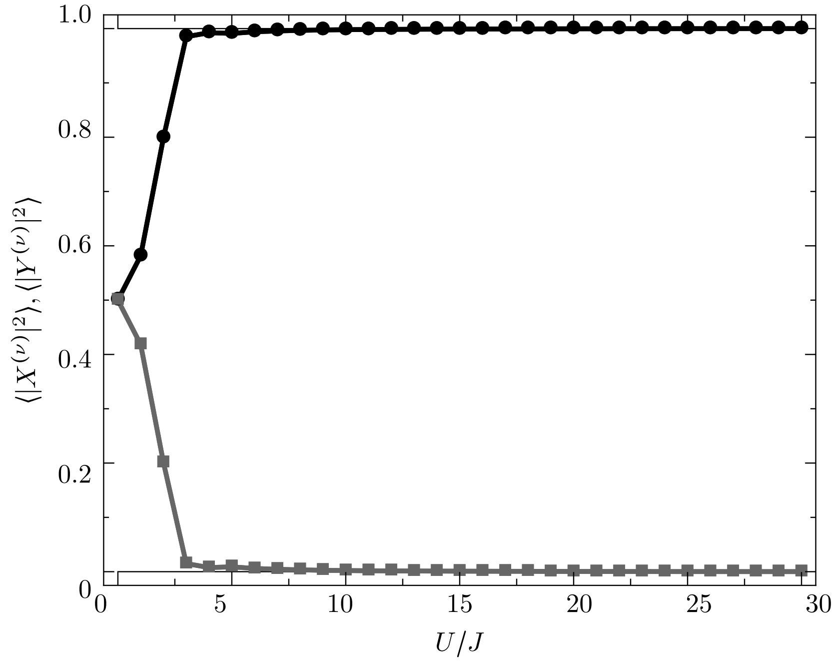

Fig. 3.22.: Average squared norm of the $X^{(\nu)}$ (—●—) and $Y^{(\nu)}$ (—■—) amplitudes with $|\langle\text{ref}|\,[\mathbf{Q}_\nu, \mathbf{H}_J]|\text{ref}\rangle|^2 \neq 0$ plotted versus the interaction strength of a system of 20 bosons on 20 sites of a homogeneous lattice. The reference state for the RPA calculations is the number state with one particle per site.

in the 1p1h-space with respect to the reference state (cf. Sect. 3.5.2).

Figures 3.23 compare the GSF obtained via the solution of the RPA with exchanged $\underline{A}$ matrix and the pTDA for ratios $U/J = 6$, 12, and 20. The results of RPA and pTDA are in perfect agreement, which demonstrates that the contributions of the $\underline{B}$ matrix, i.e. the back correlations, are irrelevant for the U resonance. Furthermore, the dropping of the *problematic* terms results in resonance widths that are in agreement with the pTDA results. In summary, only the four-operator type particle-hole operators allow to formulate the RPA equations. However, the non-vanishing matrix $\underline{B}$, which distinguishes the RPA equation from the corresponding TDA equations, is purely based on the fact, that the particle-hole operators are capable to move the double-occupation of a number state to a different site – which is neither a excitation nor a de-excitation. Moreover, the double-occupancy transfer behavior affects the matrix $\underline{A}$ in the same way it happens for the 4TDA and leads a more narrow U-resonance in comparison to pTDA and exact time-evolution. By exchanging the $\underline{A}$ matrix obtained with four-operator particle-hole operators with the pTDA matrix, we constructed a RPA matrix which reproduces the strength functions of pTDA in all aspects. This suggests, that the important element of a particle-hole method is to consider interacting particle-hole pairs like $\langle ij|\mathbf{H}|i'j'\rangle$ (pTDA). This shows at the same time that the back correlations are not relevant for the description of the U resonance.

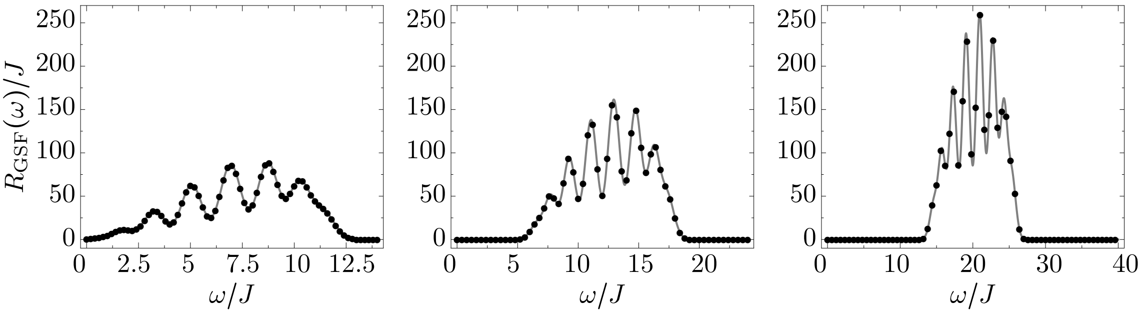

Fig. 3.23.: The U-resonance represented by the Gaussian strength function ($\sigma/J = 0.5$) for $I = N = 20$ and $U/J = 6$ (a), 12 (b), and 20 (c). Shown are the results of the RPA build of the $\underline{A}$ matrix using the projector-type ph-operators (solid line) and the pTDA (dots).

Appendix A

Linearization of the Bose-Hubbard Hamiltonian

We consider the Bose-Hubbard Hamiltonian given by

$$\mathbf{H} = -J[\tilde{V}_0]\mathbf{H}_J + U[\tilde{V}_0]\mathbf{H}_U \tag{A.1}$$

with operator structure hidden in

$$\mathbf{H}_J = \sum_{i=1}^{I} \left(\mathbf{a}_i^\dagger \mathbf{a}_{i+1} \mathbf{a}_{i+1}^\dagger \mathbf{a}_i \right) \quad \text{and} \quad \mathbf{H}_U = \frac{1}{2} \sum_{i=1}^{I} \mathbf{a}_i^\dagger \mathbf{a}_i^\dagger \mathbf{a}_i \mathbf{a}_i . \tag{A.2}$$

The Hubbard parameters J and U are functions of the time-dependent depth of the optical lattice (2.3),

$$\tilde{V}_0(t) = V_0[1 + F \sin(\omega t)], \tag{A.3}$$

which describes a temporal amplitude modulation with the relative amplitude F. The Hubbard parameters J and U are functions of the lattice depth V_0 and thus sensitive to its temporal variation. In a short notation the Hubbard Hamiltonian describing a homogeneous lattice system reads

$$\mathbf{H}(t) = -J[\tilde{V}_0(t)]\mathbf{H}_J + U[\tilde{V}_0(t)]\mathbf{H}_U \tag{A.4}$$

with the operator structure hidden in the symbols $\mathbf{H}_J$ and $\mathbf{H}_U$. Since we assume small modulations of the time-dependent lattice depth $V_0(t)$ around V_0 we can expand the Hamiltonian (2.13) and obtain a linearization by retaining the lowest-order terms only,

$$\mathbf{H}_{\text{lin}}(t) = \mathbf{H}_0 + \Delta V_0(t) \left. \frac{\partial \mathbf{H}}{\partial \tilde{V}_0} \right|_{V_0} + \mathcal{O}(\Delta V_0^2), \tag{A.5}$$

in which the the derivative can be decomposed by applying the chain rule

$$\frac{\partial \mathbf{H}}{\partial F}(t) = \left. \frac{d\mathbf{H}}{d\tilde{V}_0} \frac{d\tilde{V}_0}{dF}(t) \right|_{F=0} . \tag{A.6}$$

The derivative of the Hamiltonian with respect to the lattice amplitude $\tilde{V}_0$ is

$$\frac{d\mathbf{H}}{d\tilde{V}_0} = -\frac{d\mathbf{H}}{dJ} \frac{dJ}{d\tilde{V}_0} + \frac{d\mathbf{H}}{dU} \frac{dU}{d\tilde{V}_0}, \tag{A.7}$$

in which $d\mathbf{H}/dJ = \mathbf{H}_J$ and $d\mathbf{H}/dU = \mathbf{H}_U$. It is convenient to express $\mathbf{H}_U$ in terms of $\mathbf{H}$ and $\mathbf{H}_J$ using (A.1),

$$\frac{d\mathbf{H}}{d\tilde{V}_0} = \frac{1}{U}\frac{dU}{d\tilde{V}_0}\mathbf{H} - J\left(\frac{1}{J}\frac{dJ}{d\tilde{V}_0} - \frac{1}{U}\frac{dU}{d\tilde{V}_0}\right)\mathbf{H}_J \tag{A.8}$$

$$= \frac{d\ln U}{d\tilde{V}_0}\mathbf{H} - J\left(\frac{d\ln J}{d\tilde{V}_0} - \frac{d\ln U}{d\tilde{V}_0}\right)\mathbf{H}_J. \tag{A.9}$$

The derivative of the lattice amplitude $\tilde{V}_0$ with respect to the modulation amplitude F in (A.6) can be directly evaluated to

$$\frac{d\tilde{V}_0}{dF} = V_0\sin(\omega t). \tag{A.10}$$

By substitution of (A.9) and (A.10) into (2.14) we arrive at the full expression for the linearized Bose-Hubbard Hamiltonian

$$\mathbf{H}_{\mathrm{lin}}(t) = \mathbf{H}_0 + FV_0\sin(\omega t)\left[\left.\frac{d\ln U}{d\tilde{V}_0}\right|_{V_0}\mathbf{H} - J\left(\left.\frac{d\ln J}{d\tilde{V}_0}\right|_{V_0} - \left.\frac{d\ln U}{d\tilde{V}_0}\right|_{V_0}\right)\mathbf{H}_J\right]. \tag{A.11}$$

Appendix B

Derivation of the transition amplitudes

Since we assume a small amplitude modulation the transition probabilities $P_{0\to n}$ from the ground state into an excited state can be derived by applying the time-dependent perturbation theory. The following derivation can be found in various quantum mechanics textbooks, i.e. [64].

Due to the small amplitude modulation we consider the excitation to stay close to the unperturbed state. We consider the eigenproblem of the unperturbed Hamiltonian $\mathbf{H}_0 = \mathbf{H}(t = 0)$ to be solved,

$$\mathbf{H}_0 \left|n\right\rangle = E_n \left|n\right\rangle, \tag{B.1}$$

i.e. the orthonormal and complete eigenbasis $\{\left|n\right\rangle\}$ as well as the energy eigenvalues E_n are known. For clarity, we shorten the linearized Hamiltonian (A.11) to

$$\mathbf{H}_{\text{lin}}(t) = \mathbf{H}_0 + \lambda \mathbf{V}(t), \tag{B.2}$$

by defining the time-dependent perturbation

$$\mathbf{V}(t) = F V_0 \sin(\omega t) \left[\left.\frac{d\ln U}{d\tilde{V}_0}\right|_{V_0} \mathbf{H} - J \left(\left.\frac{d\ln J}{d\tilde{V}_0}\right|_{V_0} - \left.\frac{d\ln U}{d\tilde{V}_0}\right|_{V_0} \right) \mathbf{H}_J \right]. \tag{B.3}$$

The parameter λ has been introduced for book-keeping reasons and is set to $\lambda = 1$ at the end. The Schrödinger equation for the time-dependent Hamiltonian reads

$$\mathbf{i}\frac{\partial}{\partial t} \left|\psi, t\right\rangle = \left[\mathbf{H}_0 + \lambda \mathbf{V}(t)\right] \left|\psi, t\right\rangle, \tag{B.4}$$

with the general solution expressed in the basis of the unperturbed Hamiltonian $\mathbf{H}_0$

$$\left|\psi, t\right\rangle = \sum_k c_k(t) \exp(-\mathbf{i} E_k t) \left|n\right\rangle, \tag{B.5}$$

in which the sum runs over the full eigenbasis. The expansion coefficients are chosen time dependent due to the time-dependent perturbation; for vanishing perturbation ($\lambda = 0$) the coefficients would be constant $c_n = \left\langle n \middle| \psi, 0\right\rangle$. The expansion (B.5) can be substituted into (B.4)

$$\sum_k \left(\mathbf{i} \frac{dc_k(t)}{dt} + E_k c_k(t) \right) \exp(-\mathbf{i}E_k t) \left|k\right\rangle = \sum_k c_k(t) \exp(-\mathbf{i}E_k t) \left(E_k + \lambda \mathbf{V}(t)\right) \left|k\right\rangle, \quad \text{(B.6)}$$

which we project into the static Hamiltonians eigenbasis $\{\left\langle m\right|\}$,

$$\mathbf{i} \frac{dc_k(t)}{dt} = \lambda \sum_k c_k(t) \exp(-\mathbf{i}\omega_{mk} t) \left\langle m\right| \mathbf{V}(t) \left|k\right\rangle, \quad \text{(B.7)}$$

with $\omega_{mk} = E_m - E_k$. This equation describes the time-evolution of the coefficients of $\left|psi, t\right\rangle$ in the basis of the static Hamiltonian. Therefore, it is equivalent to (B.4). The perturbation series for the coefficients reads

$$c_m(t) = c_m^{(0)}(t) + \lambda c_m^{(1)}(t) + \lambda^2 c_m^{(2)}(t) + \cdots \quad \text{(B.8)}$$

with the initial conditions $c_m^{(0)}(0) = \delta_{mn}$ and $c_m^{(1)}(0) = c_m^{(2)}(0) = \cdots = 0$. These initial conditions define the initial state $\left|\psi, 0\right\rangle = \left|n\right\rangle$, which can be proved by plugging (B.8) into (B.5). In principal, we are just interested in the transition amplitudes from the ground state into excited states, so for our purposes we consider $n = 0$.

We plug (B.8) into (B.7) and write down the terms up to first order in λ,

$$\mathbf{i} \frac{dc_m^{(0)}(t)}{dt} + \mathbf{i}\lambda \frac{dc_m^{(1)}(t)}{dt} + \mathcal{O}(\lambda^2) = \lambda \sum_k c_k^{(0)}(t) \exp(-\mathbf{i}\omega_{mk} t) \left\langle m\right| \mathbf{V}(t) \left|k\right\rangle + \mathcal{O}(\lambda^2). \quad \text{(B.9)}$$

The zeroth order in λ is

$$\mathbf{i} \frac{dc_m^{(0)}(t)}{dt} = 0 \quad \text{(B.10)}$$

which solves to $c_m^{(0)} = \delta_{mn}$ using the initial conditions given above. We can substitute this into the right hand side of (B.9) and write down the first order in λ,

$$\mathbf{i} \frac{dc_m^{(1)}(t)}{dt} = \exp(\mathbf{i}\omega_{mn} t) \left\langle m\right| \mathbf{V}(t) \left|n\right\rangle, \quad \text{(B.11)}$$

with the formal solution

$$c_m^{(1)}(\tau) = -\mathbf{i} \int_0^\tau dt' \exp(\mathbf{i}\omega_{mn} t') \left\langle m\right| \mathbf{V}(t') \left|n\right\rangle. \quad \text{(B.12)}$$

$c_m^{(1)}(t)$ is the first order coefficient of the initial Hamiltonians eigenstate $\left|m\right\rangle$ to the state $\left|\psi, t\right\rangle$. In other words, $|c_m^{(1)}(t)|^2$ is the transition probability $P_{n \to m}$ between the initial state $|n\rangle$ and $|m\rangle$. In our case, with the initial state $|n=0\rangle$, the full expression is

$$P^{(\tau)}_{0\to m} = |c^{(1)}_m(\tau)|^2 = \left|\int_0^\tau dt' \exp(\mathbf{i}\omega_{m0}t')\langle m|\,\mathbf{V}(t')|0\rangle\right|^2, \tag{B.13}$$

with the duration of the perturbation τ. Equation (B.13) is a general expression for the transition probability for any time-dependent perturbation $\mathbf{V}(t)$ which is sufficiently small to be treated perturbative.

By plugging the (B.3) into (B.13) one obtains the full expression for the transition probabilities in view of the linearized Bose-Hubbard Hamiltonian (A.11),

$$P^{(\tau)}_{0\to m} = \left|JV_0Ff(\omega,\omega_{i0},\tau)\left(\frac{d\ln J}{d\tilde{V}_0}\bigg|_{V_0} - \frac{d\ln U}{d\tilde{V}_0}\bigg|_{V_0}\right)\langle E_i|\,\mathbf{H}_J|0\rangle\right|^2. \tag{B.14}$$

We have neglected the term proportional to $\mathbf{H}$ in the above expression, since this operator does not connect between excited states. The function

$$f(\omega,\omega_{i0},\tau) = \int_0^\tau dt' \sin(\omega t')e^{\mathbf{i}\omega_{i0}t'} \tag{B.15}$$

with $\hbar\omega_{i0} = E_i - E_0$ is the time-integral of the transition probability over the perturbation time τ. For the further investigation, we rewrite the periodic perturbation to $\sin(\omega t) = (\exp(\mathbf{i}\omega t) - \exp(-\mathbf{i}\omega t))/2\mathbf{i}$ and get the integral

$$|f(\omega,\omega_{i0},\tau)|^2 = \frac{1}{4}\left|\int_0^\tau dt' e^{\mathbf{i}(\omega_{i0}+\omega)t'} - e^{\mathbf{i}(\omega_{i0}-\omega)t'}\right|^2 \tag{B.16}$$

which evaluates to

$$|f(\omega,\omega_{i0},\tau)|^2 = \frac{1}{4}\left|\frac{e^{\mathbf{i}(\omega_{i0}+\omega)\tau}-1}{\omega_{i0}+\omega} - \frac{e^{\mathbf{i}(\omega_{i0}-\omega)\tau}-1}{\omega_{i0}-\omega}\right|^2. \tag{B.17}$$

For $\omega \approx \omega_{i0}$ the first term can be neglected in the above expression, since $f(\omega,\omega_{i0},\tau)$ is dominated by the second,

$$|f(\omega,\omega_{i0},\tau)|^2 \approx \frac{1}{4}\left|\frac{e^{\mathbf{i}(\omega_{i0}-\omega)\tau}-1}{\omega_{i0}-\omega}\right|^2, \tag{B.18}$$

and by using $|\exp(\mathbf{i}\phi)-1|^2 = |\exp(\mathbf{i}\phi/2) - \exp(-\mathbf{i}\phi/2)|^2 = 4\sin^2(\phi/2)$ we obtain

$$|f(\omega,\omega_{i0},\tau)|^2 \approx \frac{\sin^2[(\omega_{i0}-\omega)\tau/2]}{(\omega_{i0}-\omega)^2}. \tag{B.19}$$

The function (B.19) is illustrated in Fig. B.1. The roots close to ω_{i0} of (B.19) with respect to the modulation frequency ω define the width of the peak, which is given by $\Delta\omega = 4\pi/\tau$.

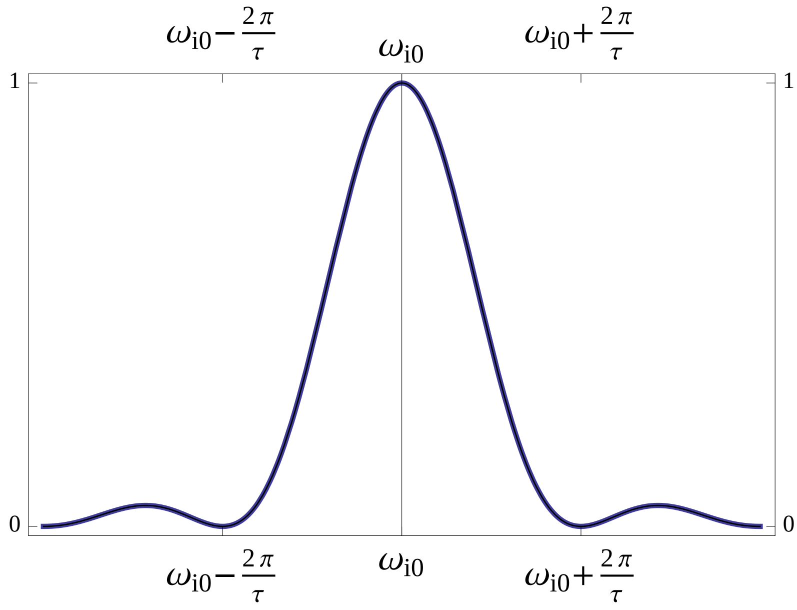

Fig. B.1.: Plot of the function $\frac{\sin^2[(\omega_{i0}-\omega)\tau/2]}{(\omega_{i0}-\omega)^2}$.

This reflects the energy-time uncertainty, because a modulation for larger times τ results in a sharper energetic width.

Finally, the final expression for the transition probabilities is given by

$$P^{(\tau)}_{0\to i}(\omega) = \left| J V_0 F \left(\left.\frac{d\ln J}{d\tilde{V}_0}\right|_{V_0} - \left.\frac{d\ln U}{d\tilde{V}_0}\right|_{V_0} \right) \left\langle E_i \middle| \mathbf{H}_J \middle| \mathrm{ref} \right\rangle \right|^2 \frac{\sin^2[(\omega_{i0}-\omega)\tau/2]}{(\omega_{i0}-\omega)^2}. \tag{B.20}$$

Appendix C

Crank-Nicholson scheme

The Crank-Nicholson (CN) scheme combines the explicit an implicit Euler method in order to solve an ordinary differential equation (ODE). For the derivation, we assume the initial state $\left|\psi, 0\right\rangle = \left|\psi, t = 0\right\rangle$ and the time-dependent Schrödinger equation

$$\left|\psi, t\right\rangle = -\frac{\mathbf{i}}{\hbar}\mathbf{H}(t)\left|\psi, t\right\rangle \tag{C.1}$$

with the Hamilton operator $\mathbf{H}(t)$. We discretize time in sufficiently[1] small time steps Δt. At the nth time step the Hamiltonian is $\mathbf{H}_n = \mathbf{H}(t_n)$.

The explicit Euler step is

$$\left|\psi, t_{n+1}\right\rangle = \left|\psi, t_n\right\rangle + \Delta t\frac{\partial}{\partial t}\left|\psi, t_n\right\rangle \tag{C.2}$$

$$= \left|\psi, t_n\right\rangle - \Delta t\frac{\mathbf{i}}{\hbar}\mathbf{H}_n\left|\psi, t_n\right\rangle, \tag{C.3}$$

where we used the time-dependent Schrödinger equation (C.1) in the last step. The implicit Euler step is given analogously by

$$\left|\psi, t_{n+1}\right\rangle = \left|\psi, t_n\right\rangle + \Delta t\frac{\partial}{\partial t}\left|\psi, t_{n+1}\right\rangle \tag{C.4}$$

$$= \left|\psi, t_n\right\rangle - \Delta t\frac{\mathbf{i}}{\hbar}\mathbf{H}_{n+1}\left|\psi, t_{n+1}\right\rangle. \tag{C.5}$$

The CN step can be written as half of an explicit and half of an implicit Euler step,

$$\left|\psi, t_{n+1}\right\rangle = \left|\psi, t_n\right\rangle - \frac{\Delta t}{2}\frac{\mathbf{i}}{\hbar}\mathbf{H}_n\left|\psi, t_n\right\rangle - \frac{\Delta t}{2}\frac{\mathbf{i}}{\hbar}\mathbf{H}_{n+1}\left|\psi, t_{n+1}\right\rangle, \tag{C.6}$$

which can be rewritten to

$$\left(1 + \frac{\Delta t}{2}\frac{\mathbf{i}}{\hbar}\mathbf{H}_{n+1}\right)\left|\psi, t_{n+1}\right\rangle = \left(1 - \frac{\Delta t}{2}\frac{\mathbf{i}}{\hbar}\mathbf{H}_n\right)\left|\psi, t_n\right\rangle. \tag{C.7}$$

The CN step can be written in the compact form

$$\left|\psi, t_{n+1}\right\rangle = \frac{1 - \frac{\Delta t}{2}\frac{\mathbf{i}}{\hbar}\mathbf{H}_{n+1/2}}{1 + \frac{\Delta t}{2}\frac{\mathbf{i}}{\hbar}\mathbf{H}_{n+1/2}}\left|\psi, t_n\right\rangle. \tag{C.8}$$

---

[1] The time steps are chosen sufficiently small in order to assume $\mathbf{H}(t)$ constant in the interval t, $t + \Delta t$.

The subscript of the Hamiltonian $\mathbf{H}_{n+1/2}$ denotes, that the operator is evaluated in the center of the time interval at $t_n + \Delta t/2$, which ensures unitarity of the CN step.

By representing the operators and states in a basis (e.g. the number basis), equation (C.7) defines a set of linear equations, which has to be solved in order to evolve the state $|\psi, t_n\rangle$ to $|\psi, t_n\rangle$.

Appendix D

Projector vs. four-operator approach: differences in the matrix elements & impact on the solution

Although the two approaches of particle-hole operators produce matching excitation energies in the TDA calculations, the structure of the excited states show severe differences. The differences can be observed indirectly in the strength functions (cf. Fig. 3.4): the pTDA (projector ph-operator) resembles the response function of the reference calculation (S2PH), whereas 4TDA (four-operator ph-operator) shows a significantly narrower response. A first guess would be to suspect similarly squeezed bandwidth of the first Hubbard band in case of the 4TDA, but from the discussion of the excitation energies in Sect. 3.5.3 we know that the energies match well.

Hence, the structure of the excited states must be the key, since they are the crucial ingredient to the transition matrix elements, which "select" the states that are excited. In Sect. 3.5.1 we have already pointed out, that the four-operator type particle-hole operators does effect some matrix elements due to the fact, that they also transfer double occupancies between the sites.

Combinatorial analysis: which configurations produce altered matrix elements

The transportation of the double occupancy occurs in the following term of the unfolded double commutator (3.32) of the matrix element,

$$\big\langle \mathrm{ref}\big|\, \mathbf{c}_{ij}\mathbf{c}^{\dagger}_{i'j'}\mathbf{H}\big|\mathrm{ref}\big\rangle. \tag{D.1}$$

Since in this term the Hamiltonian acts directly on the reference state on the right, only the hopping part can contribute. The reference state has only singly occupied sites, so the interaction part of the Hamiltonian vanishes. The initial situation is, that the annihilator generates a particle-hole excited state $\big\langle ij\big|$ to the left, and the hopping operator produces a sum of all next-neighbor excited states $\big|\mathrm{nn}ph\big\rangle$ to the right,

$$-\sqrt{2}\,J\big\langle ij\big|\,\mathbf{c}^{\dagger}_{i'j'}\big|\mathrm{nn}ph\big\rangle. \tag{D.2}$$

Since the particle-hole creator is capable to move the double occupation, it is possible to generate a non-vanishing overlap. Let us in the following construct situations, in which

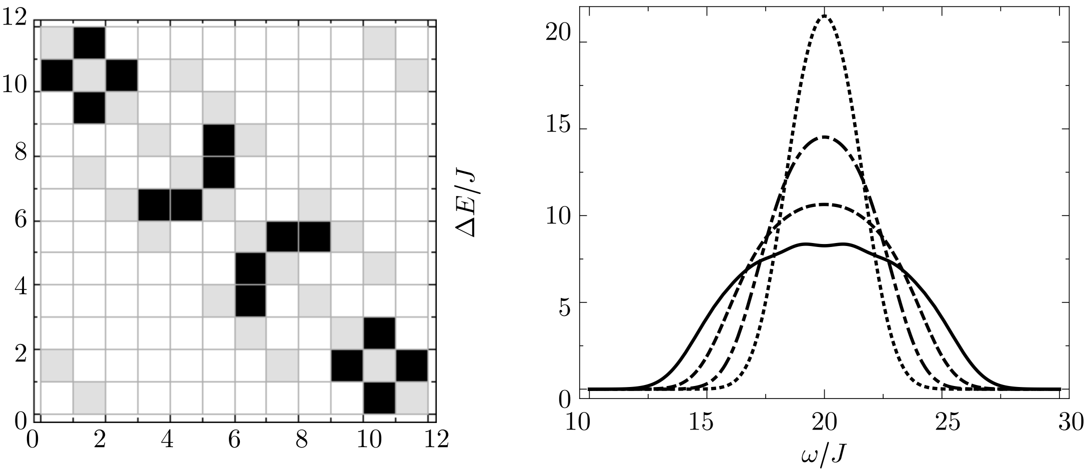

Fig. D.1.: The panel on the left hand side shows the structure of the TDA matrix of a system of 4 bosons on 4 sites. White boxes refer to zero matrix elements, gray ones are non-zero elements, and black ones are those non-zero matrix elements which are different in both particle-hole operator approaches. The small system is chosen for clarity, but the general structure is transferable to larger systems.. The panel on the right hand side shows the transition of the 1U-resonance for a system of 20 bosons on 20 sites at $U/J = 20$ calculated with different stages of the sweep between the TDA matrices of both *ph*-operator approaches. Shown is the pure projector-type approach (———)and the pure four-operator type approach (-------). The two other curves result from interpolations between the two TDA matrices, 33% (— — —) and 66% (-—-—-) from the projector approach.

such a non-vanishing overlap occurs. The bra state on the left of (D.2) could be any particle-hole excited number state, for which there are $I(I-1)$ possibilities. Since we have to create a next-neighbor excited state, we can split these states in two classes, number states with a next-neighbor excitation

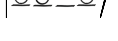
next-neighbor excited state (D.3)

and those with excitations over one or more sites,

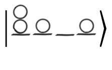
isolated hole state (D.4)

which we call *isolated hole states* in the following. For each next-neighbor excited state exists exactly one particle-hole creator, which can move the double occupation over the hole and create another next-neighbor state,

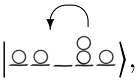

Since the hopping operator creates a sum of all next-neighbor states, we get a non-vanishing overlap. The number of next-neighbor states is $2I$, which is since each of the I sites can exist with a hole on the left and on the right (we consider periodic boundary conditions). This makes in sum $2I$ pairs of configurations, which create additional contributions to a matrix elements due to the transfer behavior of the particle-hole creator.

For the *isolated hole states*, there are two possible particle-hole creators to produce a next-neighbor state,

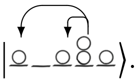

The number of *isolated hole states* is $I(I-3)$, since there are I possibilities to put the hole, which then blocks this particular site and its 2 neighbors for the double occupation. This makes $2\,I(I-3)$ possible particle-hole creators, which lead to non-vanishing matrix elements.

Both cases, next-neighbor and isolated hole states, sum up to a total of $2\,I(I-2)$ varied matrix elements. On the left panel of Fig. D.1, the matrix elements which vary between the both approaches are pointed out for a system of 4 bosons on 4 sites. The considerations we made above predict 16 varied matrix elements, which matches exactly with the findings in the figure. The according particle-hole operators to this example are given in appendix E.

It should be emphasized, that this transfer behavior does not produce additional non-vanishing matrix elements. All configurations which lead to a finite contribution by (D.1), do also produce contributions by the term $\langle \mathrm{ref} | \mathbf{c}_{ij} \mathbf{H} \mathbf{c}^{\dagger}_{i'j'} | \mathrm{ref} \rangle$.

The interesting question that arises is, how these *contaminated* matrix elements effect the diagonalization, i.e. the process of solving the TDA equations. Convincingly, such manipulations of the matrix have an effect on the structure of the eigenstates. But the manipulations here are so subtle, that the eigenvalues remain unchanged.

It can be easily proven, that the contribution by (D.1) inasmuch as the particle-hole operators that are involved fulfill the requirements from above, is always $2J$. Whereas, the contribution from the term $\langle \mathrm{ref} | \mathbf{c}_{ij} \mathbf{H} \mathbf{c}^{\dagger}_{i'j'} | \mathrm{ref} \rangle$ is always $-J$ in those cases. Consequently, the very matrix elements are $-J$ in the projector-type TDA whereas they are $-J + 2J = +J$ in the 4-operator type TDA. This means, that the difference in the matrices is just a sign change of some of the off-diagonal elements.

The panel on the right hand side of Fig. D.1 shows the strength curve of both TDA approaches and two intermediate stages of the transition from one TDA matrix into the other. For the representation of the curves we used the strength function (3.51) with a large width $\sigma/J = 1$ for clarity.

Appendix E

Particle-hole operators for 4 bosons on 4 sites

$$
\begin{aligned}
\mathbf{c}_1^\dagger &= \mathbf{a}_1^\dagger\mathbf{a}_1^\dagger\mathbf{a}_1\mathbf{a}_2 & \qquad \mathbf{c}_1 &= \mathbf{a}_2^\dagger\mathbf{a}_1^\dagger\mathbf{a}_1\mathbf{a}_1\\
\mathbf{c}_2^\dagger &= \mathbf{a}_1^\dagger\mathbf{a}_1^\dagger\mathbf{a}_1\mathbf{a}_3 & \mathbf{c}_2 &= \mathbf{a}_3^\dagger\mathbf{a}_1^\dagger\mathbf{a}_1\mathbf{a}_1\\
\mathbf{c}_3^\dagger &= \mathbf{a}_1^\dagger\mathbf{a}_1^\dagger\mathbf{a}_1\mathbf{a}_4 & \mathbf{c}_3 &= \mathbf{a}_4^\dagger\mathbf{a}_1^\dagger\mathbf{a}_1\mathbf{a}_1\\
\mathbf{c}_4^\dagger &= \mathbf{a}_2^\dagger\mathbf{a}_2^\dagger\mathbf{a}_2\mathbf{a}_1 & \mathbf{c}_4 &= \mathbf{a}_1^\dagger\mathbf{a}_2^\dagger\mathbf{a}_2\mathbf{a}_2\\
\mathbf{c}_5^\dagger &= \mathbf{a}_2^\dagger\mathbf{a}_2^\dagger\mathbf{a}_2\mathbf{a}_3 & \mathbf{c}_5 &= \mathbf{a}_3^\dagger\mathbf{a}_2^\dagger\mathbf{a}_2\mathbf{a}_2\\
\mathbf{c}_6^\dagger &= \mathbf{a}_2^\dagger\mathbf{a}_2^\dagger\mathbf{a}_2\mathbf{a}_4 & \mathbf{c}_6 &= \mathbf{a}_4^\dagger\mathbf{a}_2^\dagger\mathbf{a}_2\mathbf{a}_2\\
\mathbf{c}_7^\dagger &= \mathbf{a}_3^\dagger\mathbf{a}_3^\dagger\mathbf{a}_3\mathbf{a}_1 & \mathbf{c}_7 &= \mathbf{a}_1^\dagger\mathbf{a}_3^\dagger\mathbf{a}_3\mathbf{a}_3\\
\mathbf{c}_8^\dagger &= \mathbf{a}_3^\dagger\mathbf{a}_3^\dagger\mathbf{a}_3\mathbf{a}_2 & \mathbf{c}_8 &= \mathbf{a}_2^\dagger\mathbf{a}_3^\dagger\mathbf{a}_3\mathbf{a}_3\\
\mathbf{c}_9^\dagger &= \mathbf{a}_3^\dagger\mathbf{a}_3^\dagger\mathbf{a}_3\mathbf{a}_4 & \mathbf{c}_9 &= \mathbf{a}_4^\dagger\mathbf{a}_3^\dagger\mathbf{a}_3\mathbf{a}_3\\
\mathbf{c}_{10}^\dagger &= \mathbf{a}_4^\dagger\mathbf{a}_4^\dagger\mathbf{a}_4\mathbf{a}_1 & \mathbf{c}_{10} &= \mathbf{a}_1^\dagger\mathbf{a}_4^\dagger\mathbf{a}_4\mathbf{a}_4\\
\mathbf{c}_{11}^\dagger &= \mathbf{a}_4^\dagger\mathbf{a}_4^\dagger\mathbf{a}_4\mathbf{a}_2 & \mathbf{c}_{11} &= \mathbf{a}_2^\dagger\mathbf{a}_4^\dagger\mathbf{a}_4\mathbf{a}_4\\
\mathbf{c}_{12}^\dagger &= \mathbf{a}_4^\dagger\mathbf{a}_4^\dagger\mathbf{a}_4\mathbf{a}_3 & \mathbf{c}_{12} &= \mathbf{a}_3^\dagger\mathbf{a}_4^\dagger\mathbf{a}_4\mathbf{a}_4
\end{aligned}
$$

Conventions

Constants & Variables

$\hbar = c = 1$	natural units
$a_0 = 52.9177 \times 10^{-12}\,\mathrm{m}$	Bohr radius
N	number of particles
I	number of lattice sites
J	tunneling strength
U	interaction strength
ϵ_i	on-site potential at site i

States

$\left\|1,0,1,2\right\rangle$ = 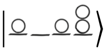	number state with per-site occupation as quantum numbers
$\left\|1,0,1,2\right\rangle$ or 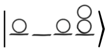	1-particle-1-hole (1p1h) states
$\left\|0,2,0,2\right\rangle$, $\left\|0,3,0,1\right\rangle$ or 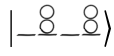 , 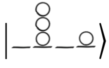	2-particle-2-hole (2p2h) states
$\left\|\mathrm{nn}ph\right\rangle$	a **n**ext-**n**eighbor **p**article-**h**ole excitation, i.e. $\left\|1,0,2,1\right\rangle$

Operators

$\mathbf{a}_i^\dagger$	particle creation operator at site i
$\mathbf{a}_i$	particle creation operator at site i
$\mathbf{c}_k^\dagger$	particle-hole creation operator
$\mathbf{c}_k$	particle-hole annihilation operator
$\mathbf{\Pi}_\alpha = \left\|\alpha\right\rangle\left\langle\alpha\right\|$	projection operator on state $\left\|\alpha\right\rangle$

Acronyms

BEC	Bose-Einstein condensate
BHM	Bose-Hubbard model
TOF	Time of flight
SEQ	stationary Schroedinger equation
SPH	stationary Schroedinger equation in 0p0h+1p1h-space
S2PH	stationary Schroedinger equation in 0p0h+1p1h+2p2h-space
S3PH	stationary Schroedinger equation in 0p0h+1p1h+2p2h+3p3h-space
tSEQ	time-dependent Schroedinger equation
TDA	Tamm-Dancoff approximation
4TDA	TDA based on four-operator type particle-hole operators
pTDA	TDA based on projector type particle-hole operators
RPA	Random-phase approximation
GSF	Gaussian based strength function
PSF	perturbative strength function

Bibliography

[1] S. Bose, Zeitschrift für Physik A Hadrons and Nuclei, 178(1924)

[2] A. Einstein, Sitzungsberichte der Preussischen Akademie der Wissenschaften. Phys.-Mathe. Klasse, 261(1924)

[3] H. Kamerlingh-Onnes, Comm. Phys. Lab. Univ. Leiden **122 and 124** (1911)

[4] V. Ginzburg and L. Landau, Zh. Eksp. Teor. Fiz. **20** (1950)

[5] J. Bardeen, L. N. Cooper, and J. R. Schrieffer, Phys. Rev. **108**, 1175 (1957)

[6] P. Kapitza, Nature **141**, 74 (1938)

[7] J. F. Allen and A. D. Misner, Nature **141**, 75 (1938)

[8] D. G. Henshaw and A. D. B. Woods, Phys. Rev. **121**, 1266 (1961)

[9] R. W. Cline, D. A. Smith, T. J. Greytak, and D. Kleppner, Phys. Rev. Lett. **45**, 2117 (1980)

[10] D. E. Pritchard, Phys. Rev. Lett. **51**, 1336 (1983)

[11] M. H. Anderson, J. R. Ensher, M. R. Matthews, C. E. Wieman, and E. A. Cornell, Science **269**, 198 (1995)

[12] `http://patapsco.nist.gov/imagegallery/details.cfm?imageid=193`

[13] K. B. Davis, M. O. Mewes, M. R. Andrews, N. J. van Druten, D. S. Durfee, D. M. Kurn, and W. Ketterle, Phys. Rev. Lett. **75** (1995)

[14] M. R. Andrews, C. G. Townsend, H.-J. Miesner, D. S. Durfee, D. M. Kurn, and W. Ketterle, Science **275**, 637 (1997)

[15] M.-O. Mewes, M. R. Andrews, D. M. Kurn, D. S. Durfee, C. G. Townsend, and W. Ketterle, Phys. Rev. Lett. **78**, 582 (1997)

[16] D. Jaksch, C. Bruder, J. I. Cirac, C. W. Gardiner, and P. Zoller, Phys. Rev. Lett. **81**, 3108 (1998)

[17] M. P. A. Fisher, P. B. Weichman, G. Grinstein, and D. S. Fisher, Phys. Rev. B **40** (1989)

[18] J. K. Freericks and H. Monien, Europhys. Lett. **26**, 545 (1994)

[19] T. D. Kühner and H. Monien, Phys. Rev. B **58**, R14741 (1998)

[20] J. Hubbard, Proceedings of the Royal Society of London. Series A. Mathematical and Physical Sciences **276**, 238 (1963)

[21] M. Greiner, O. Mandel, T. Esslinger, T. W. Hänsch, and I. Bloch, Nature **415**, 39 (2002)

[22] `http://www.quantum-munich.de/media/mott-insulator/`

[23] K. Braun-Munzinger, J. A. Dunningham, and K. Burnett, Phys. Rev. A **69**, 053613 (2004)

[24] S. R. Clark and D. Jaksch, New J. Phys. **8**, 160 (2006)

[25] M. Hild, F. Schmitt, and R. Roth, J. Phys. B: At. Mol. Opt. Phys. **39**, 4547 (2006)

[26] M. Hild, F. Schmitt, I. Türschmann, and R. Roth, Phys. Rev. A **76**, 053614 (2007)

[27] A. Iucci, M. A. Cazalilla, A. F. Ho, and T. Giamarchi, Phys. Rev. A **73** (04 2006)

[28] C. Kollath, A. Iucci, T. Giamarchi, W. Hofstetter, and U. Schollwöck, Phys. Rev. Lett. **97** (2006)

[29] R. Roth and K. Burnett, Phys. Rev. A **67** (2003)

[30] R. Roth and K. Burnett, J. Opt. B: Quantum Semiclass. Opt. **5**, S50 (2003)

[31] R. Roth and K. Burnett, Phys. Rev. A **68**, 023604 (2003)

[32] G. Roux, T. Barthel, I. P. McCulloch, C. Kollath, U. Schollwock, and T. Giamarchi, Phys. Rev. A **78**, 023628 (2008)

[33] F. Schmitt, M. Hild, and R. Roth, Phys. Rev. A **80**, 023621 (2009)

[34] F. Schmitt, M. Hild, and R. Roth, J. Phys. B: At. Mol. Opt. Phys. **40**, 371 (2007)

[35] L. Fallani, L. De Sarlo, J. E. Lye, M. Modugno, R. Saers, C. Fort, and M. Inguscio, Phys. Rev. Lett. **93** (2004)

[36] L. Fallani, J. E. Lye, V. Guarrera, C. Fort, and M. Inguscio, Phys. Rev. Lett. **98**, 130404 (2007)

[37] M. Greiner, O. Mandel, T. W. Hansch, and I. Bloch, Nature **419**, 51 (2002)

[38] V. Guarrera, L. Fallani, J. E. Lye, C. Fort, and M. Inguscio, New Journal of Physics **9**, 107 (2007)

[39] T. Stöferle, H. Moritz, C. Schori, M. Köhl, and T. Esslinger, Phys. Rev. Lett. **92**, 130403 (2004)

[40] K. Sengupta and N. Dupuis, Europhys. Lett. **70**, 586 (2005)

[41] J. Stenger, S. Inouye, A. P. Chikkatur, D. M. Stamper-Kurn, D. E. Pritchard, and W. Ketterle, Phys. Rev. Lett. **82**, 4569 (1999)

[42] I. Bloch, Nature Physics **1**, 23 (2005)

[43] R. Grimm, M. Weidemüller, and Y. B. Ovchinnikov, arXiv:physics/9902072v1 [physics.atom-ph]

[44] W. Jones and N. H. March, *Theoretical Solid State Physics (Volume 1)* (Wiley, 1973)

[45] F. Bloch, Zeitschrift für Physik A Hadrons and Nuclei **52** (1929)

[46] N. F. Mott, Proceedings of the Physical Society. Section A **62**, 416 (1949)

[47] G. G. Batrouni and R. T. Scalettar, Phys. Rev. B **46**, 9051 (1992)

[48] J. K. Freericks and H. Monien, Phys. Rev. B **53**, 2691 (1996)

[49] S. R. White, Phys. Rev. Lett. **69**, 2863 (1992)

[50] U. Schollwöck, Rev. Mod. Phys. **77**, 259 (2005)

[51] G. H. Wannier, Phys. Rev. **52**, 191 (1937)

[52] P. W. Anderson, Phys. Rev. **109**, 1492 (1958)

[53] K. Braun-Munzinger, *Dynamics of Bose-Einstein Condensates in optical Lattices*, Ph.D. thesis, University of Oxford (2004)

[54] W. H. Press, *Numerical recipes: the art of scientific computing*, 3rd ed. (Cambridge University Press, 2007)

[55] J. C. Butcher, *Numerical Methods Ordinary Differential Equations* (Wiley, 2003)

[56] E. A. Hylleraas and B. Undheim, Zeitschrift für Physik A Hadrons and Nuclei **65**, 759 (1930)

[57] J. K. L. MacDonald, Phys. Rev. **43**, 830 (1933)

[58] D. Bohm and D. Pines, Phys. Rev. **92**, 609 (1953)

[59] D. J. Rowe, Phys. Rev. **175**, 1283 (1968)

[60] D. J. Rowe, Rev. Mod. Phys. **40**, 153 (1968)

[61] P. Ring and P. Schuck, *The Nuclear Many-Body Problem* (Springer, 1980)

[62] D. J. Thouless, Nuclear Physics **21** (1960)

[63] M. Hild, "Quantum dynamics & excitations of ultracold atomic gases in optical lattices," Diploma Thesis (2005)

[64] T. Fließbach, *Quantenmechanik*, 3rd ed. (Spektrum Akademischer Verlag, 2000)

Danksagung

An erster Stelle danke ich Prof. Robert Roth für die Annahme als Doktorand und die erstklassige Betreuung während der vergangenen vier Jahre.

Prof. Jochen Wambach danke ich für die Bereitschaft zur Erstellung des Zweitgutachtens, trotz der knappen Zeit.

Ich danke Dr. Panagiota Papakonstantinou, die entscheidend zur Formulierung der Teilchen-Loch Methoden beigetragen hat, und darüberhinaus zum Korrekturlesen dieser Arbeit bereit stand.

Dank gebührt Felix Schmitt, meinem Mitstreiter erster Stunde, der durch anregende Diskussionen und Unterstützung maßgeblich zum Gelingen dieser Arbeit beigetragen hat. Des weiteren danke ich Verena Kleinhaus, Mathias Wagner und Heiko Hergert (mittlerweile *alle* Kaffeetrinker), die immer zu Diskussion (Physik, Apple, IT allgemein,... oder ganz allgemein), zum Kaffee trinken oder auch zum Korrekturlesen bereit sind.

Ich danke Clemens Kruspel und Tinka Spehr und vor allem meiner Mutter Lieselotte und meinem Bruder Michael für die Unterstützung während des gesamten Studiums.

Lebenslauf

Zur Person

Name	Markus Hild
Geburtstag	01. Januar 1976
Geburtsort	Bad Soden - Salmünster
Staatsangehörigkeit	deutsch
Eltern	Hans-Rudolf Hild (†) Lieselotte Hild, geb. Lissmann

Bildungsweg

07/1982 - 05/1986	Grundschule Brachttal
06/1986 - 06/1992	Gesamtschule Wächtersbach, Realschulzweig
09/1992 - 01/1995	Berufsausbildung zum Chemikant, Cassella AG, Frankfurt/M.
01/1995	vorgezogene Gesellenprüfung
01/1995 - 06/1995	Chemikant, Cassella AG, Frankfurt/M.
09/1995 - 06/1998	Berufliches Gymnasium, Ludwig-Geissler Schule, Hanau Fachrichtung Chemietechnik
06/1998	Abitur, Gesamtnote: *1.2*
07/1998 - 10/1999	Zivildienst, Sozialstation Brachttal
10/1999 - 10/2005	Studium der Physik an der TU Darmstadt
10/2005	Diplomarbeit *"Quantum Dynamics & Excitations of Ultracold Atomic Gases in Optical Lattices"* Diplom, Gesamtnote: *sehr gut*
10/2005 - 12/2009	Promotionsstudium an der TU Darmstadt und Anfertigung der Dissertation